AN ABSTRACT OF THE DISSERTATION OF

Jennifer A. Thomas for the degree of Doctor of Philosophy in Ocean, Earth, and Atmospheric Sciences presented on August 27, 2018.

Title: Horizontal Variability of Internal Waves and Tides:
Seafloor Pressure Measurements and Idealized Resonant Modes

Abstract approved: _____

James A. Lerczak

Internal waves and tides are a dominant source of current variability, and they are intermittent and hard to predict. Internal waves can have significant variability in alongshore structure. However, previous studies on internal waves have focused primarily on their cross-shore structure and propagation. For example, while alongshore-propagating superinertial internal tides are known to exist in the ocean, their dynamics are not well understood. This dissertation entails two research directions that address different aspects of along- (and cross-) shore properties of internal waves, focusing on understanding alongshore variability of internal waves and tides and mechanisms that cause it. In one (Chapter 2), observations from seafloor pressure sensors and linear theory are used to investigate along- and cross-shore structure of high-frequency nonlinear internal waves. In the other (Chapters 3 and 4), linear theory is used to investigate excitation of coupled barotropic-baroclinic resonant modes

in idealized basins and their application to understanding coastal and basin internal tide dynamics and intermittency.

In Chapter 2, along- and cross-shore variability in propagation speed, direction, and kinetic energy of packets of high-frequency nonlinear internal waves in Massachusetts Bay are investigated using a two-dimensional array of seafloor pressure sensors and linear theory. This region is known for the predictable occurrence of these wave packets, making it a good location to test the utility of using an array of low-cost pressure sensors to study high-frequency internal waves. Speed and direction are determined using only the pressure sensors, and their alongshore variability is quantified. Linear theory predicts a relationship between kinetic energy and bottom pressure variance that is sensitive to sheared background currents, water depth, and stratification. Comparisons with seafloor acoustic Doppler current profiler measurements nonetheless show a strong relationship between kinetic energy and bottom pressure variance. This is presumably due to phase locking of the wave packets to the internal tide that dominates background currents and to horizontally uniform and relatively constant stratification throughout the study. Thus the observed bottom pressure variance is used to qualitatively describe variations in wave packet kinetic energy.

In Chapter 3, linear theory for idealized two-layered basins with a free surface and alongshore uniform shelves is used to investigate effects of basin size, continental shelves, shelf-deep phase speed ratio, and rotation on coupled barotropic-baroclinic superinertial resonant modes. Large amplitude coupled barotropic-baroclinic basin modes, shelf-amplified basin modes, and edge modes are excited by a body force,

modeled as an idealized equilibrium tide. Shelves are shown to have a strong effect on basin modes once the shelf width is greater than a quarter-wavelength of a mode. The phase speed ratio over the shelf versus deep basin is important in determining how much mode structures will be affected by shelves. The smaller the ratio, the more separation between scales of shelf and deep responses, resulting in more edge modes for a given frequency range and edge modes that decay faster into the deep basin. Full basin mode excitation requires a basin to reach equilibrium, but time scales over which stratification and thus basin mode structure change could be shorter than baroclinic adjustment times. Therefore, in the real ocean, basin modes for barotropic tides could occur in large basins, due to their relatively fast phase speeds, but slower propagating baroclinic tides would only be able to develop full basin modes in smaller basins. Shelf-trapped edge modes depend only on the shelf geometry, and not that of the deep basin, so baroclinic edge modes can develop much more quickly, making them possible for any continental shelf with the appropriately tuned geometry. In rotating basins, baroclinic edge modes can have phase that propagates alongshore (in either direction) or a complicated phase and amplitude structure that results in what appears more like standing waves. These findings indicate that shelves and shelf-deep phase speed ratios can have a significant impact on the structure of barotropic and baroclinic tides, that resonant mode excitation can generate large-amplitude shelf-trapped superinertial internal tides, and that some temporal variability of internal tides could be explained by stratification tuning toward and away from resonance.

Building on this, in Chapter 4, alongshore shelf width variability is introduced to the idealized basins. In nature, continental shelves are not perfectly uniform along-

shore, so these simulations are performed to understand what might happen with resonant modes in the real ocean. A small phase speed ratio over the shelf versus deep basin is used to focus on responses over the shelf. The shelf is on the western boundary of the basin, and is narrow to the north and south, with a wide middle section. Some resonant edge modes have large amplitudes isolated to the wide section of the shelf, some have large amplitudes along the entire shelf, but more confined to the narrow width extent, and some have large amplitudes distributed over the entire shelf. Alongshelf and cross-shelf wavelength scales in a resonant response can be different for the narrow versus wide sections of shelf, as can sense of phase propagation. These results indicate that large-amplitude superinertial internal tides from resonant edge modes can occur on realistic continental shelves of ocean basins, with resonance being associated with smaller segments of a shelf and not needing to communicate with the entire alongshelf distance of a basin. This could account for some observations of alongshelf variability in superinertial internal tides.

Horizontal Variability of Internal Waves and Tides: Seafloor Pressure Measurements and Idealized Resonant Modes

by

Jennifer A. Thomas

A DISSERTATION

submitted to

Oregon State University

in partial fulfillment of
the requirements for the
degree of

Doctor of Philosophy

Presented August 27, 2018
Commencement June 2019

Doctor of Philosophy dissertation of Jennifer A. Thomas presented on August 27, 2018.

APPROVED:

Major Professor, representing Ocean, Earth, and Atmospheric Sciences

---

Dean of the College of Earth, Ocean, and Atmospheric Sciences

---

Dean of the Graduate School

I understand that my dissertation will become part of the permanent collection of Oregon State University libraries. My signature below authorizes release of my dissertation to any reader upon request.

Jennifer A. Thomas, Author

ACKNOWLEDGEMENTS

I would first like to thank my advisor, Jim Lerczak. I feel very lucky to have worked with Jim. He provided me with great opportunities for research, learning, presenting my research, meeting people in our field, and participating in field work, always supporting my growth as a scientist and guiding me along the way. I appreciate all of Jim's effort in helping me succeed throughout graduate school and in preparing me for my future. Jim, I really admire you as a scientist and teacher. Though it was short lived, I am thankful we got to play music together. I will always remember "The Troths", as well as the crests! Thank you for working with me, Jim!

I am thankful to Jim Moum for being a supportive coauthor and bringing new elements into my research on internal waves in Massachusetts Bay, testing the limits of what we could achieve with seafloor pressure sensors. I am thankful to Clint Winant for sharing his research ideas on resonant modes with me, for helping guide me through all of the process, and for being a great mentor.

I am thankful to my committee members: Roger Samelson, Emily Shroyer, and Jonathan Nash. They have all been mentors to me, helping me navigate this process of graduate school scientifically and personally. I am especially thankful to Roger for figuring out why my model was not conserving volume and helping me move forward with it when I needed it most. If not for him, we might all be in over our heads!

I am really thankful to have had this opportunity to be a graduate student in CEOAS. There are so many wonderful professors in our department who have enriched my experience. I am thankful to Kipp Shearman, Larry O'Neill, and Eric Skyllingstad,

for encouraging me–and letting me–teach lectures in their courses. That challenge and opportunity helped me realize I enjoy teaching and let me gain experience in doing so. Eric, it has been fun being across the hall from you. Thank you for always answering my research and otherwise questions, and for putting up with that time I filled your office with balloon animals! Thank you to Bill Smyth for being an inspiring teacher, and for welcoming me into his music family. Bill, your support of my solo music means the world to me, and I am sorry I quit the band! Thank you to all of the faculty and staff of CEOAS for making sure all of the logistics of being in graduate school went smoothly for me, especially Robert Allan and Lori Hartline. And a special thank you to Bruce Marler for getting me and all of my files safely onto a new computer when my computer died a few months before defending!

Thank you to my lab group members, Emily Lemagie, Jack McSweeney, and Anna Pfeiffer-Herbert, for your support, advice, editing, and friendship throughout the years. You all were always there for me, and I learned so much from you.

Thank you to my friend, and sole cohort member, Juan Muglia. Juancho, it was so much better to go through all of this with you. From the beginnings of "J-Team" at math camp, to classes, comprehensive exams, research, and all of the adventures in between, we have been through a lot together. I am glad we survived the 180 off the pass, as well as graduate school. We did it!

Thank you to my dad, mom, and sister: William Thomas, Susan Thomas, and Leah Thomas Montegut. Your love and support gives me the ability and confidence to succeed in accomplishing my goals. I love you all so much!

To my boyfriend, Tom Laster (and his little dog, Mathilde, too!), you have been

my rock through all of this, my number one cheerleader. Thank you! I love you! And I can't wait to be able to Netflix and chill with you, again!

Thank you to all of my surfing, music, hiking, and science buddies throughout grad school, including Ale Sanchez-Rios, Ashley Ellenson, Jenessa Duncombe, Na Hyung Choi, Colleen Wall, Kim Jones, Christo Buizert, Erica Yerkey, Raychel Kolen, Paul Allen, Alex Simpson, Scott Gerweck, Sally Warner, and many others. You all make my life whole and will always be important to me. Thank you Corvallis Community Band (trumpet beers!), Salem Philharmonia Orchestra (dive-bar karaoke!), all the various pit orchestra ensembles, The Flow, The Hilltop Big Band, and The Hot Air Band. It was so rewarding playing music with all of you.

TABLE OF CONTENTS

TABLE OF CONTENTS (Continued)

TABLE OF CONTENTS (Continued)

LIST OF FIGURES

LIST OF FIGURES (Continued)

LIST OF FIGURES (Continued)

LIST OF TABLES

LIST OF APPENDIX FIGURES

Chapter 1: General introduction

1.1 Objectives

This thesis entails two research directions associated with studying internal waves. The first, in Chapter 2, uses observations of seafloor pressure and linear theory to investigate the along- and cross-shore structure of packets of high-frequency nonlinear internal waves in Massachusetts Bay. The main goal of this study was to test the utility of using low-cost pressure sensors in studying the horizontal properties of internal waves, as well as to learn about the along- and cross-shore structure of these waves. The second research direction, in Chapters 3 and 4, uses linear theory to investigate the excitation of coupled barotropic-baroclinic resonant basin and shelf modes by the equilibrium tide in idealized basins, to understand their application to coastal and basin internal tide dynamics. The main goal of this study was to determine if resonance could result in large-amplitude superinertial internal tides over the continental shelf, and also explain some observations of temporal intermittency and spatial variability in internal tides.

1.2 Background, motivation, and key results

Internal waves and tides are an important source of current variability on continental shelves (e.g. Lerczak et al. 2003; Alford et al. 2006; Savidge et al. 2007; Aguirre

et al. 2010; Aristizábal et al. 2016). Although internal waves can propagate alongshore and can have alongshore variability, most studies on internal waves have focused on their cross-shore properties, characterizing their evolution as they propagate onshore. The studies in this thesis are all related to understanding alongshore, as well as cross-shore, properties of internal waves.

In order to study horizontal variability of internal waves, observations are needed over a large horizontal extent. The methods and instruments commonly used for making internal wave observations (e.g. acoustic Doppler current profilers (ADCPs); conductivity, temperature, and depth sensors; thermistor strings; and shipboard profiling) can be expensive and complicated to deploy and retrieve, making it difficult and involved to collect data on internal waves over a large horizontal extent. Seafloor pressure sensors are relatively inexpensive and easy to deploy and retrieve.

In thesis Chapter 2, we take advantage of this, using data from a two-dimensional array of 14 seafloor pressure sensors over a 14-km by 12-km area to study the horizontal properties of the high-frequency nonlinear internal wave packets known to propagate through Massachusetts Bay with each semidiurnal internal tide, in order to test the limits of studying internal waves with seafloor pressure sensors. Band-pass filtering the pressure data enables the identification of high-frequency internal waves as well as their arrival times at each pressure sensor over the array. Thus, we were able to use the data to triangulate internal wave propagation speed and direction and to quantitatively show how these vary along- and across-shore, as well as to compare pressure variance with kinetic energy (from an ADCP) of the internal waves. Linear theory demonstrates that the pressure variance-kinetic energy relationship depends

on sheared background currents, water depth, and stratification, but because of the phase-locking of the internal waves with the internal tide that dominates background currents and because of the horizontally uniform stratification of the study site, there was a strong relationship between the seafloor pressure variance and kinetic energy.

It is understood that coastal-trapped superinertial internal tides can only be partially trapped to the coast, losing energy to the deep basin through internal wave propagation offshore in all directions (Chapman 1982; Dale and Sherwin 1996; Dale et al. 2001), but the transition from perfectly-trapped subinertial edge modes to imperfectly-trapped superinertial edge waves has been shown to be gradual as frequency increases (Dale et al. 2001). It has been suggested that continental shelf sections with appropriately tuned geometry to a superinertial tidal frequency might result in a resonant baroclinic response over that segment of shelf, leading to alongshelf dependence of the superinertial internal tide (Dale and Sherwin 1996). In thesis Chapters 3 and 4, we explore the resonant excitation of coupled barotropic-baroclinic basin and edge modes by the equilibrium tide to explore superinertial internal tides, with the particular goal to show resonant excitation of coastal-trapped superinertial internal tides over the continental shelf and how this can depend on variability of alongshelf geometry.

In thesis Chapter 3, we develop the linear model for idealized coupled basins, beginning with more simplified basins, from one-dimensional, flat bathymetry, with no rotation building up to two-dimensional, with alongshore uniform continental shelves and rotation on an f-plane, in order to begin with an analytical framework from which understanding of more complicated basins can be built. From this, we present the

effects of different model parameters, showing that shelf width and phase speed ratio between the shelf and deep basin are important in determining the effects of shelves on basin and edge modes, and the extent of trapping over the shelf. One interesting finding is that in any basin with continental shelves, all of the barotropic basin modes have baroclinic scales coupled to their response. This work also shows that large-amplitude superinertial coastal-trapped internal tides can develop over the shelf due to resonant edge mode excitation by the equilibrium tide, that these responses do not depend on the deep basin geometry, and that the phase and amplitude distribution of edge modes can result in various complicated structures.

In thesis Chapter 4, we build on the findings from Chapter 3, adding alongshore shelf width variability to the idealized two-dimensional, rotating basins. Here, we focus on baroclinic responses over the shelf, demonstrating how alongshore variability in shelf width affects resonant modes and that resonance can result in large-amplitude superinertial internal tides that are isolated to a particular shelf segment. The shelf phase and amplitude distribution again result in diverse complicated structures. With the added complexity of varying shelf widths, along- and across-shelf wavelength scales and propagation direction can be different for wide and narrow shelf regions, even within a single resonant mode, clearly demonstrating the asymmetry of edge modes in rotating basins, which results in preferred propagation directions for edge modes (Huthnance 1975). These results show that resonance can result in alongshelf dependence of superinertial internal tides on continental shelves.

Chapter 5 is a summary of the general conclusions of this thesis.

Chapter 2: Horizontal variability of high-frequency nonlinear internal waves in Massachusetts Bay detected by an array of seafloor pressure sensors

Jennifer Thomas, James Lerczak, and James Moum

Journal of Geophysical Research: Oceans

2000 Florida Avenue N.W.

Washington, DC 20009-1227

USA

Volume 121 Issue 8, doi:10.1002/2016JC011866, 2016.

2.1 Abstract

A two-dimensional array of 14 seafloor pressure sensors was deployed to measure properties of tidally-generated, nonlinear, high-frequency internal waves over a 14-km by 12-km area west of Stellwagen Bank in Massachusetts Bay during summer 2009. Thirteen high-frequency internal wave packets propagated through the region over 6.5 days (one packet every semidiurnal cycle). Propagation speed and direction of wave packets were determined by triangulation, using arrival times and distances between triads of sensor locations. Wavefront curvature ranged from straight to radially spreading, with wave speeds generally faster to the south. Waves propagated to the southwest, rotating to more westward with shoreward propagation. Linear theory predicts a relationship between kinetic energy and bottom pressure variance of internal waves that is sensitive to sheared background currents, water depth, and stratification. By comparison to seafloor acoustic Doppler current profiler measurements, observations nonetheless show a strong relationship between kinetic energy and bottom pressure variance. This is presumably due to phase-locking of the wave packets to the internal tide that dominates background currents and to horizontally uniform and relatively constant stratification throughout the study. This relationship was used to qualitatively describe variations in kinetic energy of the high-frequency wave packets. In general, high-frequency internal wave kinetic energy was greater near the southern extent of wavefronts and greatly decreased upon propagating shoreward of the 40-m isobath.

2.2 Introduction

A relatively new technique to study internal waves uses observations of seafloor pressure (Moum and Smyth 2006; Moum and Nash 2008; Stöber and Moum 2011). The seafloor pressure signal of a packet of nonlinear internal waves of elevation (depression) is a sequence of positive (negative) pressure perturbations (Moum and Smyth 2006; Moum and Nash 2008). This bottom pressure signal principally arises from the internal hydrostatic pressure perturbation (formed by the displacement of isopycnals by the passing internal wave), with lesser contributions from the external hydrostatic (surface displacement) and the non-hydrostatic pressure perturbations. Here, we extend the technique to a two-dimensional array of pressure sensors to make both cross-shore and alongshore in situ observations of high-frequency internal waves in a region west of Stellwagen Bank in Massachusetts Bay (Fig. 2.1). This seafloor antenna of 14 sensors yields both wave direction and speed as well as a detailed depiction of alongshore variability of high-frequency nonlinear internal waves. Our specific objectives are to:

1. quantify high-frequency internal wave speed and propagation direction;
2. quantify spatial variations in wave speed and direction;
3. determine the relationship between bottom pressure variance and high-frequency internal wave kinetic energy;
4. qualitatively describe spatial variations in high-frequency internal wave kinetic energy, based on bottom pressure variance.

Various methods have been used to calculate internal wave speed and propagation

direction from observations. One method uses wave arrival times at moorings at different horizontal locations. With a linear array of moorings, wave propagation direction must be assumed or determined from other information, such as satellite data (Alford et al. 2010). Other methods include shipboard tracking with acoustic backscatter and radar (Moum and Nash 2008; Shroyer et al. 2009) and using shore-based still photography (Bourgault and Kelley 2003). Scotti et al. (2005) calculated speed and direction for high-frequency (short wavelength) internal waves using backscatter intensity and lag in arrival time between the four acoustic beams of an acoustic Doppler current profiler (ADCP) due to horizontal separation of the beams.

Qualitative information on properties along internal wavefronts, such as spatial distribution and wavefront curvature, are revealed by Synthetic Aperture Radar (SAR) satellite imagery and photography (Hsu et al. 2000; Bourgault and Kelley 2003; Butman et al. 2006; da Silva and Helfrich 2008). Satellite data, however, is not always available for the time period and location of interest, and in both SAR imagery and photography, the presence of an internal wave is not always detectable. Thus, these types of remote sensing typically need to be combined with in situ measurements to make quantitative evaluations.

While most in situ internal wave studies have only addressed these propagation properties in the cross-shore direction (along the propagation path of the waves), here we use a bottom pressure array to address both cross-shore and alongshore spatial variability.

Variations in internal wave energy have been studied primarily in the cross-shore direction, via detailed measurements of velocity, temperature, and salinity from moor-

ings, bottom landers, and shipboard profiling (Scotti et al. 2006; Moum et al. 2007; Alford et al. 2010; Shroyer et al. 2010). In order to study spatial variations in internal wave energy based on bottom pressure measurements, a relationship between the bottom pressure and energy of the internal waves must be determined. For mode-one linear and, to leading order, weakly-nonlinear, weakly-dispersive internal wave theory, bottom pressure and all other wave fields are directly related via wave amplitude (e.g., pycnocline displacement) and their respective vertical structure functions. Therefore, in principle, it should be straightforward to relate, for example, internal wave kinetic energy to bottom pressure variance. Then, assuming internal wave energy is equipartitioned between kinetic and potential energy, (Osborne and Burch 1980; Moum et al. 2007; Shroyer et al. 2010) internal wave energy density, energy flux and flux divergence could be obtained from an array of bottom pressure sensors.

In practice, background stratification must be known in order to relate internal wave variables. If stratification does not vary horizontally–that is, if background isopycnals are flat–wave field vertical structure functions will vary as bottom depth changes, but this should be straightforward to calculate. In addition, sheared background currents will impact internal wave propagation (Maslowe and Redekopp 1980; Stastna and Lamb 2002; Choi 2006; Alford et al. 2010; Shroyer et al. 2011) and the relationship between internal wave variables.

Here we quantify the influences of changes in stratification, water depth, and sheared background currents on the kinetic energy/bottom pressure variance relationship and we assess the feasibility of using bottom pressure measurements to quantify spatial variations in high-frequency internal wave energy.

Our study site, Massachusetts Bay, is known for the predictable occurrence of tidally-generated nonlinear internal tides during periods of strong stratification (summer and early fall) (Halpern 1971; Haury et al. 1979; Chereskin 1983). These internal waves are generated from interaction of the barotropic tide with Stellwagen Bank (Fig. 2.1a) (Scotti and Pineda 2004; Butman et al. 2006; Scotti et al. 2007, 2008; Lai et al. 2010). The waves have been characterized through observational (e.g. Scotti and Pineda 2004; Butman et al. 2006) and two-dimensional (cross-shore) modeling (e.g. Scotti et al. 2007, 2008; Lai et al. 2010) studies. A large-scale (O(5 km)) pycnocline depression propagates shoreward from Stellwagen Bank each semidiurnal tidal cycle (Scotti et al. 2007). Upon entering Massachusetts Bay, the leading edge of the depression steepens and develops into an undular bore. Thus, the nonlinear internal tide is a large-scale depression of the pycnocline with a packet of high-frequency waves of depression at its leading edge (Scotti et al. 2007; Lai et al. 2010). Observations have shown that the nonlinear internal tide propagates shoreward through Massachusetts Bay at speeds ranging from about 0.2 to 0.7 m s^{-1}, containing a packet of about 5 to 10 high-frequency oscillations with periods of 5 to 10 minutes and roughly 100 to 400-m wavelengths (Scotti and Pineda 2004; Scotti et al. 2005; Butman et al. 2006). The oscillations depress the thermocline by as much as 30 m, and the entire packet of high-frequency oscillations takes 1 to 2 hours to propagate past a given location (Butman et al. 2006; Scotti et al. 2006). Details of the high-frequency packet structure and propagation speed depend on the stratification and the strength of the tide (Scotti et al. 2007; Lai et al. 2010). As the nonlinear internal tide approaches water depths between 30 to 50 m, it interacts strongly with the sea floor, transforming in structure,

with significant loss of high-frequency energy. Details of this transformation depend on wave amplitude and stratification (Scotti et al. 2008).

This paper is organized as follows. Section 2.3 is a description of the measurements and data analysis methods. Results are in section 2.4, describing the bottom pressure record (2.4.1.); wave direction and speed (2.4.2.); the relationship between kinetic energy and bottom pressure variance, and relative kinetic energy (2.4.3.). Section 2.5 is a discussion that expands on spatial variations in wave direction and speed (2.5.1.); bottom pressure variance versus kinetic energy (2.5.2.); spatial variations in high-frequency internal wave kinetic energy (2.5.3.); and wave packet-to-wave packet variability (2.5.4.). Conclusions are in section 2.6.

2.3 Methods

2.3.1 Data collection

We use two data sets: bottom pressure data from a 14-sensor array collected over a 6.5-day period from 20 to 27 July 2009, during a spring tide phase; and bottom pressure, current velocity, and density data from three of the 14 stations, collected from 20 July through 20 August 2009. The pressure transducers used were Paroscientific Model 6000-200A. These have a resolution of 1.4 Pa (0.00014 dbar) and a full scale output of 1.4×10^6 Pa (140 dbar), and were mounted inside a pressure case that housed electronics, data storage, and batteries (Moum and Nash 2008). The bottom pressure sensors were deployed from the R/V Hugh R. Sharp, forming an

array that covered an area approximately 14 by 12 km (Fig. 2.1). Pressure sensors 6 and 10 to 14 were deployed on bottom landers and remained on the sea floor for about 60 days. Sensors 1 through 5 and 7 through 9 were deployed for one week and were attached to negatively buoyant pressure cases that were dropped to the sea floor, where they remained until a predetermined time, when each pressure case autonomously released a weight, allowing the instrument to float to the surface and be recovered.

The 14-sensor array formed two parallel lines of stations in the alongshore direction and one line of stations in the cross-shore direction (Fig. 2.1). The offshore line refers to the approximately 4.5-km alongshore line (stations 1 through 3), the inshore line refers to the approximately 10-km alongshore line of sensors (stations 4 through 9), and the cross-shore line refers to the approximately 15-km cross-shore line (stations 2, 6, and 10 through 14), as in Fig. 2.1b. Spacing between stations varied from 0.7 to 4.5 km. All pressure sensors sampled at 1-second intervals, except the sensor at station 14, which sampled at 2-second intervals.

Bottom mounted ADCPs (vertical resolution 1 m, sample period 15 s) at stations 6, 10, and 11 provided current velocities. At station 6, 17 thermistors, and at station 11, 14 thermistors, were distributed down the water column (sample period 15 s), and throughout the array, conductivity and temperature (CT) sensors (sample period 15 s) were deployed at different depths. These data allowed us to obtain a temperature-salinity (T-S) relationship for the area as a function of time and background density as a function of time (approximately every 3 hours) and depth at stations 6 and 11. Temperature dominated the density variability, with a strong seasonal thermocline in

this region in summer and early fall.

2.3.2 Data analysis

2.3.2.1 Seafloor pressure

The bottom pressure signal includes barotropic tides (Fig. 2.2a) and surface waves of larger amplitude than the nonlinear internal tide. To isolate the signal of the nonlinear, high-frequency internal wave packets in the internal tide, referred to as IWPs from here on, we band-pass filtered the pressure data using the pl66 filter (Beardsley et al. 1985) with half-amplitude frequencies at 1/120 Hz and 1/1800 Hz, thus retaining periods between 2 and 30 minutes. While this band preserves the variability due to the high-frequency internal wave component of the internal tide, variability from the large-scale internal tide is removed. This is similar to the method used in Moum and Nash (2008). The band-pass filter was applied to the bottom pressure data from each station, and we interpolated each station's data onto a common 1-second time base. We refer to the filtered bottom pressure as P_B (Figs. 2 and 3).

2.3.2.2 High-frequency internal wave packet (IWP) arrival times

Thirteen IWPs passed through the study site over the 6.5-day period (Figs. 2 and 3). Arrival times for IWPs were subjectively defined as the time when the first trough of an IWP passed a particular station. Due to spatial variations in IWP amplitude

across the array, IWPs and therefore arrival times were not always apparent at all stations. Generally, wave packets were most apparent offshore and to the south. A storm that passed through the study site on 24 through 25 July caused large amplitude variability in P_B that was coherent at near zero time lag at all stations and obscured the IWPs during this period (Fig. 2.2, IWPs 8 through 10). We hypothesize that this coherent variability was due to large-scale barotropic motions (e.g., a seiche) within Massachusetts Bay driven by the storm.

2.3.2.3 Comparison to current and temperature data

Comparing the bottom pressure, P_B, to velocity and temperature variations, for example at station 6 (Fig. 2.4), confirms that the wave packet signals apparent in P_B were caused by shoreward-propagating IWPs. The coordinate reference frame was rotated so that the positive x-axis was in the direction of IWP propagation at station 6. Oscillations in P_B line up with oscillations in isotherms and velocities consistent with shoreward propagating high-frequency mode-one internal waves of depression: the positive (negative) horizontal velocities were above (below) thermocline troughs, and downward (upward) currents occurred before (after) the troughs. Note that thermocline displacements of approximately 20 m correspond to oscillations in P_B of 0.04 dbar (equivalent to 4 cm of sea surface displacement).

2.3.2.4 Calculating wave direction and speed

We used two methods to calculate propagation direction, θ, with the second method allowing us to calculate wave speed, c. In the "plane wave method", θ was calculated based on IWP arrival times at stations of an alongshore line (offshore or inshore), assuming the packet propagated across the line with straight phase lines at an assumed speed. This allowed us to quantify changes in θ as each IWP propagated in the cross-shore direction. In the "triangulation method", propagation with straight phase lines is also assumed, but only over groups of three stations forming a triangle. Five triangle groupings were used, and θ and c were calculated for each based on arrival times at the three stations, allowing us to quantify alongshore variation.

In addition, we calculated theoretical linear, mode-one, hydrostatic internal wave phase speeds in the presence of background currents for comparison with the observed speeds. For the theoretical speeds, we used the observed stratification and background currents at station 6 (the method for obtaining background currents is explained in section 2.3.2.5.1.). Note that background currents alter phase speed through both advection and shear.

2.3.2.4.1 Plane wave method for calculating θ

In this method, θ was calculated separately at each alongshore line (offshore and inshore), according to:

$$\theta = \theta_o + \theta_L \equiv \theta_o + \sin^{-1}(m\bar{c})\,, \tag{2.1}$$

where $\theta_o = 243°$ is the direction normal to both alongshore lines and directed onshore, θ_L is the angle between the leading phase line of an IWP and the alongshore array line, $\overline{c}$ is the average wave speed for the IWP (as described in section 2.3.2.4.2.) and m (with units s m^{-1}) is the slope of a line fit to the relationship between arrival time of the IWP at the stations of the alongshore array line versus distance of each station along that line. For example, IWP 5 clearly propagates obliquely relative to both alongshore lines, as it arrives first to the south and later at stations to the north (Figs. 2 and 3). θ is expressed in degrees clockwise from north (for example, northward is 0° and westward is 270°).

Calculating θ for a wave packet at either alongshore line required at least two arrival times along the line so that m could be determined. Consequently, θ could not be determined for IWP 11 at the offshore line or for IWP 10 at the inshore line (Fig. 2.2).

2.3.2.4.2 Triangulation method for calculating θ and c

Here, we followed the method of Scotti et al. (2005) and calculated θ and c based on arrival times at three stations forming a triangle and by minimizing the mean squared error, Φ, between the observed difference in arrival time, Δt_{ij}, between station pairs of the triangle and arrival time differences, $\Delta\hat{t}_{ij}$, for phase lines of a plane wave propagating across the triangle at a particular speed and direction, as follows:

$$\Phi = \sum_{lags} \left(\Delta t_{ij} - \Delta\hat{t}_{ij}\right)^2 = \sum_{lags} \left(\Delta t_{ij} - \frac{\Delta \mathbf{x}_{ij} \cdot \hat{\mathbf{n}}}{c}\right)^2 , \tag{2.2}$$

where $\Delta\mathbf{x}_{ij}$ are horizontal spatial separation vectors between triangle stations, $\hat{\mathbf{n}}$ is a unit normal to phase lines in the direction of wave propagation, and the sum is over all station pairs (three pairs for a triangle). The Gauss-Newton method is used to minimize Φ and determine θ and c.

We used five triangles–N, NC, C, SC, and S (Fig. 2.1b)–to quantify propagation direction and speed variability along wavefronts. These five triangles were chosen to divide the array into regions in the alongshore direction, and using other sets of triangles did not change the overall conclusions. Note that each triangle has two points along the inshore line and only one along the offshore line. This is in order to be consistent when comparing alongshore locations, as all five triangles will have results more representative of the state of the IWPs at the inshore rather than offshore line. Arrival times were required at all three locations within a triangle, thus there are no results for IWPs 9 and 10. The average speed, $\bar{c}$, used for each wave packet in the plane wave method described above is the average of c from all five triangles for that wave packet.

2.3.2.5 Comparing bottom pressure variance to internal wave kinetic energy

The concurrent velocity and bottom pressure data at stations 6, 10, and 11 allow comparison of observed bottom pressure variance and kinetic energy. To better understand their correspondence and to determine whether bottom pressure variance can be used as a proxy for internal wave energy, we first consider linear theory.

2.3.2.5.1 Description of theory

In nonrotating linear theory and to leading order in weakly-nonlinear, weakly-dispersive theory, mode-one internal waves are completely described by an amplitude, $A(x, y, t)$, and vertical structure functions for each field variable, $\phi_\nu(z)$, where ν refers to the two components of velocity (u, in the direction of wave propagation, and w, in the vertical), density perturbations, ρ', and vertical displacements of isopycnals, ξ, associated with the internal wave (Lee and Beardsley 1974; Pedlosky 2003). $\phi_\nu(z)$ are obtained from linear dynamics for either case. For weakly-nonlinear, weakly-dispersive theory, $\phi_\nu(z)$ are determined from hydrostatic theory, and the amplitude time series is governed by weakly-nonlinear, weakly-dispersive evolution of the wave (for example, through variants of the Korteweg de Vries equation; (Benney 1966; Lee and Beardsley 1974)). For the linear case, hydrostatic or non-hydrostatic theory may be applied. Here we define the amplitude to describe the evolution of ξ at the depth of maximum displacement. Thus, $\phi_\xi(z)$ is nondimensional and is normalized so that $\max|\phi_\xi| = 1$.

When considering a particular horizontal location, the amplitude time series governs the variance of a particular field variable and the vertical structure function determines how its variance is distributed vertically. Therefore, a theoretical relationship between internal wave bottom pressure variance, $\langle P_B^2 \rangle_T$, and depth-integrated kinetic energy, $\langle KE \rangle_T$, is straightforward to obtain. Here, the angled brackets refer to averaging in time over a wave period, and the subscript T indicates linear theory. For example, for a non-hydrostatic, linear, mode-one internal plane wave propagating

in a fluid with constant buoyancy frequency N, no background currents, and water depth H, $\langle KE\rangle_T$, $\langle P_B^2\rangle_T$, and their ratio are given by:

$$\begin{aligned}
\langle KE\rangle_T &= \frac{\rho_o}{2}\int_{-H}^{0}\left\langle u^2+w^2\right\rangle dz = \frac{\rho_o}{2}\left\langle A^2\right\rangle \int_{-H}^{0}\left(c^2\left|\frac{d\phi_\xi}{dz}\right|^2+\sigma^2\left|\phi_\xi\right|^2\right)dz = \frac{\rho_o}{4}\left\langle A^2\right\rangle HN^2\,,\\
\left\langle P_B^2\right\rangle_T &= \rho_o^2c^4\left\langle A^2\right\rangle\left|\frac{d\phi_\xi}{dz}\right|^2_{z=-H} = \rho_o^2c^4\left\langle A^2\right\rangle\frac{\pi^2}{H^2}\,,\\
\frac{\langle KE\rangle_T}{\langle P_B^2\rangle_T} &= \frac{N^2H^3}{4\rho_oc^4\pi^2}\,,
\end{aligned} \tag{2.3}$$

where ρ_o is the average background density of the fluid, c is the linear phase speed, and σ is the wave frequency. In the hydrostatic limit, $c = NH/\pi$ and $\langle KE\rangle_T / \langle P_B^2\rangle_T$ simplifies to $H/4\rho_oc^2$. This simple case demonstrates that the relationship between $\langle KE\rangle_T$ and $\langle P_B^2\rangle_T$ will change for changing water depth and stratification.

In our study region, stratification is a function of depth and there are sheared background currents. Only background currents in the direction of wave propagation, $U(z)$, are dynamically important, so we extend the above linear theory to allow for background currents, $U(z)$, and arbitrary stratification, $N(z)$. The relationship becomes:

$$\frac{\langle KE\rangle_T}{\langle P_B^2\rangle_T} = \frac{\left[\int_{-H}^{0}\left(\frac{d\phi_w}{dz}\right)^2dz+\frac{\sigma^2}{c^2}\int_{-H}^{0}\phi_w(z)^2dz\right]}{2\rho_o\left[\left(U(z=-H)-c\right)\left.\frac{d\phi_w}{dz}\right|_{z=-H}-\left.\frac{dU}{dz}\right|_{z=-H}\phi_w(z=-H)\right]^2}\,, \tag{2.4}$$

where the inviscid Taylor-Goldstein equation is used to compute the vertical modes, $\phi_w(z)$, and phase speeds, $c = \sigma/k$, of mode-one linear internal waves. The vertical structure of vertical velocity, $\phi_w(z)$, is related to the vertical structure of isopycnal displacement, $\phi_\xi(z)$, as follows:

$$w = (U(z) - c)\,\frac{d\xi}{dx} = (U(z) - c)\,ikA\phi_\xi = i\sigma A\frac{(U(z) - c)}{c}\phi_\xi = i\sigma A\phi_w\,. \tag{2.5}$$

The imaginary unit number, i, is present because w and ξ are 90° out of phase in time. To leading order, weakly-nonlinear theory gives the same relationship between $\langle KE\rangle_T$ and $\langle P_B^2\rangle_T$ averaged over the time it takes for a wave form to pass a given location.

We use equation (2.4) to explore how the theoretical relationship depends on water depth, stratification, and background currents, and to determine what controls the relationship between observed bottom pressure variance, $\langle P_B^2\rangle_O$, and depth-integrated kinetic energy, $\langle KE\rangle_O$ (method for calculating observed values is described below, in section 2.3.2.5.2.). The Taylor-Goldstein equation is solved numerically (Smyth et al. 2011), using observed background stratification and background currents for each IWP, along with a chosen wave frequency, σ.

The thermistor and CT data revealed that background stratification was horizontally uniform throughout the study area (note, for example, the overlap of average background stratification at stations 6 (55-m) and 11 (35-m) in Fig. 2.5a). Therefore, we used the background stratification from station 6, shortening or lengthening

the profile (with constant density for increased depths) to account for the range of water depths of the array stations. We used the background stratification sample time closest to that of each IWP arrival. The stratification did not change much over the period of this study. In general, the pycnocline was centered at approximately 10-m depth, but before the storm that passed through the study site on 24–25 July, it ranged from about 5–10-m depth, and after the storm, it was slightly deeper, from about 10–15-m depth. The average minimum buoyancy period at the pycnocline during the study was 2 minutes.

In addition, we solved equation (2.4) using an analytical background density profile:

$$\overline{\rho}(z) = \rho_2 - \frac{1}{2}\Delta\rho\left(1 + \tanh\left(\frac{z + D_o}{\mu}\right)\right), \tag{2.6}$$

where $\Delta\rho = \rho_2 - \rho_1$ (4.2 kg m^{-3}), ρ_1 and ρ_2 (1025.2 kg m^{-3}) are the upper and lower density extremes, respectively, z goes from $-H$ (55 m) to the sea surface (0 m), D_o (12.5 m) is the depth of the center of the pycnocline, μ (7.5 m) is a measure of the thickness of the pycnocline, and base parameters were chosen to produce a stratification similar to the time average of stratification observed at station 6 (Fig. 2.5a). Parameters $\Delta\rho$, D_o, and μ were varied to test sensitivity of results to changes in stratification.

Background currents $U(z)$ for each IWP at stations 6, 10, and 11 were obtained by low-pass filtering the currents to allow periods of variability greater than 30 minutes to remain in the data (thus retaining the low-frequency barotropic and internal tides)

and time-averaging the remaining currents over 2-hour periods concurrent with each of the observed IWPs in P_B. The background current structure was similar for all of the IWPs and at all three stations. This is because the internal tide envelope, to which the high-frequency IWPs are phase-locked, dominates background currents. On average, $U(z)$ currents were in the direction of wave propagation above the pycnocline and against wave propagation below the pycnocline (Fig. 2.5b). In addition, the average background current profile, $\overline{U}(z)$, and variations on it were used to test the sensitivity of results to changes in background currents.

2.3.2.5.2 Calculating observed bottom pressure variance and kinetic energy

Observed bottom pressure variance of each IWP, $\langle P_B^2 \rangle_O$, was calculated for all 14 stations. The total variance in P_B over time periods with IWPs (var_{IW+BG}) is due to both the IWPs and background variance due to other processes and instrument noise. Therefore, we isolated the bottom pressure variance due to each IWP as:

$$\left\langle P_B^2 \right\rangle_O \equiv var_{IW+BG} - var_{BG}\,. \tag{2.7}$$

var_{BG} is background variance calculated separately for each IWP at each sensor location over two-hour periods with no discernable IWPs just prior to the arrival of each packet at the array. For example, var_{BG} for IWP 2 was calculated over the period between the vertical dashed lines in Fig. 2.2. IWP 1 arrived at the array at

the start of the time series; therefore, we used var_{BG} from IWP 2.

To calculate var_{IW+BG}, we used a common period of time for all stations for each IWP, beginning just before the IWP's earliest arrival in the array and ending just before the earliest arrival of the next IWP. This resulted in time spans ranging from 11.7 – 13.1 hours, thus also including the variance of P_B over long periods during which there were no IWPs present. To account for this, we scaled the results by multiplying by 12.42 hours/2 hours, as the IWP variance is primarily contained within 2-hour periods.

We did not calculate bottom pressure variance for IWP 13 because the data set ended before the packet had passed through the array (Fig. 2.2). The storm on 24–25 July caused the background variance to vary significantly, making it challenging to properly remove background variance over this period (Fig. 2.2). Thus, we did not use results for IWPs 7 and 8. Some estimates of $\langle P_B^2 \rangle_O$ are below zero due to uncertainties in background variance.

Observed time-averaged, depth-integrated kinetic energy, $\langle KE \rangle_O$, was calculated for each IWP at stations 6, 10, and 11, using current velocities aligned with wave propagation direction (u) and in the vertical direction (w), measured at each station from 20 July through 20 August, 2009. Velocities u and w were band-pass filtered by the same method used for bottom pressure. Similar to the method for calculating $\langle P_B^2 \rangle_O$, we removed mean background kinetic energy calculated from 2-hour periods during which there were no discernable IWPs, just prior to each IWP arrival in this one-month period. Because we could identify arrival times in the ADCP data for all IWPs in the one-month period, for this comparison, we calculated mean IWP kinetic

energy and var_{IW+BG} for each IWP over a unique 2-hour period.

2.4 Results

2.4.1 Internal wave properties from the processed bottom pressure

The properties and variability of the IWPs revealed in the band-pass filtered bottom pressure record, P_B, agree with previous studies of high-frequency internal waves in the region. An IWP propagated through the study region each tidal cycle, arriving at the array between 15 minutes before and 50 minutes after high tide at station 1, with an interval of 11.7 to 13.1 hours between each IWP (Fig. 2.2). Each IWP had about 10 waves within its packet (ranging from about 2 to 15), with high-frequency periods ranging from 4 to 18 minutes. It took approximately 2 hours for each IWP to transit each station location and about 10 hours for each IWP to propagate through the array. Within P_B, the amplitude of the pressure oscillations caused by the IWPs ranged from 0.0036 to 0.058 dbar. IWPs were detected at all 14 stations, but were most commonly identifiable for the stations offshore of the 40-m isobath and for the more southern of those stations (Figs. 1–3).

2.4.2 Wave direction and speed

2.4.2.1 Plane wave results for θ

For the plane wave method (equation (2.1)), θ varied from packet to packet, and each IWP turned to a more westward direction (rotated clockwise) while propagating from the offshore to the inshore line (Fig. 2.6). All IWPs propagated to the southwest, consistent with previous studies of the region. At the offshore line, θ ranged from 239° to 261° for all IWPs except one outlier (IWP 12, $\theta = 192°$). At the inshore line, θ ranged from 249° to 263°. Clockwise rotations of θ from offshore to inshore (excluding IWP 12) were from 1.1° to 13.4°, with a mean of 6.9° and a standard deviation of the mean of 1.4°, showing that the clockwise rotation was statistically significant. Packet-to-packet variations were correlated between the offshore and inshore lines.

2.4.2.2 Triangulation results for θ and c

The propagation direction results from the triangulation method were similar to the plane wave results, with θ from 241°–282° (Figs. 6 and 7a). Consistent with previous studies, these results show that the wavefronts were approximately straight to somewhat radially spreading (θ increasing to the north) away from Stellwagen Bank (the generation site), with variability between packets. There was a mean 14.2° clockwise rotation of phase lines from triangle S (253.2°) to triangle N (267.4°). However, only three IWPs had results at triangle N, with more results for the more southern triangles, so the mean is not representative of all IWPs (yellow squares, Fig.

2.7a).

For each IWP, we averaged its triangulation direction results over all five triangles and compared these averages (Fig. 2.6, grey dots) to the plane wave direction results at the inshore line to see if the two methods capture similar changes from packet to packet. We chose to statistically compare the mean triangulation results only to the inshore line results because the wave directions calculated by the triangulation method are more influenced by arrival times at the inshore line because each triangle contains two stations of the inshore line and only one station of the offshore line. Regressing the mean triangulation results onto the results at the inshore line resulted in a slope of 0.87, with a 95% confidence interval of $+/-$ 0.20, and an r-squared of 0.92, with a 95% significance level of 0.36, showing that the results between both methods are highly correlated. The RMS difference between θ estimated at the inshore line using the plane wave method and θ from the triangulation method is 1.4°, while the packet-to-packet standard deviation in θ is greater, at 4.8°. Therefore, we conclude that packet-to-packet variability in θ is detectable by both methods (Fig. 2.6).

Large packet-to-packet differences in wave speed, c, were observed using the triangulation method (0.36 m s^{-1}–0.63 m s^{-1}), consistent with previous studies of the region (Fig. 2.7b). More subtle differences in c were observed for particular wave packets in the N-S direction. Generally, c decreased from south to north along the array, on average 0.046 m s^{-1} slower at triangle N than at S (decreased from 0.55 m s^{-1} to 0.50 m s^{-1}).

We estimate an outer limit of error in arrival times of 10 minutes (the approximate temporal spacing between troughs). Adding random error of standard normal

distribution with a 5-minute standard deviation (10 minutes out to two standard deviations) to arrival times based on a chosen known direction and speed results in a standard deviation of +/− 3.5° for direction and +/− 0.021 m s^{-1} for speed. Based on this maximum error, the variability in the triangulation results is robust.

Not surprisingly, observed wave speed estimates are higher than predicted for a theoretical linear, mode-one, hydrostatic internal wave in the presence of background currents. Using observed stratification and background currents at station 6 over the 6.5-day study gave a mean theoretical phase speed of 0.47 m s^{-1} (standard deviation 0.09 m s^{-1}). To compare observations to this, we averaged the triangulation method speed results over triangles S, SC, and C, since they are near to and/or include station 6 (Fig. 2.1). The mean speed of the observations, 0.53 m s^{-1} (standard deviation 0.06 m s^{-1}), was 1.1 times greater than the mean theoretical phase speed, likely because the observed speeds are calculated over an area with greater depth than at station 6 (Fig. 2.1) and because the waves are large amplitude, and thus predicted to be faster than linear internal waves. Without background currents, the theoretical speed is slightly, though not significantly, slower, at 0.45 m s^{-1} (standard deviation of 0.02 m s^{-1}), 1.2 times smaller than the mean observed speed. These ratios are the same as found by Alford et al. (2010) for observed nonlinear internal wave speeds versus calculated linear phase speeds in the South China Sea. They attribute the difference to the larger amplitudes (and thus, nonlinearity) of the observed waves.

2.4.3 Bottom pressure variance and internal wave kinetic energy

As a baseline for comparing observations to linear theory, we define α, the theoretical ratio of internal wave kinetic energy to bottom pressure variance as in equation (2.4), but in the hydrostatic limit, with no background currents:

$$\alpha \equiv \left(\frac{\langle KE \rangle_T}{\langle P_B^2 \rangle_T} \right) \Bigg|_{Hydrostatic,\, no\, currents} = \frac{\int_{-H}^{0} \left(\frac{d\phi_w}{dz} \right)^2 dz}{2\rho_o c^2 \left(\frac{d\phi_w}{dz} \right) \Big|_{z=-H}^{2}} . \tag{2.8}$$

We compute α numerically, using the average observed buoyancy frequency profile during this study from station 6, yielding the single value 0.190 m^3 N^{-1}. We use this to scale comparisons between kinetic energy and bottom pressure variance such that they give a measure of deviation from hydrostatic linear theory in the absence of background currents. That is, the ratio of kinetic energy over α multiplied by bottom pressure variance (see equation (2.10), section 2.4.3.2.) gives a dimensionless value that equals one when the relationship between kinetic energy and bottom pressure variance matches that of hydrostatic linear theory without background currents, and deviates from one when that theory is not satisfied.

For example, we performed linear regressions between scaled observed bottom pressure variance, $\alpha \langle P_B^2 \rangle_O$, and kinetic energy predicted from linear hydrostatic theory, $\langle KE \rangle_P$, with no background currents and using the background stratification observed during the passage of each IWP (see section 2.3.2.5.1.). That is, for each IWP, we use the observed bottom pressure variance, $\langle P_B^2 \rangle_O$, and the theory (equation (2.4)) to predict the kinetic energy of each IWP, as follows:

$$\langle KE \rangle_P \equiv \left(\frac{\langle KE \rangle_T}{\langle P_B^2 \rangle_T} \right) \left\langle P_B^2 \right\rangle_O . \tag{2.9}$$

The slight deviation of the results from a one-to-one line demonstrates the minor influence of variations in stratification during the study period (Fig. 2.8, blue symbols; Table 1, row 2).

We note that when non-hydrostatic theory is applied (and the wave period is assumed to be 18 minutes), the theoretical ratio between kinetic energy and bottom pressure variance is 1.2 times greater than the α predicted from hydrostatic theory. The difference increases when shorter wave periods are used.

2.4.3.1 Observed and theoretical relationship

Linear regressions between observations of IWP kinetic energy, $\langle KE \rangle_O$, and scaled bottom pressure variance, $\alpha \langle P_B^2 \rangle_O$, have strong correlations (Fig. 2.8, black line; Table 1, row 1), demonstrating a linear relationship between kinetic energy and bottom pressure variance for IWPs at each of the three stations (6, 10, 11). However, the slopes of the regressions are much smaller than 1, indicating that for a given bottom pressure variance, observed kinetic energy is 20–30% of that predicted by hydrostatic linear theory in the absence of background currents.

When observed background currents were included in predicting kinetic energy, $\langle KE \rangle_P$, for each IWP, slopes significantly decreased compared to theory without background currents, bringing the predicted values closer to those observed (Fig. 2.8, red line; Table 1, row 3). These theoretical slopes were only between 1.3 to 1.7

times larger than the observed slopes. These results demonstrate the importance of background currents on the relationship between bottom pressure variance and kinetic energy.

Water depth also affects the relationship between kinetic energy and bottom pressure variance, as demonstrated by the decrease in slopes with water depth (Table 1). The only result to violate this was the observed slope at the shallowest station (station 11), which was larger than at the next deepest station (station 10). This inconsistency is attributed to the limited range of $\langle P_B^2 \rangle_O$ at station 11, where the maximum $\langle P_B^2 \rangle_O$ was 3730 Pa^2, while at stations 6 and 10, values ranged to greater than 7300 Pa^2. When we exclude IWPs with $\langle P_B^2 \rangle_O > 3730$ Pa^2, regression slopes decrease with decreasing station depth (not shown).

2.4.3.2 Sensitivity to background conditions

To explore the sensitivity of the relationship between kinetic energy and bottom pressure variance to background conditions, we explored how the theoretical relationship varies over a range of water depths, background currents, and stratifications (Table 2). For these analyses, we compute equation (2.4) scaled by $1/\alpha$,

$$\beta \equiv \frac{1}{\alpha} \left(\frac{\langle KE \rangle_T}{\langle P_B^2 \rangle_T} \right) , \tag{2.10}$$

and compare values computed by varying a particular background condition (e.g. depth) while keeping the others constant (e.g. currents and stratification). When $\beta < 1$, for example, kinetic energy for a given bottom pressure variance is less than

what would be predicted by hydrostatic linear theory without background currents and with the average observed stratification.

To explore the effect of water depth, we computed β across the range of depths of the array stations (18–75 m), neglecting background currents and using the time-averaged observed stratification profile from station 6 (Fig. 2.5a), shortening or lengthening the profile to account for the range of depths. With water depth decreasing from 75 to 18 m, β decreases almost linearly with depth, from 1.5 to 0.44. This means that for a particular value of bottom pressure variance, kinetic energy decreases with decreasing water depth.

These analyses show that β is very sensitive to shear in background currents aligned in the direction of wave propagation. The results are consistent between stations 6, 10, and 11, but are only shown for station 6 (Table 2), for which we use the average observed background current profile, $\overline{U}(z)$, (Fig. 2.5b) scaled to different magnitudes, and the fixed analytical density profile, $\overline{\rho}(z)$ (Fig. 2.5a). When the background current is varied from $1.5U(z)$ to $-1.5U(z)$, β varies by over an order of magnitude, from 0.40 to 5.7 (Table 2). It is the vertical shear in the background currents that has an effect on β: when a vertically uniform background current is used, it has no effect on the ratio compared to neglecting background current; and when a background current profile with shear is uniformly increased or decreased, it does not change the ratio (e.g. $\overline{U}(z) + 0.2$ m s^{-1} versus $\overline{U}(z)$ (not shown)). If the background currents are in the direction of wave propagation above the pycnocline and against it below the pycnocline, decreasing in magnitude over the deepest $\sim$10 m, as they were for the IWPs observed, shear is generally positive for the majority

of the water column, becoming negative for the deepest ∼10 m, and β is less than 1. Considering these results, it is clear that if the observed background current shear had not been similar for all IWPs (Fig. 2.5b), then the observed linear relationship between $\langle KE \rangle_O$ and $\langle P_B^2 \rangle_O$ (Fig. 2.8, Table 1) would not have occurred. That is, the phase-locking of the IWPs to the internal tide acts to consistently decrease the ratio of kinetic energy to bottom pressure variance and thus contributes to the significant linear regression between them.

Finally, variations on the analytical density profile $\overline{\rho}(z)$ produced small increases and decreases (by 4 to 21%) in β (Table 2). This is consistent with the significant regressions between $\langle KE \rangle_O$ and $\langle P_B^2 \rangle_O$, despite the small variations in stratification during the study period.

The results make it clear that the relationship between bottom pressure variance and kinetic energy of an IWP is sensitive to total water depth, background shear, and stratification. Thus, without observations of stratification and currents, it is not possible to convert observations of bottom pressure variance to high-frequency internal wave kinetic energy. Therefore, the results can only be analyzed relative to these constraints. However, even with these limitations, bottom pressure variance measurements do tell us something about the relative kinetic energy between IWPs and spatially. This is because we know the station depths; we know the stratification is horizontally uniform; and we know that the background currents are similar due to the phase-locking of the IWPs to the internal tide.

2.4.3.3 Observations of bottom pressure variance for the entire array

$\langle P_B^2 \rangle_O$ generally decreased to the north along wavefronts, especially north of the cross-shore line (Fig. 2.9). Average $\langle P_B^2 \rangle_O$ increased as IWPs propagated from the offshore to the inshore line and greatly decreased shoreward from there (Fig. 2.10). IWPs during the first half of the study tended to have higher values of $\langle P_B^2 \rangle_O$.

Along the offshore line, average $\langle P_B^2 \rangle_O$ for each station decreased to the north from 3,354 Pa^2 to 1,115 Pa^2, and individual $\langle P_B^2 \rangle_O$ ranged from 0 to 9,365 Pa^2 (Fig. 2.9a). Along the inshore line, average $\langle P_B^2 \rangle_O$ ranged from 505 Pa^2 to 3,765 Pa^2, and the maximum individual $\langle P_B^2 \rangle_O$ was for IWP 5 at station 5, at 13,358 Pa^2, with all other values being below 7,225 Pa^2 (Fig. 2.9b). In the cross-shore direction, the average increase of $\langle P_B^2 \rangle_O$ from station 2 to 6 (2,147 Pa^2 to 3,216 Pa^2) was similar in magnitude to the decrease from station 6 to 10, while the decrease from station 10 to 11 was about twice as large (Fig. 2.10). Shoreward of station 11, for water depths less than 40 m, average $\langle P_B^2 \rangle_O$ remained small.

2.4.3.4 Relative kinetic energy from observations of bottom pressure variance

In section 2.4.3.2., we demonstrate that the relationship between kinetic energy and bottom pressure variance has a strong dependence on water depth. Here we address the question of whether the observed changes in bottom pressure variance are strictly due to variations in water depth, with kinetic energy of an IWP remaining

constant as it propagates across the array. We note that stratification is roughly constant across the array (Fig. 2.5a) and that background currents were not measured at every station. Therefore, we use linear hydrostatic theory with horizontally uniform stratification based on mean stratification observed at station 6 (Fig. 2.5a) and neglect background currents, but with varying water depth to predict how bottom pressure variance would change across the array if kinetic energy of an IWP remained constant (equation (2.4)).

For both alongshore lines, water depth increases to the north (Fig. 2.1). At the offshore line, linear hydrostatic theory predicts that bottom pressure variance would decrease to the north by 29% from station 1 to 3 for an IWP with constant kinetic energy, due to changes in water depth (Fig. 2.9a, black lines). This is somewhat consistent with mean observed variations of bottom pressure variance, suggesting that kinetic energy of IWPs is not varying much across the offshore line on average. However, individual packets do part from this trend, with some packets (e.g. IWPs 5 and 6) having significantly greater kinetic energy to the south, and one packet (IWP 3) increasing in kinetic energy to the north. At the inshore line, theory predicts that bottom pressure variance would decrease to the north (21% from station 4 to 9) for an IWP with constant kinetic energy (Fig. 2.9b, black lines). On average, the changes in $\langle P_B^2 \rangle_O$ are greater, suggesting that kinetic energy is generally greater to the south, but with several IWPs increasing in kinetic energy before decreasing to the north.

In the cross-shore direction, linear theory predicts that bottom pressure variance would increase onshore with decreasing water depth if kinetic energy remained constant (Fig. 2.10b, black lines). While an increase in $\langle P_B^2 \rangle_O$ toward the coast is

observed between the two offshore stations, the abrupt drop in $\langle P_B^2 \rangle_O$ at approximately the 45-m isobath ($x \approx -1$ km) indicates that the kinetic energy of IWPs decreases abruptly at that cross-shore location, consistent with the observed drop in IWP kinetic energy from stations 6 to 11 (Fig. 2.10b, yellow diamonds). The large increase in $\langle P_B^2 \rangle_O$ for IWPs 1, 3, and 4 from station 2 to 6 indicates large increases in high-frequency kinetic energy. Results showed that the same IWPs that have larger $\langle P_B^2 \rangle_O$ also have larger $\langle KE \rangle_O$, indicating that wave-to-wave variations in $\langle P_B^2 \rangle_O$ likely represent similar wave-to-wave differences in kinetic energy (not shown).

2.5 Discussion

2.5.1 Spatial variations in wave direction and speed

A question to consider is whether the clockwise rotation of wavefronts while propagating shoreward from the offshore to the inshore line, as seen in the plane wave results, is due to topographic refraction (for example, note the change in the orientation of the 80, 70, and 60-m isobaths in Fig. 2.1). The effects of topographic refraction depend on the initial propagation direction of the waves relative to isobaths. Comparing the plane wave direction results (Fig. 2.6) to the isobaths (Fig. 2.1) shows that for all but IWP 12, the propagation directions at the offshore line were such that refraction (bending of shoaling wavefronts to align with bathymetry) would cause rotation of the waves in the opposite direction to that observed.

Another consideration is that in equation (2.1), the same value for $\bar{c}$ was used

whether solving for the offshore or inshore line. But, the water is deeper at the offshore line than at the inshore line, and therefore it is likely that wave speeds at the offshore line were slightly greater. Using larger $\overline{c}$ for the offshore line would increase θ for cases with a positive m, potentially eliminating the rotation seen. The increase for theoretical propagation speed in 75-m of water depth versus 55-m of depth, using linear theory with observed background stratification and no background currents, is approximately 0.05 m s^{-1}. Using this speed increase at the offshore line still gave results with clockwise rotation of the waves. When asking the question of what values of $\overline{c}$ would be required to increase θ at the offshore line to yield equal results to the inshore line, we found that for the ten IWPs with results at both lines, the required values of $\overline{c}$ were not physically possible for at least five of the IWPs. For example, for IWP 6, $\overline{c}$ would have to be 5.7 m s^{-1}. For the other five IWPs, required increases in $\overline{c}$ ranged from 0.07 to 0.32 m s^{-1}. So, while it is possible that some of the clockwise rotation of θ may be due to using the same values for $\overline{c}$ at both alongshore lines, it is unlikely that this accounts for all of the rotation.

A third consideration for the clockwise rotation is that curved wavefronts, as indicated by the triangulation results, could be responsible for the apparent change in direction from the offshore to the inshore line: the array elements might be seeing different parts of the curved fronts. Curvature and radial spreading are consistent with SAR images discussed by Butman et al. (2006). They noted that the long, continuous, curved internal wave surface slick features in SAR imagery of the region–that were concurrent with the internal waves observed in situ along a cross-shore transect–suggest that internal waves spread radially away from their finite generation

region at Stellwagen Bank. Note, for example, that the alongshore direction results for IWP 5 (Fig. 2.7a, magenta line) are generally consistent with radial spreading, and that this alongshore variability explains the deviations of arrival times from the dashed lines in Fig. 2.3.

The waves being generally faster to the south along their wavefronts, as indicated by the triangulation results, would also contribute to the clockwise rotation from offshore to inshore. This speed variability is not consistent with shoaling, as the water is deeper to the north (Fig. 2.1), where theory would predict the waves would be faster. However, it could be due to the nonlinear waves having larger amplitudes to the south.

Another potential cause of spatially non-uniform propagation direction and speed could be related to spatially non-uniform barotropic tidal advection. da Silva and Helfrich (2008) saw a clockwise curling of westward propagating internal wavefronts in SAR imagery of internal waves generated in Race Point Channel, north of Cape Cod (Fig. 2.1a). Their current measurements revealed a gradient of barotropic tidal currents through the channel, and they determined that advection of one end of internal wavefronts was stronger than at the other, resulting in curved wavefronts. Our bottom pressure study, however, does not provide data to address this effect.

A three-dimensional numerical model is necessary to distinguish the causes of the observed spatial variations in internal wave propagation direction and speed and to determine the relative importance of the finite extent and spatial irregularity of the source, shoaling by local bathymetric variability, wave nonlinearity, and spatially non-uniform barotropic advection.

2.5.2 Bottom pressure variance versus kinetic energy

The linear analyses and observations reveal that the relationship between high-frequency internal wave kinetic energy and bottom pressure variance depends strongly on water depth and shear of background currents, $U(z)$, and also depends on stratification. As such, it was not possible to use bottom pressure observations as a proxy to quantify kinetic energy, and thus it was not possible to quantify internal wave energy flux and flux divergence from the pressure array.

However, given the strong sensitivity to background shear (Table 2), the observed high correlation between bottom pressure variance and kinetic energy is surprising. This high correlation is likely due to the fact that the high-frequency waves are phase-locked to the internal tide, with each IWP experiencing similar background currents of the internal tide (Fig. 2.5b). The high correlation allows the array to be used qualitatively to describe variations in high-frequency internal wave kinetic energy.

2.5.3 Spatial variations in high-frequency internal wave kinetic energy

IWPs were consistently observed in the study region in water depths greater than ~ 40 m, with a large reduction in high-frequency internal wave kinetic energy as the waves propagated between water depths of 30–50 m, such that they were not consistently detected in water depths shallower than ~ 40 m. The only IWP tracked all the way shoreward through the array was IWP 1. This study and previous studies at this location (modeling and observations) show no evidence of reflection. Though SAR data have not shown internal wave signatures inshore of the 40-m isobath (But-

man et al. 2006), in situ observations of internal waves at the 25-m isobath (Scotti and Pineda 2004) and 2-D modeling of the shoaling of these internal waves in water depths around 40 m (Scotti et al. 2008) indicate that internal waves do propagate shoreward of this depth, but that they change frequency content and structure.

Scotti et al. (2008) showed that transformation of the nonlinear internal tide upon shoaling in Massachusetts Bay is strongly dependent on wave amplitude and pycnocline depth, and whether or not vertical displacements exceed the critical mid-level depth where internal waves would switch polarity (Helfrich et al. 1984). Scotti et al. (2007) showed that weaker barotropic tidal forcing produces smaller amplitude high-frequency internal wave packets. For weak forcing and a shallow pycnocline, the undular bore is not modified strongly until it reaches close to shore (water depth < 25 m), but for larger amplitude forcing and a deeper pycnocline, there are strongly nonlinear modifications to the undular bore with shoaling near the 45-m isobath, with strong loss in energy of the high-frequency waves of depression as the bore evolves into a large-scale rarefaction wave with high-frequency waves of elevation on its trailing end and the possibility for high-frequency waves of depression at its front end (Scotti et al. 2008). This is generally consistent with what we observed. Our study occurred during a spring tide phase, but barotropic tides were weakest at the very beginning of the study. As well, the pycnocline was slightly shallower at the beginning of the study. This is likely why we were able to detect IWP 1 all the way shoreward through the array but not any others. The high-frequency content of the first internal tide, IWP 1, persisted through the array, either due to a lack of strong modification as it propagated shoreward, or potentially to energetic high-frequency

waves of depression at the front and waves of elevation at the back of a rarefaction wave, but the other undular bores lost much of their high-frequency energy while their low-frequency rarefaction wave continued to propagate onshore. For example, in looking at the velocity data at stations 10 and 11 and the isotherms at station 11, it is clear that the internal waves do persist at both stations, and that they evolve from nonlinear internal tides containing high-frequency nonlinear wave packets (e.g. Fig. 2.4) into nonlinear internal tides with little to no high-frequency content (e.g. Fig. 2.11). If there were high-frequency waves present at the shallower stations, they were likely low in energy, as we could not detect them.

The evolution from high to low frequency content with shoaling is at least in part responsible for the large decrease in high-frequency internal wave kinetic energy near the 40-m isobath (Fig. 2.10b, yellow diamonds). It is not clear how much of the high-frequency kinetic energy is transformed to turbulence. Bottom pressure data alone are not sufficient to determine where the energy goes, as they can only be used to identify the high-frequency component of the nonlinear waves. However, the bottom pressure data allow for an upper limit estimate of energy loss for high-frequency internal waves to turbulence.

Looking to the velocity data, the average observed high-frequency kinetic energy of the IWPs decreased by 189 J m^{-2} from station 6 to station 11 (from 211 to 22 J m^{-2}; Fig. 2.10b). These values and those of individual IWPs are similar to energy calculations done for the same region by Scotti et al. (2006). Assuming equipartition and using average group velocities and the distance between the two stations gives a flux divergence of -0.1244 W m^{-2}. If all of this energy loss was due to dissipation, this

would give a depth-averaged dissipation rate, ϵ, of $O(10^{-6})$ W kg^{-1}.

Our results also indicate variation in high-frequency internal wave kinetic energy in the alongshore direction. On average, if background currents and stratification were horizontally uniform, high-frequency internal wave kinetic energy was greater at the southern and central stations of the alongshore lines than to the north along wavefronts. Perhaps energy is focused near the bathymetric ridge seen along the 40-m isobath (Fig. 2.1).

2.5.4 Wave-to-wave variability

Wave-to-wave variability in properties is likely related to differences in barotropic tidal forcing strength and stratification structure, as described by previous studies (Scotti et al. 2007, 2008; Lai et al. 2010). The barotropic tides during the study were mixed semidiurnal/diurnal for the first nine IWPs, also increasing in overall amplitude during the study, with IWPs 1, 3, 5, 7, and 9 generated on relatively stronger ebb tides and IWPs 2, 4, 6, and 8 generated on relatively weaker ebb tides. After IWP 9, the observed tides had less diurnal inequality (Fig. 2.2a). The stratification changed slightly during the study, most notably from the 24–25 July storm that caused the pycnocline to deepen by about 5 m. Speed and direction results had a somewhat striking alternating pattern of wave-to-wave variability for the beginning of the study period, perhaps explained in part by alternating mixed barotropic tides during that period. Plane wave and averaged triangulation direction results regularly decreased and then increased between IWPs, alternating as such for the first six IWPs (Fig.

2.6). Speeds alternated in a similar way for IWPs 1 through 7 (Fig. 2.7b). Pressure amplitude (wave energy) was generally smaller (weaker) after the storm, likely affected by the change in stratification.

For the triangulation method, the three IWPs (3, 5, and 7) with results at all five triangles have the most influence on the trend of the mean results. The means suggest a particular trend in curvature (consistent with radial spreading) and a particular trend in alongshore speed variability (fastest in the southern extent). However, the direction results suggest that most IWPs, including 3 and 7, have somewhat flat wavefronts, while 5 and 6 have a lot of curvature. The alongshore trend of the speed results is less variable between IWPs, and thus the mean trend is more robust.

2.6 Conclusions

A two-dimensional array of bottom pressure sensors was successfully used to identify the passage of high-frequency nonlinear internal wave packets through the study region, to quantify alongshore and cross-shore variations in internal wave propagation direction and speed, and to qualitatively describe variations in high-frequency internal wave kinetic energy based on its relationship to bottom pressure variance.

This research goes beyond previous studies in that we used only bottom pressure sensors to study internal wave properties and in that the two-dimensional array allowed us to obtain details of alongshore (along wavefront) as well as cross-shore variation of high-frequency internal wave direction, speed, and energy. The extension into two dimensions made it possible to triangulate direction and speed using just

the pressure sensors, without a propagation direction needing to be assumed or found through other data. The analysis of the relationship between bottom pressure variance and kinetic energy made it possible to estimate relative high-frequency internal wave energy variations. Although the relationship was found to be highly sensitive to background shear and water depth changes, and also dependent on stratification, the observations still had a strong relationship between kinetic energy and bottom pressure variance due to the phase-locking of the IWPs to the internal tide, causing the IWPs to experience the same background current, and due to the horizontally uniform and relatively similar stratification throughout the study.

We found clear patterns in alongshore and cross-shore spatial variability in the properties of the IWPs. The IWPs all propagated to the southwest, but the wavefronts rotated clockwise as they propagated shoreward from the offshore to inshore line. There was curvature along the wavefronts, ranging from approximately straight to radially spreading. Propagation speeds were faster toward the southern end of the alongshore lines. Pressure amplitude and high-frequency wave energy were generally greater toward the south. With propagation from the offshore to the inshore line, pressure amplitude and high-frequency wave energy generally increased during the beginning of the study (for the first four or five IWPs) and generally decreased during the second half of the study. Shoreward from there, pressure amplitude and high-frequency wave energy decreased, greatly so shoreward of the 40-m isobath.

One drawback of using only an array of bottom pressure sensors to study these internal tides is that it only allows detection of the high-frequency component, so we could not detect the low-frequency component that continues to propagate toward

shore after shoaling. In the bottom pressure data, the baroclinic motions could only be isolated from the barotropic within the frequency band used; the lower frequency internal tide component could not be distinguished from the barotropic tide. Another drawback is that bottom pressure variance could only yield qualitative variability of high-frequency internal wave kinetic energy and it could only do so due to the relatively similar background currents and stratification for each IWP and throughout the array.

2.7 Acknowledgements

We wish to thank Zen Kurokawa for collection and processing of the pressure data, Emily Shroyer for discussions on internal wave energy, and Bill Smyth for the use of his Taylor-Goldstein equation code. We thank the two anonymous reviewers for their helpful comments. Funding provided by the National Science Foundation (Grants 0424742 (JAL), 1155799 (JAL), and 0751930 (JNM)) and the Office of Naval Research (JNM). Data used for the analyses can be provided by the corresponding author, Jenny Thomas (jthomas@coas.oregonstate.edu).

Table 2.1: Linear fits between $\langle KE \rangle_O$ and $\alpha \langle P_B^2 \rangle_O$ [a]

Source of $\langle KE \rangle$	55-m mooring (St. 6)			45-m mooring (St. 10)			35-m mooring (St. 11)		
	R^2	Slope	C.I.	R^2	Slope	C.I.	R^2	Slope	C.I.
$\langle KE \rangle_O$	0.89	0.298	0.0282	0.87	0.207	0.0243	0.60	0.215	0.0552
$\langle KE \rangle_P$; U=0; $N(z,t)$	0.98	0.965	0.0360	0.98	0.778	0.0373	0.91	0.655	0.0666
$\langle KE \rangle_P$; $U(z,t)$; $N(z,t)$	0.88	0.401	0.0381	0.90	0.355	0.0355	0.85	0.333	0.0443

[a] $\langle KE \rangle_P$ were computed using hydrostatic theory (equation (2.9)). All R^2 values are above their respective critical values with 95% confidence. C.I. are confidence intervals of slopes.

Table 2.2: Sensitivity of β to background currents and stratification[b]

$U(z)$	$\rho(z)$	β
Testing changes to $U(z)$		
0	$\bar{\rho}(z)$	1.00
$\bar{U}(z)$	$\bar{\rho}(z)$	0.510
$-\bar{U}(z)$	$\bar{\rho}(z)$	2.77
$1.5\bar{U}(z)$	$\bar{\rho}(z)$	0.395
$-1.5\bar{U}(z)$	$\bar{\rho}(z)$	5.66
Testing changes to $\bar{\rho}(z)$		
$\bar{U}(z)$	$\mu = 3$	0.530
$\bar{U}(z)$	$\mu = 12$	0.488
$\bar{U}(z)$	$D_o = 10$	0.618
$\bar{U}(z)$	$D_o = 15$	0.430
$\bar{U}(z)$	$\Delta\rho = 3.2$	0.618
$\bar{U}(z)$	$\Delta\rho = 5.2$	0.436

[b] Calculations for β (equation (2.10)) were done for 55-m depth (St. 6), using hydrostatic theory. Base parameters for $\bar{\rho}(z)$ (equation (2.6)) are: $\mu = 7.5$ m; $D_o = 12.5$ m; and $\Delta\rho = 4.2$ kg/m^3.

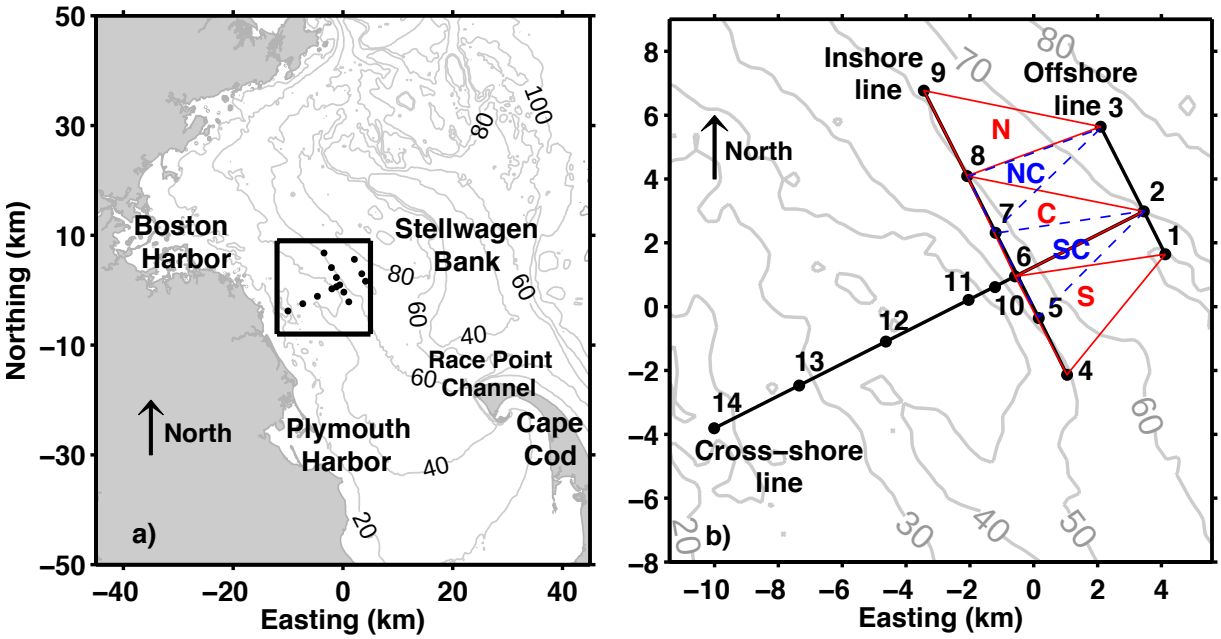

Figure 2.1: (a) Map of study region in Massachusetts Bay. Origin is 42.2350° N, 70.5380° W, and map ranges from 41.78 to 42.68° N and 69.99 to 71.09° W. Stellwagen Bank is seen in the right, central region of the map, and station locations of bottom pressure sensors are indicated by black dots, enclosed within a black box. (b) Expansion of boxed region in (a). Black dots and numbers indicate station locations and numbers. Black solid lines and labels indicate the offshore, inshore, and cross-shore lines. Red and blue lines and labels N, NC, C, SC, and S indicate the northern, north-central, central, south-central, and southern triangle groupings used to compute θ and c via equation (2.2), made of the following station groupings, respectively: [3 8 9], [3 7 8], [2 6 8], [2 5 7], and [1 4 6].

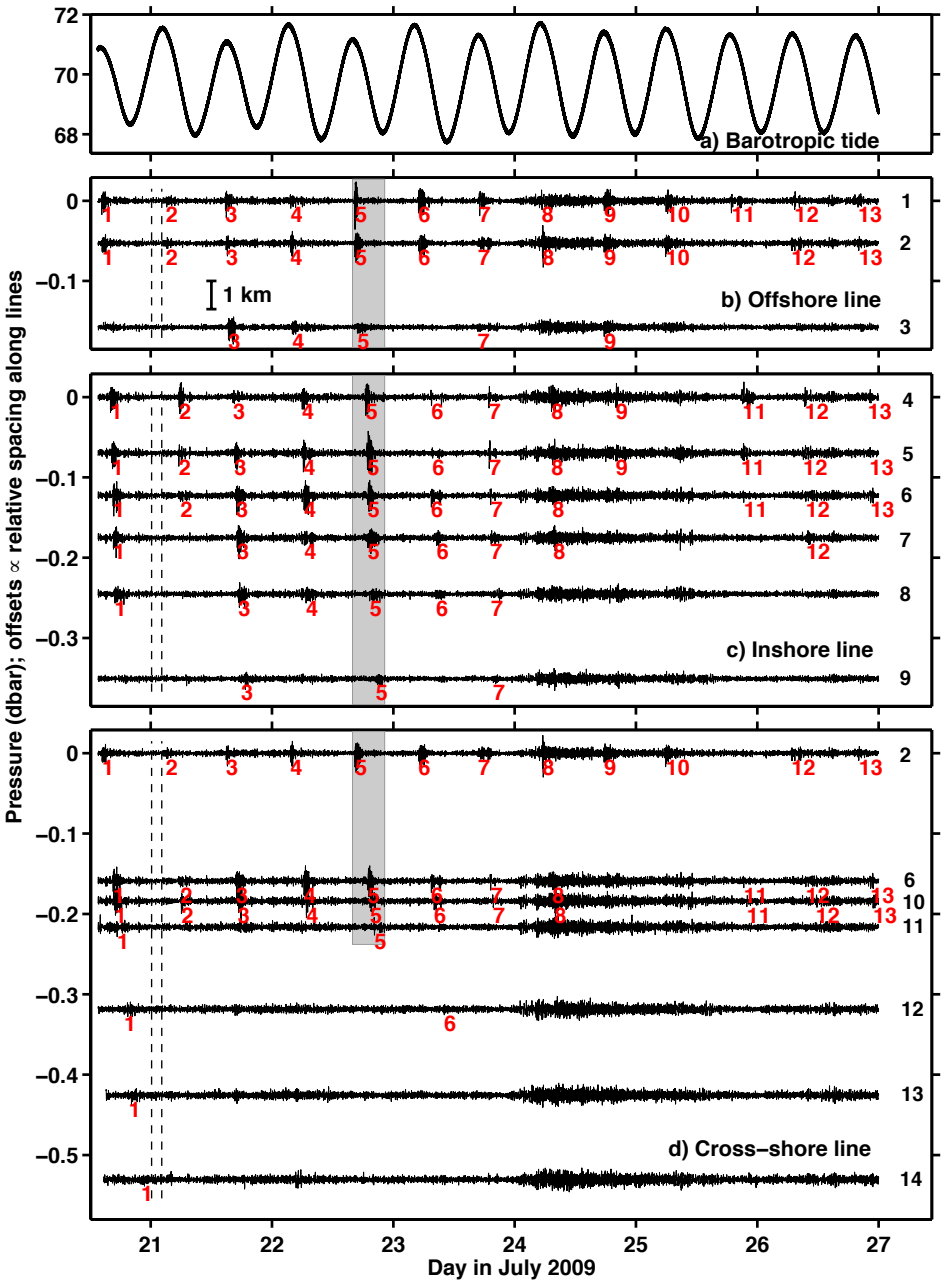

Figure 2.2: Unfiltered bottom pressure from station 1, showing the barotropic tide (a) and 2 to 30 minute band-pass filtered bottom pressure for all 14 stations, separated by line grouping: (b) offshore line; (c) inshore line; (d) cross-shore line. Note that panel (d) repeats stations 2 and 6, which are also part of the offshore and inshore lines, respectively. Offset spacing between zero lines of each station (b-d) is proportional to the distance between stations along each line, as indicated by the 1-km bar in panel (b). Stations are numbered in black on the far right. Red numbers indicate IWP arrivals, if known. The grey patch indicates the data plotted in Fig. 2.3. Vertical black dashed lines indicate the beginning and end of the first 2-hour time period used to calculate var_{BG} (used for IWPs 1 and 2, section 2.3.2.5.2.).

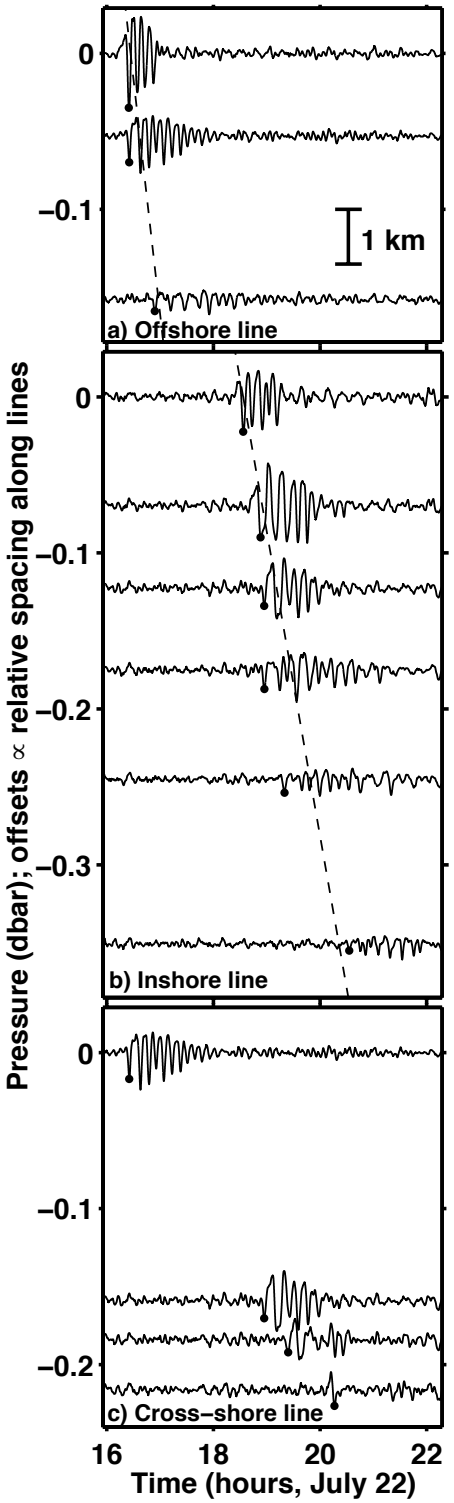

Figure 2.3: Expansion of the grey region in Fig. 2.2, plotted as in Fig. 2.2. Note the cross-shore line here does not include stations 12–14 (c). Black dots indicate IWP 5 arrival times. Dashed lines in panels (a) and (b) represent slope m in equation (2.1).

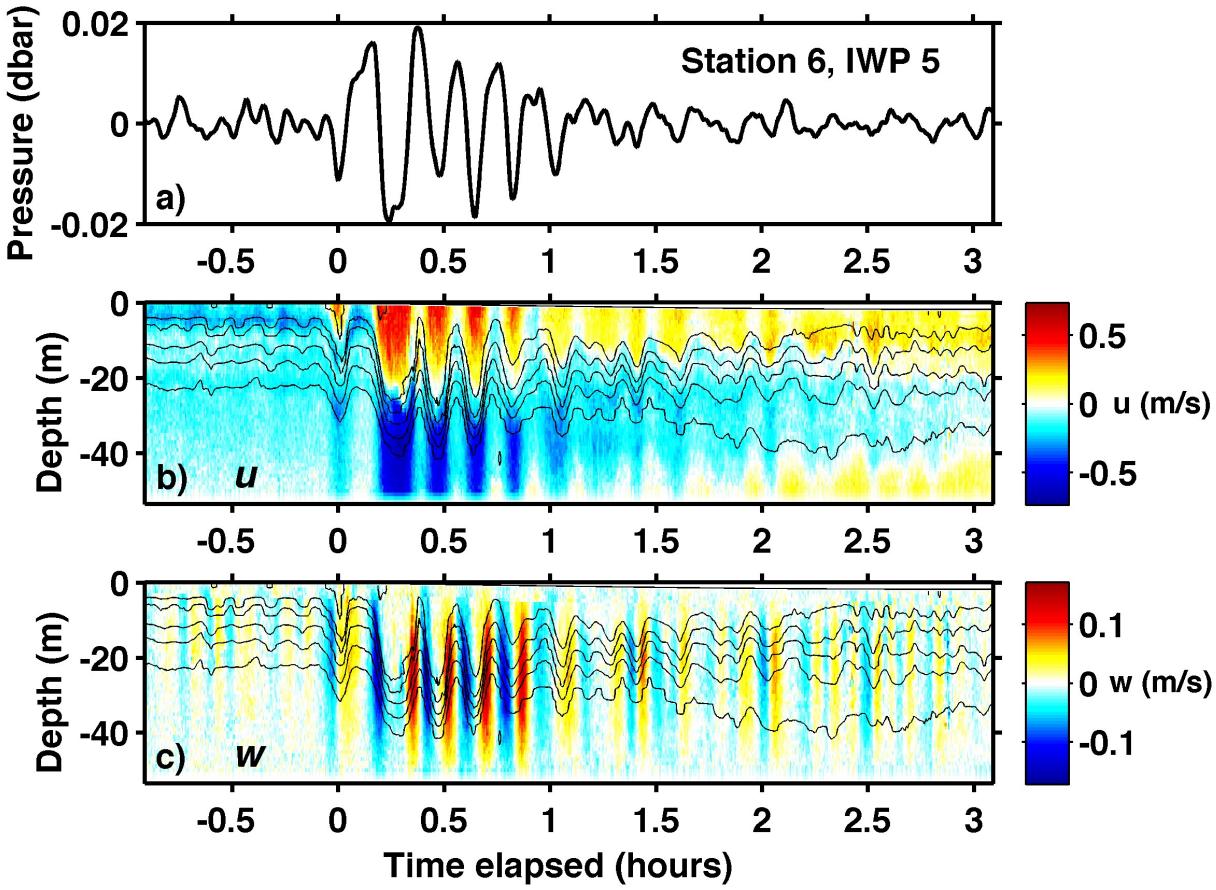

Figure 2.4: Comparison between band-pass filtered bottom pressure data (a); horizontal velocity (color; positive is shoreward, in the same direction as wave propagation; m s^{-1}) and temperature (black contour lines) (b); and vertical velocity (colors; positive is upward; m s^{-1}) and temperature (black contour lines) (c) for IWP 5 at station 6. Time 0 h was chosen to coincide with the arrival of IWP 5 at station 6 to more clearly show how long the wave packet signal persisted at station 6. Isotherms are at 8 to 18 °C at 2 °C intervals. Note that the sea surface can be seen to decrease with the low tide in panels (b) and (c) and that the color scales are not identical for panels (b) and (c).

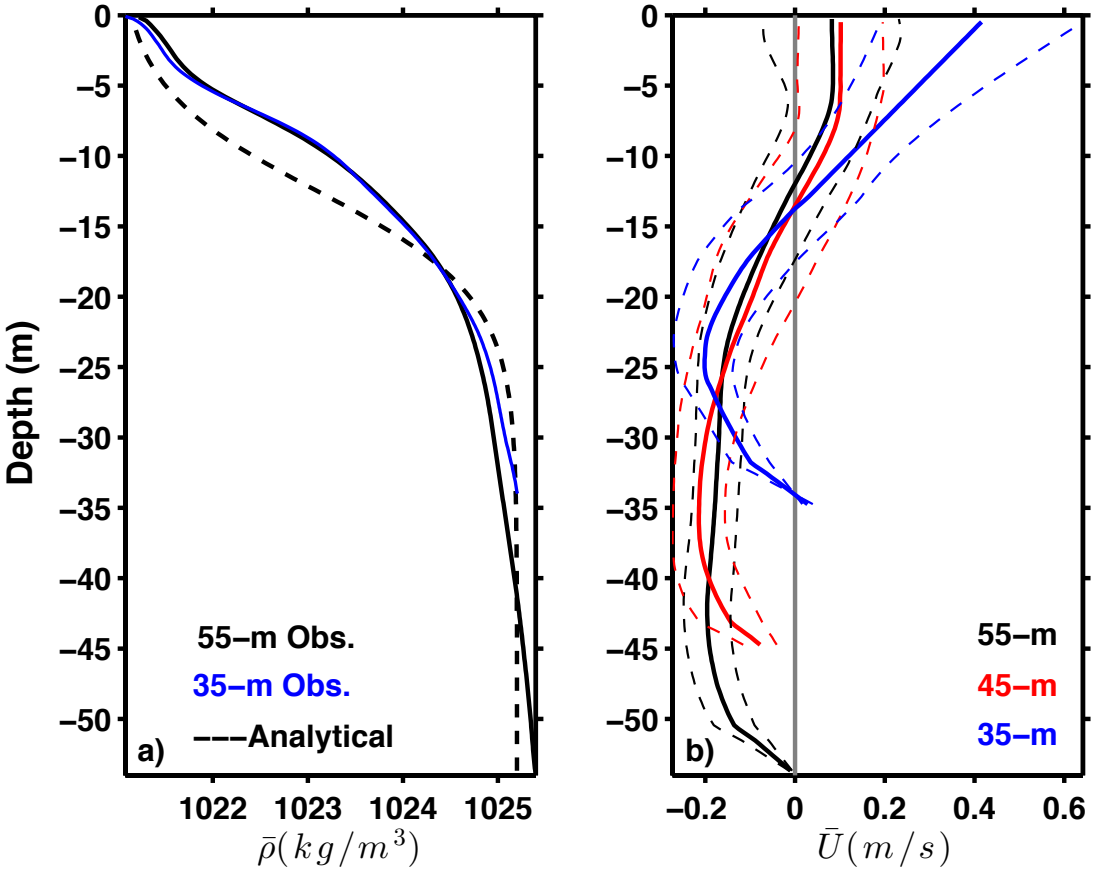

Figure 2.5: a) Average observed background density profiles at stations 6 (55-m) and 11 (35-m) (solid black and blue lines, respectively?note that these lines overlap) and the analytical density profile $\overline{\rho}(z)$ (black dashed line, equation (2.6)). b) Average observed background currents, $\overline{U}(z)$, (solid lines) and standard deviations (dashed lines) for stations 6 (55-m), 10 (45-m), and 11 (35-m).

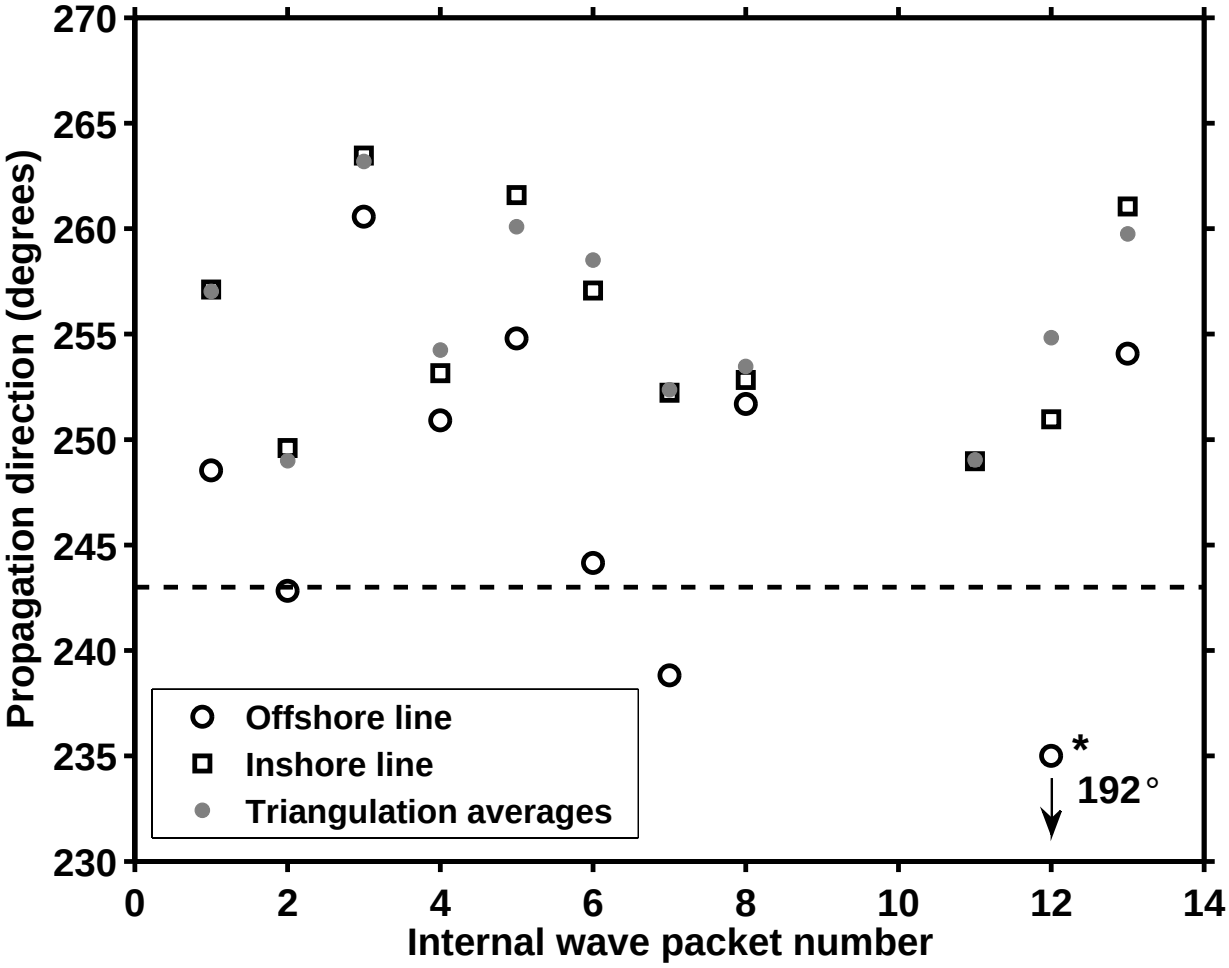

Figure 2.6: Propagation direction estimates for each IWP at the offshore (circles) and inshore (squares) lines, using the plane wave method (equation (2.1)), and averaged triangulation direction (grey dots). Propagation direction is in degrees clockwise from north. The dashed line shows the direction of the cross-shore line and shoreward normal to the alongshore lines (243°). The result for IWP 12 at the offshore line is 192°, which is below the limits of the figure, which were chosen to emphasize wave-to-wave variability.

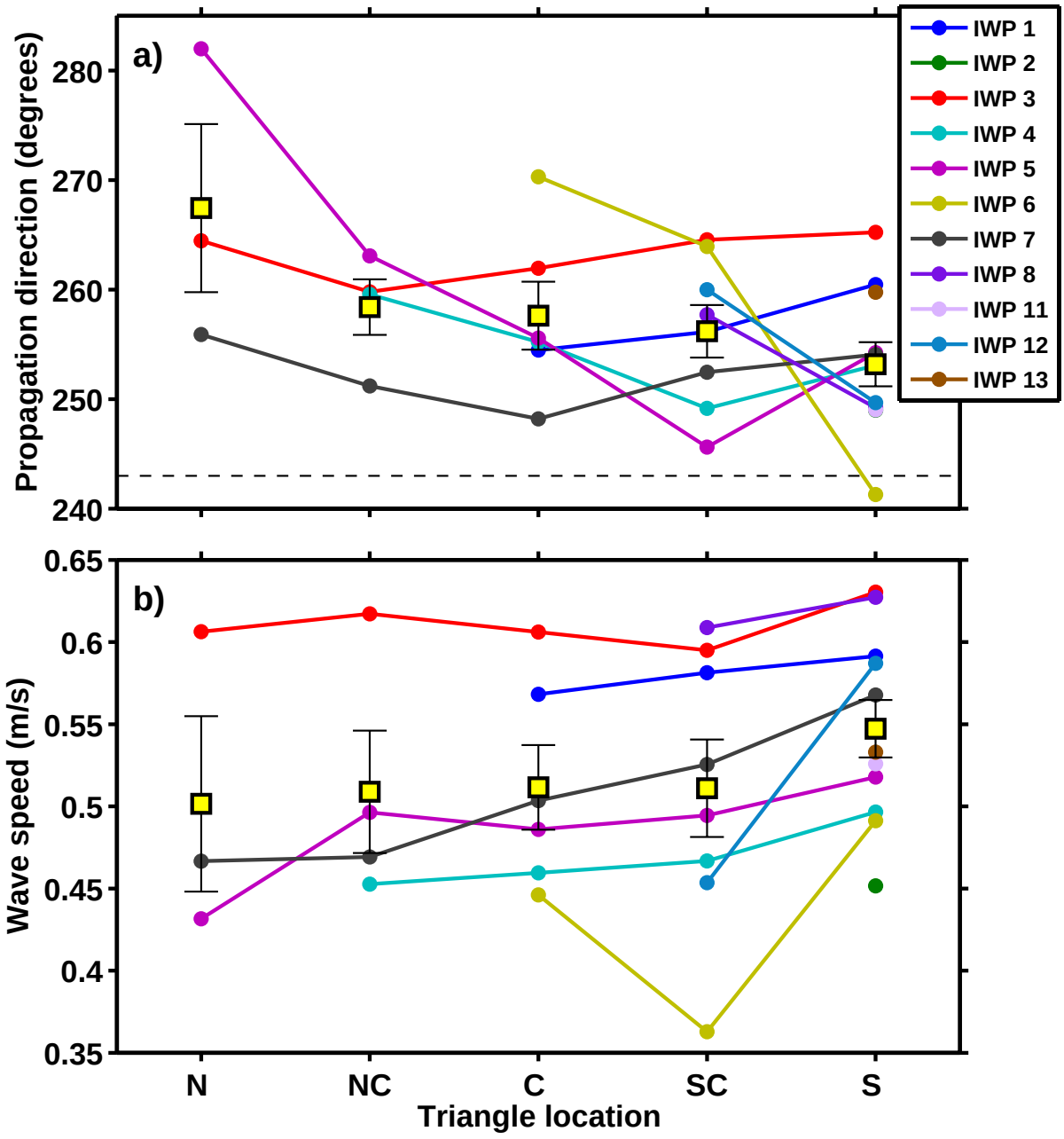

Figure 2.7: Results from the triangulation method (equation (2.2)). (a) Propagation direction estimates for each IWP at each of the five triangles (degrees clockwise from north). There is only one result for IWPs 2, 11, and 13, and the result for IWP 2 is under the points for IWPs 8 and 12 at the southern (S) triangle. The dashed line shows the direction of the cross-shore line, which is the shoreward normal of the alongshore lines (243°). (b) Propagation speed estimates for each IWP at each of the five triangles (m s^{-1}). In both panels, yellow squares with black borders show the mean at each triangle, with bars showing plus/minus the standard error of the mean.

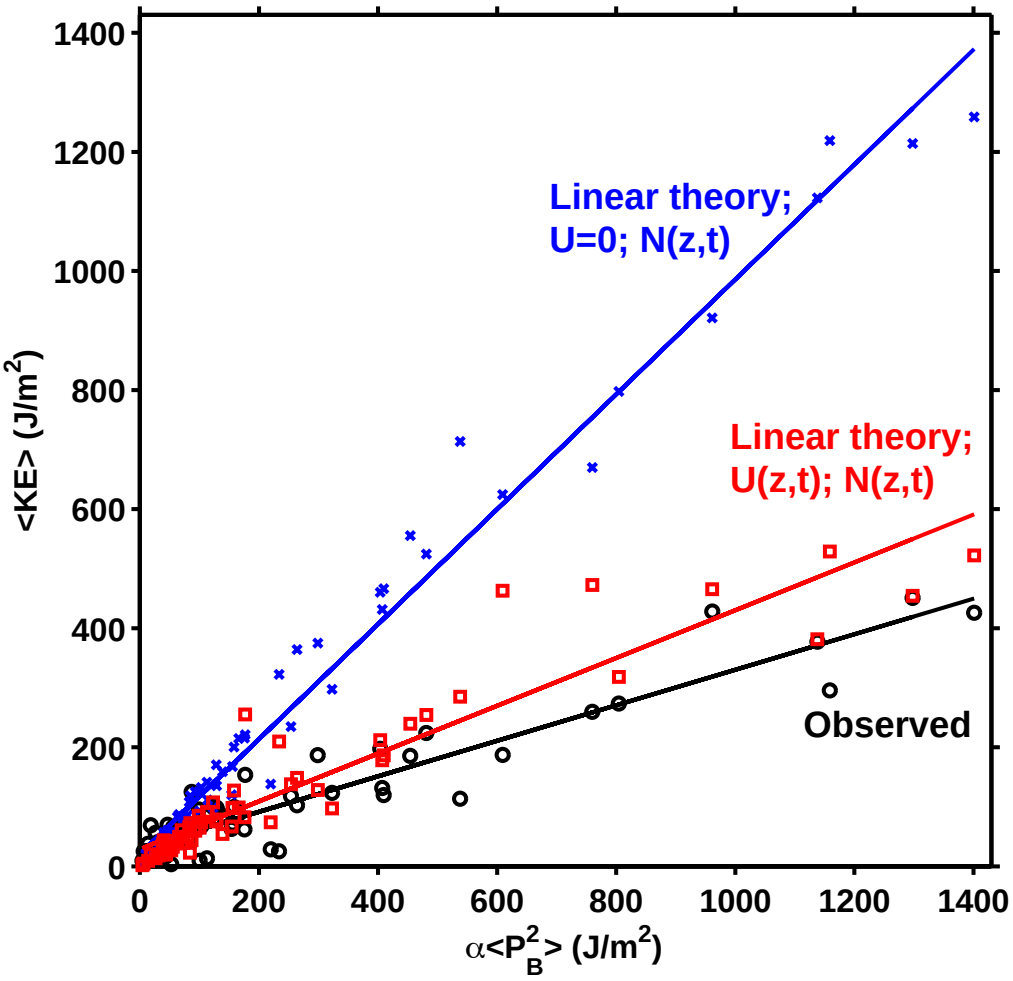

Figure 2.8: Observed and hydrostatic theoretical time-averaged, depth-integrated high-frequency internal wave kinetic energy, $\langle KE \rangle$, versus observed high-frequency internal wave bottom pressure variance, $\langle P_B^2 \rangle_O$, scaled by α (equation (2.8)) at station 6 (55-m depth), over the period from 20 July through 20 August, 2009. Black circles show observations; blue x symbols show predicted $\langle KE \rangle_P$ for each observed $\langle P_B^2 \rangle_O$ when using observed stratification $N(z,t)$ concurrent with the IWPs and setting background currents equal to zero; red squares show predicted $\langle KE \rangle_P$ for each observed $\langle P_B^2 \rangle_O$ when using observed stratification $N(z,t)$ and observed background currents $U(z,t)$ concurrent with the IWPs. Solid lines are the linear fits for each data set. Results were qualitatively the same for stations 10 (45-m water depth) and 11 (35-m depth). Slopes and R^2 values for the three linear fit cases for all three stations are in Table 1.

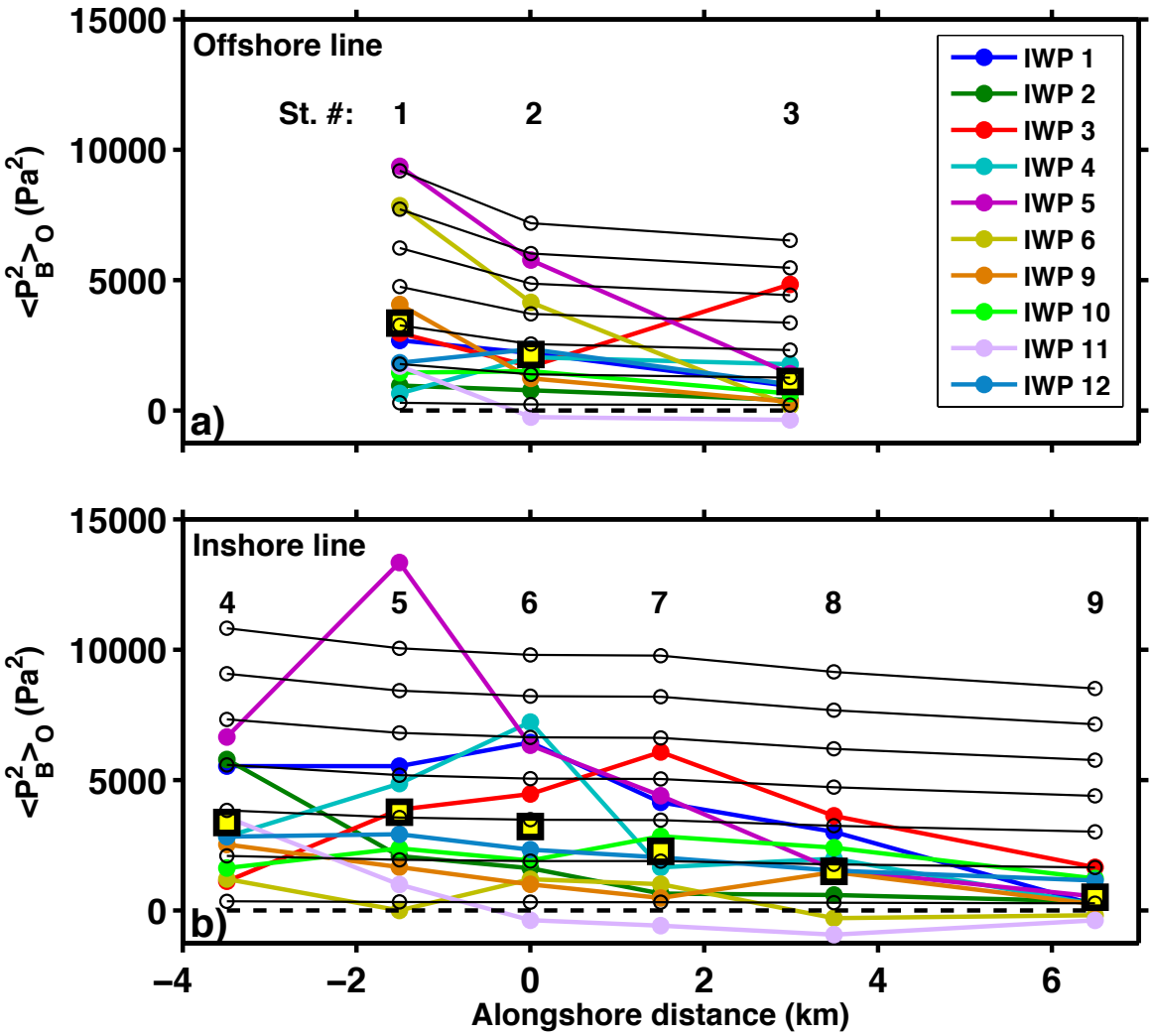

Figure 2.9: Bottom pressure variance $\langle P_B^2 \rangle_O$ along the offshore (a) and inshore (b) lines, with stations 2 and 6 as the origin, respectively, increasing northward. Average $\langle P_B^2 \rangle_O$ for each method at each station is shown by yellow squares with black borders. Solid black lines show predicted changes in bottom pressure variance due only to changes in water depth for IWPs with constant kinetic energy (section 2.4.3.4.). Values of $\langle P_B^2 \rangle_O$ below zero (black dashed line) are due to uncertainties in background variance removal.

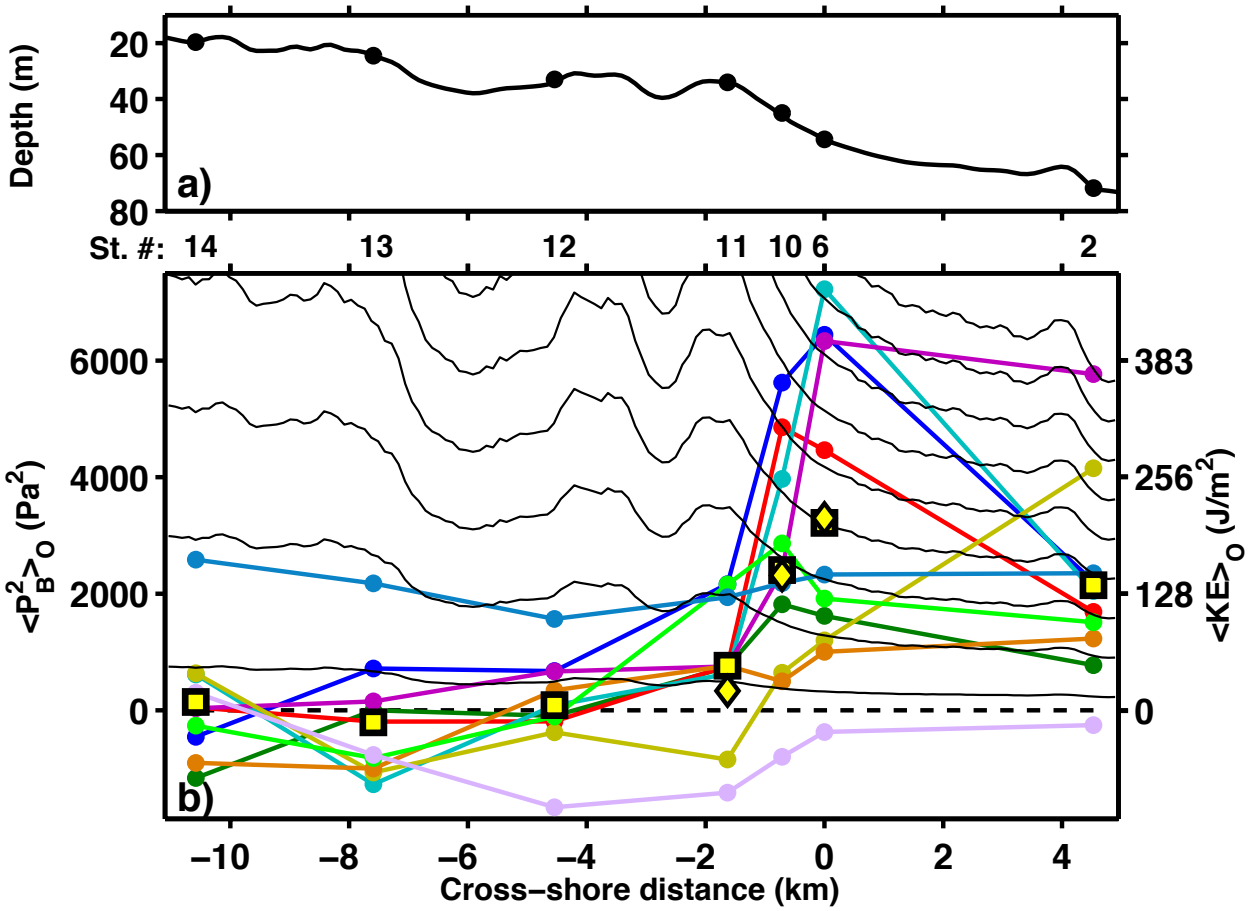

Figure 2.10: Mean water depth (a) and bottom pressure variance $\langle P_B^2 \rangle_O$ (b) along the cross-shore line, with station 6 as the origin, increasing offshore. Average $\langle P_B^2 \rangle_O$ for each method at each station is shown by yellow squares with black borders. Solid black lines in (b) show predicted changes in bottom pressure variance due only to changes in water depth for IWPs with constant kinetic energy (section 2.4.3.4.). Values of $\langle P_B^2 \rangle_O$ below zero (black dashed line) are due to uncertainties in background variance removal (b). Yellow diamonds with black borders (b) are average $\langle KE \rangle_O$ of the IWPs. Note that at stations 6 and 10, the average $\langle KE \rangle_O$ overlap the average $\langle P_B^2 \rangle_O$ results. See Fig. 2.9 for color legend of IWPs.

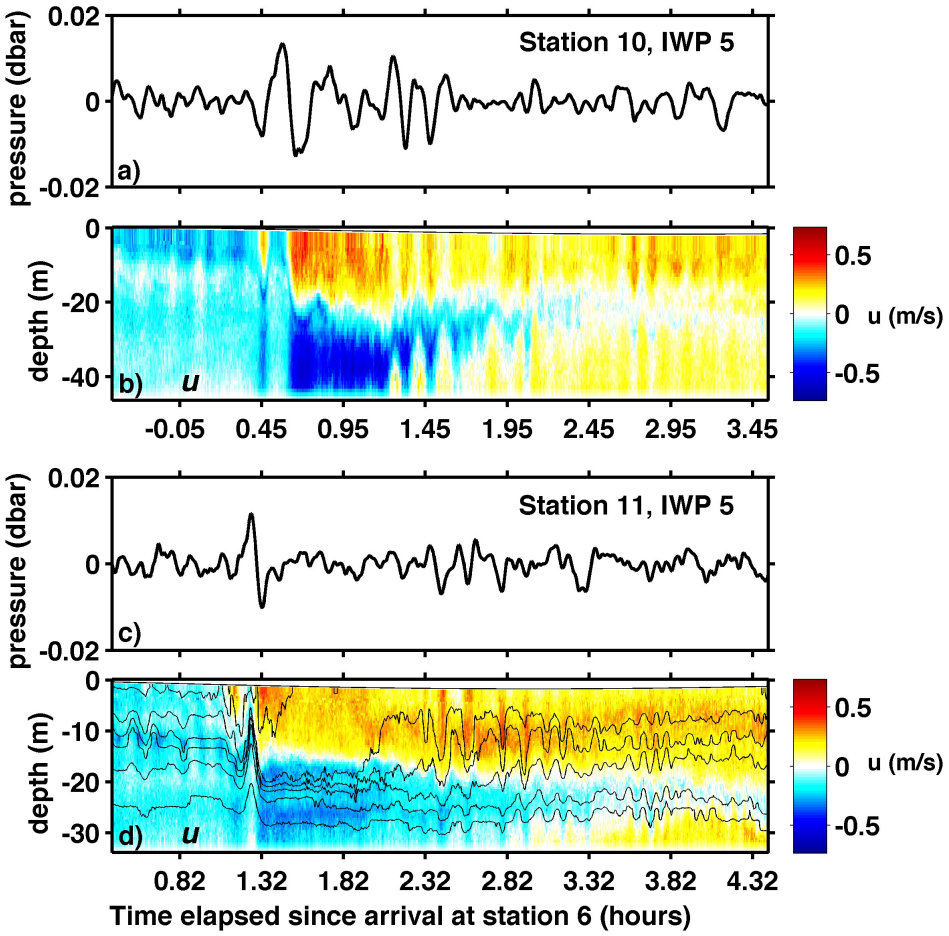

Figure 2.11: Similar to Fig. 2.4, comparison between band-pass filtered bottom pressure and horizontal velocity (color; positive is shoreward, in the same direction as wave propagation; m/s) and temperature (black contour lines) for IWP 5 at stations 10 (panels a and b) and 11 (c and d). Temperature data was not collected at station 10. Time is relative to Fig. 2.4, where time 0 h was chosen to coincide with the arrival of IWP 5 at station 6. IWP 5 arrived at station 10 0.45 hours after arriving at station 6 and arrived at station 11 1.32 hours after arriving at station 6. Isotherms are at 8 to 18 °C at 2 °C intervals. Note that the sea surface can be seen to change with the barotropic tide in panels (b) and (d). Time duration, pressure limits, color scales, and isotherm temperatures are the same as in Fig. 2.4 panels a and b.

Chapter 3: Coupled barotropic-baroclinic resonant modes in idealized basins with alongshore uniform shelves and their application to barotropic and baroclinic tides

Jennifer Thomas, James Lerczak, Clinton Winant, and Roger Samelson

To be submitted to Journal of Physical Oceanography

45 Beacon Street

Boston, MA 02108-3693

USA

3.1 Abstract

This study explores the importance of superinertial resonant mode excitation for barotropic and baroclinic tides and whether modes can yield coastal-trapped superinertial internal tides. Coupled barotropic-baroclinic basins with alongshore uniform shelves are used to investigate effects of basin size, continental shelves, shelf-deep phase speed ratio, and rotation on resonant modes. Basin modes, shelf-amplified basin modes, and edge modes are excited by an idealized equilibrium tide. In basins with continental shelves, modes can be coupled with both barotropic and baroclinic wave scales. Once the shelf is wider than a quarter-wavelength of a mode, mode frequencies shift to lower values. The ratio of phase speeds between the shelf and deep basin is important in determining the impact of shelves on modes. The smaller the ratio, the less far edge modes extend into the deep basin. Rotation causes phase propagation of modes that can be clockwise and/or counterclockwise and can result in complicated structures. Basin mode excitation requires waves to propagate fully across the basin. Thus, basin modes for barotropic tides could occur in large basins, due to their relatively fast phase speeds, but slower-propagating baroclinic tides would only be able to develop basin modes in smaller basins. We speculate that edge modes depend only on shelf geometry, and not deep basin geometry, such that baroclinic edge modes should be able to develop more quickly, making them possible for any continental shelf with appropriately tuned geometry. Baroclinic edge modes can have phase that propagates alongshore or that appears like standing waves, resulting in different types of large-amplitude shelf-trapped superinertial internal tides.

3.2 Introduction

Current variability is dominated by temporally intermittent internal tides on many continental shelves (e.g. Lerczak et al. 2003; Alford et al. 2006; Savidge et al. 2007; Aguirre et al. 2010; Nash et al. 2012a,b; Aristizábal et al. 2016). Observations show structures consistent with coastal-trapped alongshore propagating superinertial internal tides, with coherent alongshore variability (e.g. Lerczak et al. 2003; Alford et al. 2006; Klymak et al. 2016). However, most studies on internal waves have focused primarily on cross-shore structure and propagation, often neglecting alongshore variability. So, while alongshore propagating superinertial internal tides are known to exist in the ocean, their dynamics are not well understood. Work by Dale and Sherwin (1996) and Dale et al. (2001), extending subinertial baroclinic coastal-trapped wave theory to superinertial frequencies, suggests that alongshore propagating superinertial internal tides could be resonantly excited by alongshore bathymetric variability of appropriate length scales on continental shelves, which could be important considering that the often dominant $M2$ tidal frequency is superinertial from the equator to $\sim 74.5^{\circ}$ latitude. Previous studies have suggested that some observations of barotropic and baroclinic tides can be described as the resonant (or, near resonant) excitation of a basin's normal modes (Platzman et al. 1981; Platzman 1984b; de Young and Pond 1987; Allen and Simpson 2002; Winant 2010; Buijsman et al. 2012). These studies motivate us to explore resonant barotropic and baroclinic tide basin and edge mode excitation on continental shelves and their sensitivity to basin and shelf geometry and stratification, in order to understand how resonant basin mode and edge mode exci-

tation might be important for barotropic and baroclinic tides and if they might help us understand alongshore propagating superinertial internal tides and observations of internal tide temporal intermittency.

In this paper, we study the excitation of superinertial resonant modes in basins to test our hypotheses that direct forcing of baroclinic modes by the tide generating potential can generate large-amplitude, coastal trapped, superinertial internal tides, and that the tuning/detuning of resonant modes might explain some observations of temporal intermittency in internal tides. In addressing these questions, we develop a linear model to explore coupled barotropic-baroclinic resonant basin and edge modes, which addresses our hypotheses, including how basin size, continental shelf width, the phase speed ratio between the shelf and deep basin, and rotation affect resonant basin and edge modes and how these might be important for barotropic and baroclinic tides. Our specific objectives are to:

1. develop theoretical predictions for the types of modes–basin modes, shelf-amplified basin modes, and edge modes–that exist in idealized basins;
2. describe how modes are affected by basin size, continental shelf width, the phase speed ratio between the shelf and deep basin, and rotation on an f-plane;
3. explore how likely it is that a mode will be resonantly excited in a real ocean basin;
4. and show that basin and edge mode excitation by the tide generating potential can generate large-amplitude superinertial internal tides on the shelf with phase that propagates alongshore or that is perhaps standing.

Huthnance (1975) uses shallow water theory to describe the distribution of barotropic

coastal-trapped modes for a straight shelf with a monotonic depth profile and uniform density (Kelvin waves, edge waves (superinertial modes), and continental-shelf waves (subinertial, topographic Rossby wave modes)) for arbitrary continental shelf profiles, and there is observational evidence of these barotropic modes along continental shelves. While in a homogeneous basin, the superinertial edge modes are perfectly trapped, in a continuously stratified ocean, edge waves are not perfectly trapped, because even though the surface wave decays exponentially into the deep basin, they slowly lose energy to scattering into internal modes that radiate into the deep sea (Huthnance 1978). In a basin with two-layered stratification and a rigid lid, perfectly trapped superinertial baroclinic edge modes can exist, but with continuous stratification, like the barotropic edge modes, baroclinic edge modes scatter energy into the deep sea, becoming partially trapped. Chapman (1982) showed that along a step-shelf that borders a constant-depth, non-rotating ocean, refractively nearly trapped internal edge waves can occur when the shelf width is approximately one-quarter "...plus any integral number of half wavelengths..." the cross-shelf wavelength, and that these would be modified only slightly in a rotating basin, in which they would be nearly trapped superinertial internal edge waves, equivalent to the barotropic superinertial edge modes in Huthnance (1975). Dale and Sherwin (1996) and Dale et al. (2001) continue dispersion curves from sub- to superinertial and show that there is a smooth transition from trapped subinertial to partially-trapped superinertial waves, which lose energy to scattering offshore, though it is not known to what extent they lose energy.

In a series of papers, Platzman describes a finite element barotropic model for

solving for barotropic normal modes of the world oceans and from them, synthesizes diurnal and semidiurnal tides by summing over modes (Platzman 1978; Platzman et al. 1981; Platzman 1984a,b). In this work, he shows that some observed tides are consistent with individual modes. For example, the California amphidrome that yields the barotropic tide that propagates northward along the west coast of North America closely resembles the 15.5 hour basin mode he refers to as the Pacific North American Kelvin wave (Platzman 1979).

Winant (2010) showed that the excitation of basin modes can also be important in explaining large amplitude internal tides observed in some small basins. His idealized, two-layered, free surface model of the Strait of Juan de Fuca-Strait of Georgia system, forced at the opening to the Pacific Ocean by the $M2$ tide, resulted in resonant excitation of a cross-channel internal seiche mode response that is similar to observations by Martin et al. (2005). The model showed that as stratification changes, the small basin is tuned toward or detuned away from large amplitude responses. Winant's modeling work also supported observations in Upper Loch Linnhe fjord (Allen and Simpson 2002) of normal mode excitation of a standing internal tide within the fjord. Winant (2010) suggests that the extension of his model to an open continental shelf in a large ocean basin might result in baroclinic Kelvin wave systems that are trapped to the coast.

Our work extends the coupled barotropic-baroclinic model of Winant (2010) to enclosed idealized basins of any size with continental shelves, addressing the coupled barotropic-baroclinic resonant modes for superinertial tides. Our basins thus include what we call "basin modes" and "shelf-amplified basin modes" that impact

the sea surface and interface structure throughout the full basin–like the full-basin and Kelvin barotropic modes addressed in the series of Platzman papers (Platzman 1978, 1979; Platzman et al. 1981; Platzman 1984a,b) and the full-basin baroclinic modes in Winant (2010)–and "edge modes" that impact the structure primarily over the shelves–like the superinertial barotropic edge waves of Huthnance (1975) and superinertial baroclinic partially-trapped waves of Chapman (1982), Dale and Sherwin (1996), and Dale et al. (2001). We will show that the basin modes, shelf-amplified basin modes, and edge modes are resonant modes in our idealized basins, in which the two basin mode types depend on the full basin geometry whereas the edge modes depend only on the shelf geometry. We will discuss the implications of the amount of time required for resonant modes to set up, showing that resonant edge mode excitation of baroclinic modes could result in large-amplitude internal tides on shelves of the appropriate geometry in basins of any size.

Alongshore propagating, trapped superinertial internal tides have been observed at many coastlines, such as in Lerczak et al. (2003) on the continental margin off Mission Bay, CA, in Alford et al. (2006) in Mamala Bay, south of Oahu, HI, and in Klymak et al. (2016), on the Tasman continental slope. Most of the observations by Lerczak et al. (2003) had intermittency that did not modulate with the spring/neap cycle. Observations by Alford et al. (2006) of the interference pattern of interacting eastward and westward (both alongshore) propagating internal tides included variability on time scales of months, attributed to changes in stratification and propagation times from remote generation sites. Perhaps intermittency seen in observations like these can be partly explained by stratification tuning toward and away from mode

resonance.

The sections in this paper are organized as follows: In section 3.3, we derive a pair of coupled equations used to solve for sea surface and interface displacement in enclosed basins and we describe our method for solving for modes. In section 3.4, the modes are solved in one-dimensional basins with no rotation, with theory developed to predict resonant frequencies in flat basins and basins with continental shelves. The resulting mode structures for basin modes and shelf-amplified basin modes are described, along with the effects of shelf width and phase speed ratio over the shelf and deep basin on mode structures and frequencies. We discuss the factors that influence how easy it is to "tune into" and excite different modes. In section 3.5, the problem is solved in two-dimensional basins with no rotation. Edge wave modes (modes that are nearly trapped to the shelves) are introduced and theory developed to predict their occurrence. Modes are described in flat basins and basins with continental shelves, again discussing factors that influence how easy it is to excite the modes. In section 3.6, rotation is added to the two-dimensional problem. Modes in these basins are described as analogs to those in the non-rotating case, relying on the theory without rotation. Here, we see resonant excitation of large-amplitude superinertial internal tides on the shelf. We discuss the influence of rotation on how easy it is to excite modes. Finally, in section 3.7, we summarize the findings, discussing the implications of basin and edge mode excitation on real ocean basins and discussing some questions that remain on their applicability to generating large-amplitude barotropic and baroclinic tides.

3.3 Coupled barotropic-baroclinic equations

Similar to the coupled problem in Winant (2010), we begin by deriving two second-order partial differential equations to solve for displacement of the free sea surface and internal interface in a three-dimensional enclosed basin rotating on an f-plane, with two-layered stratification and variable bathymetry that do not intersect. There is a periodic body force acting on the basin, modeled as an idealized equilibrium tide propagating from east to west with amplitude A^*, frequency σ^*, and horizontal wavenumbers k^* and l^*, which can be written as

$$\overline{\eta(x,y,t)}^* = \mathrm{Re}[A^* cos(l^* y^*) e^{i(k^* x^* + \sigma^* t^*)}]\,. \tag{3.1}$$

The symbol * denotes dimensional parameters throughout.

The forced, linear, inviscid, Boussinesq, shallow water equations for a barotropic-baroclinic coupled two-layered system are non-dimensionalized using the forcing frequency and the length and depth scales of the basin, as follows:

$$\frac{\partial u_1}{\partial t} - f v_1 = -\frac{1}{\sigma^2}\frac{\partial(\eta - \overline{\eta})}{\partial x}\,, \tag{3.2}$$

$$\frac{\partial v_1}{\partial t} + f u_1 = -\frac{1}{\sigma^2}\frac{\partial(\eta - \overline{\eta})}{\partial y}\,, \tag{3.3}$$

$$\frac{\partial \eta}{\partial t} + h_1\left(\frac{\partial u_1}{\partial x} + \frac{\partial v_1}{\partial y}\right) - \frac{\partial \zeta}{\partial t} = 0\,, \tag{3.4}$$

$$\frac{\partial u_2}{\partial t} - f v_2 = -\frac{1}{\sigma^2}\frac{\partial(\eta - \overline{\eta})}{\partial x} - \frac{\rho}{\sigma^2}\frac{\partial \zeta}{\partial x}\,, \tag{3.5}$$

$$\frac{\partial v_2}{\partial t} + f u_2 = -\frac{1}{\sigma^2}\frac{\partial(\eta - \overline{\eta})}{\partial y} - \frac{\rho}{\sigma^2}\frac{\partial \zeta}{\partial y}\,, \tag{3.6}$$

$$\frac{\partial \zeta}{\partial t} + (h(x,y) - h_1)\left(\frac{\partial u_2}{\partial x} + \frac{\partial v_2}{\partial y}\right) + u_2\frac{\partial h}{\partial x} + v_2\frac{\partial h}{\partial y} = 0\,. \tag{3.7}$$

The non-dimensional parameters are

$$\begin{aligned}
&t = \sigma^* t^*;\ x = \frac{x^*}{L_x^*};\ y = \frac{y^*}{L_x^*};\ z = \frac{z^*}{H^*};\\
&h(x,y) = \frac{h(x,y)^*}{H^*};\ h_1 = \frac{h_1^*}{H^*};\ \text{and}\ H = \frac{H^*}{H^*} = 1;\\
&u_{1,2}(x,y,t) = \frac{u_{1,2}(x,y,t)^*}{\sigma^* L_x^*};\ v_{1,2}(x,y,t) = \frac{v_{1,2}(x,y,t)^*}{\sigma^* L_x^*};\ w_{1,2}(x,y,t) = \frac{w_{1,2}(x,y,t)^*}{\sigma^* H^*};\\
&\eta(x,y,t), \zeta(x,y,t) = \frac{\eta(x,y,t)^*, \zeta(x,y,t)^*}{H^*};\ \overline{\eta(x,y,t)} = \frac{\overline{\eta(x,y,t)}^*}{H^*};\ k = k^* L_x^*;\ l = l^* L_x^*;\\
&\sigma = \frac{\sigma^* L_x^*}{\sqrt{g^* H^*}};\ f = \frac{f^*}{\sigma^*};\ \text{and}\ \rho = \frac{\Delta\rho^*}{\rho_o^*};
\end{aligned} \tag{3.8}$$

where σ^* is the forcing frequency; L_x^* is the basin length in the x direction; H^* is the maximum deep basin depth; $h(x,y)^*$ is the bathymetry as a function of x^* and y^*; h_1^* is the resting upper layer thickness; subscripts 1 and 2 denote which layer is described by the variable; η^* is displacement of the sea surface; ζ^* is displacement of the interface between layers 1 and 2; and k^* and l^* are the x- and y-direction wavenumbers of the forcing, respectively. The non-dimensional parameter σ, which will frequently be referred to throughout the paper, shows how the basin length in the x-direction relates to the wavelength of the free non-rotating shallow water wave with the forcing frequency; f shows how the Coriolis parameter relates to the forcing frequency; and ρ is the stratification strength as the ratio of the density difference

between the two layers of fluid to their average density.

Separable, periodic solutions are sought, of the form

$$\eta(x,y,t) = \mathrm{Re}\left(N(x,y)e^{it}\right);\ \zeta(x,y,t) = \mathrm{Re}\left(Z(x,y)e^{it}\right);\ \overline{\eta}(x,y,t) = \mathrm{Re}\left(\overline{N}(x,y)e^{it}\right);$$
$$u_{1,2}(x,y,t) = \mathrm{Re}\left(U_{1,2}(x,y)e^{it}\right);\ v_{1,2}(x,y,t) = \mathrm{Re}\left(V_{1,2}(x,y)e^{it}\right); \tag{3.9}$$

where $N, Z, \overline{N}, U_{1,2}$, and $V_{1,2}$ are complex amplitudes and phases.

We define $N' = N - \overline{N}$, the deviation of sea level from the equilibrium tide forcing, substitute it and the solution form (equations 3.9) into the forced coupled shallow water equations (3.2-3.7), and combine the equations to form the two coupled second-order partial differential equations that solve for displacement of the sea surface, N', and internal interface, Z:

$$\frac{h_1}{\sigma^2(1-f^2)}\left(\frac{\partial^2}{\partial x^2}+\frac{\partial^2}{\partial y^2}\right)N' + N' - Z = -\overline{N}\,, \text{ and} \tag{3.10}$$

$$\frac{1}{\sigma^2(1-f^2)}\left[(h(x,y)-h_1)\left(i\frac{\partial^2}{\partial x^2}+i\frac{\partial^2}{\partial y^2}\right)+\frac{\partial h}{\partial x}\left(i\frac{\partial}{\partial x}+f\frac{\partial}{\partial y}\right)\right.$$
$$\left.+\frac{\partial h}{\partial y}\left(-f\frac{\partial}{\partial x}+i\frac{\partial}{\partial y}\right)\right](N'+\rho Z)+iZ = 0\,, \tag{3.11}$$

where

$$\overline{N}(x,y) = \frac{A^*}{H^*}cos(ly)e^{ikx}\,. \tag{3.12}$$

At the solid basin boundaries ($x^* = 0, L_x^*$; $y^* = 0, L_y^*$; or $x = 0, 1$; $y = 0, \frac{L_y^*}{L_x^*}$),

normal transport must vanish, resulting in four boundary conditions:

$$f\frac{\partial N'}{\partial y} + i\frac{\partial N'}{\partial x} = 0\Big|_{x=0,1}, \tag{3.13}$$

$$-f\frac{\partial N'}{\partial x} + i\frac{\partial N'}{\partial y} = 0\Big|_{y=0,\frac{L_y^*}{L_x^*}}, \tag{3.14}$$

$$f\frac{\partial Z}{\partial y} + i\frac{\partial Z}{\partial x} = 0\Big|_{x=0,1}, \tag{3.15}$$

$$-f\frac{\partial Z}{\partial x} + i\frac{\partial Z}{\partial y} = 0\Big|_{y=0,\frac{L_y^*}{L_x^*}}. \tag{3.16}$$

The equations are solved for a range of the parameter σ for different basin structures via the computational method of Lindzen and Kuo (1969). We identify basin modes as occurring at values of σ for which there is an unbounded peak in interface response amplitude. For efficiency, we begin our sweeps through σ with $\Delta\sigma = 0.001$, then identify peaks in response, and further converge on those peaks by iterating through finer resolution sweeps through σ about each peak. With each iteration, peak amplitudes increase and structures of the responses further converge to the structures of resonant modes. The result is a series of peaks of varying large amplitudes in response, but the relative amplitudes of the peaks are not significant, as further convergence would continue to increase the unbounded peaks.

Note that the structure in which the equations were discretized results in solutions that do not conserve volume for even modes (modes with an even number of zero crossings), but a reformatting of the discretization gives solutions that are identical

but do conserve volume. Thus, none of the conclusions change. The non-volume conserving solutions have mean sea surface and interface displacements that are offset from zero, so figures are presented with the mean removed. See thesis appendix A for a further explanation.

Changes in σ can represent a change in forcing frequency, basin length, or basin depth (equations 3.8). When rotation is included, we keep the non-dimensional Coriolis parameter constant and superinertial, at $f = 0.73$. This value for f comes from solving for f^* at 45° N and σ^* at the $M2$ frequency; so when looking at the results when rotation is included, if we consider a change in σ to be due to changing σ^*, then f^* also changes such that f remains constant.

Our reason for solving for modes as a coupled system with both barotropic and baroclinic motions, instead of solving separately for them using a homogeneous basin and the rigid lid approximation, is because when we have a free surface in the two-layered coupled system, we see that the coupling affects mode structures, with barotropic and baroclinic wave scales superimposed on each other for some resonant responses that would otherwise be considered strictly barotropic or baroclinic in the separate, non-coupled systems. Additionally, when using the forcing to find the modes of these basins, in the rigid lid derivation of equations that solve for interface motions, the forcing cancels out. Thus, the coupled system shows that the equilibrium tide forcing can excite both barotropic and baroclinic resonant modes.

3.4 One-dimensional problem, no rotation

Considering the coupled problem in an enclosed basin with only x and z dimensions and no rotation simplifies the responses such that some of the effects of continental shelves on basin modes can be clearly demonstrated. In the analyses of these simple basins that follow, it will be shown that in this coupled barotropic-baroclinic system, in basins with shelves, modes are not always clearly barotropic or baroclinic, but can contain both longer barotropic and shorter baroclinic wavelength scales, superimposed. We will see that shelves impact the frequency of a mode when the shelf width is greater than a quarter wavelength of a mode. At that point, modes shift to lower frequencies as the wavelength scales compress over the shelves and widen in the deep basin. The influence of shelves on basin modes also depends on the phase speed ratio between the shelf and the deep basin.

The enclosed non-dimensional basins analyzed here have identical, two-layered stratification ($h_1 = 0.02625$) (Fig. 3.1). One basin has flat bathymetry, one has narrow continental shelves ($L_{shelf} = 0.0321$), and the other has wide continental shelves ($L_{shelf} = 0.132$). The two basins with shelves have identical shelf depths ($h_s = 0.05$) and slopes, with only the shelf width varying. For the narrow shelves basin, basin mode wavelengths (the wavelength of the free wave over the shelf) will not be comparable to the shelf width until high frequencies, whereas for the wide shelves basin, that will occur at lower frequencies.

3.4.1 Flat basin

Beginning with flat bathymetry allows us to develop an initial intuition about basin modes of the coupled system as well as analytical theory to serve as a foundation for more complicated basins.

3.4.1.1 Analytical solution for resonant frequencies

With flat bathymetry, the coupled system can be solved analytically for values of σ at which resonant modes will occur, yielding

$$\sigma_j = j\pi\sqrt{\frac{1}{2}\left[(1+\rho(1-h_1)) \pm \sqrt{(1+\rho(1-h_1))^2 - 4\rho h_1(1-h_1)}\right]}, (j = 1, 2, 3, ...), \tag{3.17}$$

where unambiguously the plus sign gives barotropic modes and the minus sign gives baroclinic modes. To leading order, for $\rho << 1$, this equation for σ_j in a basin of depth $H = 1$ reduces to that for barotropic modes in a homogeneous basin when using the plus sign ($\sigma_j \sim j\pi$), and it reduces to that for baroclinic modes in a rigid lid basin when using the minus sign ($\sigma_j \sim j\pi\sqrt{\rho h_1(1-h_1)}$), which can be shown by expanding the equation for σ_j in ρ and looking at the leading order behavior in the

limit of $\rho << 1$, as follows:

$$\sigma_j = j\pi\sqrt{\frac{1}{2}\left[(1+\rho(1-h_1)) \pm \sqrt{1+\rho(2-2h_1-4h_1+4h_1^2)+O(\rho^2)}\right]},$$

$$\text{Taylor expansion}: \ \sigma_j \approx j\pi\sqrt{\frac{1}{2}\left[(1+\rho(1-h_1)) \pm (1+\rho(1-h_1-2h_1+2h_1^2)+O(\rho^2))\right]},$$

$$\sigma_{j+} \approx j\pi\sqrt{1+\rho(1-h_1)^2+O(\rho^2)} = j\pi\sqrt{1+O(\rho)+O(\rho^2)},$$

$$\sigma_{j-} \approx j\pi\sqrt{\rho h_1(1-h_1)-O(\rho^2)}. \tag{3.18}$$

As we solve equations (3.10 and 3.11) while sweeping through changing values of σ for a particular basin, we calculate the average variance of the interface motions for each value of sigma, in order to determine frequencies of resonant basin mode responses (Fig. 3.2a, black line). This is plotted over the results for σ_j (equation 3.17) (Fig. 3.2a, blue (barotropic) and green (baroclinic) vertical dashed lines), showing that for each resonant mode predicted by σ_j, the flat basin has a peak in response variance of the interface. Thus, each peak in the response corresponds to a resonant mode of the basin, such that for that combination of basin length L_x^* and depth H^*, there is a normal mode with frequency σ^*. Note that even without bathymetric variability within the enclosed basin, in addition to large-amplitude resonant barotropic modes that one would expect, resonant mode excitation yields large-amplitude baroclinic modes in the coupled stratified basin.

3.4.1.2 Mode structures

The structures of each of the modes are what would be expected according to the basin mode predicted by σ_j. They are standing cosine waves, and the mode number is equal to the number of zero crossings, or nodes, across the basin. For example, the first barotropic mode (σ_j for $j = 1$, using the plus sign in equation 3.17) (Fig. 3.2a, first peak with a blue circle) has one zero crossing in the sea surface and interface structure, 0° phase between the sea surface and interface, and a larger amplitude in sea surface motions than in interface motions (Fig. 3.3a). The first baroclinic mode (σ_j for $j = 1$, using the minus sign in equation 3.17) (Fig. 3.2a, first peak with a green circle) also has one zero crossing in the sea surface and interface structure, but now there is a 180° phase difference between the sea surface and interface, and the interface has the larger amplitude (Fig. 3.3b).

For barotropic modes, interface motions scale as approximately $\frac{h_2}{H}\eta_{BT}$. In this basin, the lower layer (h_2) is nearly as thick as the full basin depth, H, causing the barotropic interface amplitudes to be nearly as large as those of the sea surface: $\zeta_{BT} \sim 0.97\eta_{BT}$. For baroclinic modes, sea surface motions scale as approximately $\frac{-\rho h_2}{H}\zeta_{BC}$. In this basin, and all of the basins presented in this paper, we have used a large, unphysical value for ρ (0.25) to make the problem easier to solve and interpret, meaning $\eta_{BC} \sim -0.24\zeta_{BC}$. A larger value of ρ means less baroclinic modes and larger wavelengths for a given range of σ. So, it is easier to manage identifying all of the modes within a range of σ, and our horizontal grid resolution does not have to be very fine. This large value of ρ means that the sea surface amplitudes of baroclinic

modes are un-physically large relative to interface amplitudes, but note that none of our conclusions change when a smaller, more realistic value of ρ is used.

3.4.2 Basin with narrow continental shelves

With narrow continental shelves added to the basin, we can start to look at how shelves affect basin modes.

3.4.2.1 Estimating resonant frequencies

As in the flat bottom case above, the response of the interface in the basin with narrow shelves is a series of peaks in variance for each resonant basin mode (Fig. 3.2b and 3.2c). For the basin with shelves, however, as σ increases, the peaks no longer line up with the predicted σ_j for the modes in a flat basin (Fig. 3.2b). There is no analytical solution to predict the mode frequencies for the coupled system with shelves, so we estimate them using a shelf-weighted phase speed. The form for the coupled phase speed comes from the analytical solution for the flat basin, but now is solved for both the shelf depth, h_s, and the deep basin depth, 1, and then weighted by the shelf width, L_s, to predict the mode frequencies, σ_n, as follows:

$$c_s = \sqrt{\frac{1}{2}\left[(h_s + \rho(h_s - h_1)) \pm \sqrt{(h_s + \rho(h_s - h_1))^2 - 4\rho h_1(h_s - h_1)}\right]}, \tag{3.19}$$

$$c_d = \sqrt{\frac{1}{2}\left[(1 + \rho(1 - h_1)) \pm \sqrt{(1 + \rho(1 - h_1))^2 - 4\rho h_1(1 - h_1)}\right]}, \tag{3.20}$$

$$\sigma_n = n\pi \left[2L_s c_s + (1 - 2L_s)\, c_d\right] \,, (n = 1, 2, 3, ...)\,, \tag{3.21}$$

where c_s and c_d are the phase speed over the shelf and in the deep basin, respectively, and the factor of 2 in equation 3.21 comes from there being two shelves. These new shelf-weighted predictions for σ_n line up fairly well with the peaks (Fig. 3.2c, vertical dashed lines).

The values of σ at which the peaks begin to shift away from σ_j predicted for the flat basin (equation 3.17) and toward σ_n predicted for the basin with shelves (equation 3.21), are those σ for which the shelf width is at least a quarter the wavelength of a mode. This can be estimated by calculating the values of σ at which the shelf width is a quarter the wavelength of the excited baroclinic or barotropic modes, as in the following equation for $m = 1$:

$$\sigma_m = \frac{(2m-1)\pi}{2L_s} c_s \,, (m = 1, 2, 3, ...)\,. \tag{3.22}$$

Because baroclinic waves for a particular frequency have smaller wavelengths than barotropic waves, the shelves begin to influence the baroclinic modes for lower σ than for barotropic modes (Fig. 3.2c, first vertical solid green line). Subtracting the value of σ of the actual peak location from the predicted flat-bottom σ_j and shelf-weighted σ_n clearly demonstrates the shift in alignment for modes (Fig. 3.4a).

3.4.2.2 Mode structures

The structures of the modes become more complicated in the basin with narrow continental shelves. Where in the flat basin, there was a clear distinction between barotropic and baroclinic modes in the coupled system, in the basin with narrow shelves, this distinction is less clear. For example, in the basin with narrow shelves, the mode response that is most like barotropic mode 1 in the flat basin is no longer just the large-scale half cosine across the basin, but also includes small-scale baroclinic waves superimposed (Fig. 3.5a). We find that all of the modes associated with the barotropic σ_n have structures that are coupled like this, with barotropic and baroclinic wave scales superimposed. Note that this remains true when a smaller, realistic value for ρ is used (e.g. 0.01), just with smaller relative baroclinic sea surface amplitudes.

The less surprising effect of the shelves to decrease the frequency at which a particular mode occurs, relative to a flat basin, can be visually demonstrated by looking at a mode that has a quarter-wavelength greater than or equal to the shelf width (or, its frequency, σ_n, greater than or equal to $\sigma_{m=1}$). For the basin with narrow shelves, this occurs at baroclinic mode 12 (Fig. 3.2c, twelfth peak with green circle, just past the first solid vertical green line that indicates $\sigma_{m=1}$). Baroclinic mode 12 looks very similar to that in the flat basin, but over the shelves, the wavelength is slightly compressed due to the change in water depth, and thus the wavelength in the deep basin is slightly widened, overall requiring a lower frequency for the twelve zero crossings (Fig. 3.5b). As well, the amplitude over the shelves is slightly larger than in the deep basin and than the flat basin baroclinic mode 12.

3.4.3 Basin with wide continental shelves

These same shelf effects on the modes in the basin with narrow continental shelves are seen in the basin with wide continental shelves, often more strongly and at lower frequencies. As well, another shelf effect occurs that depends on the phase speed ratio between the shelf and deep basin.

3.4.3.1 Estimating resonant frequencies

The resonant frequencies for modes in the basin with wide continental shelves are estimated as they were for the basin with narrow shelves (equations (3.19-3.21)). The interface response is still a series of peaks in variance for each coupled basin mode (Fig. 3.2d and 3.2e) that line up better with the shelf-weighted estimate for σ_n than with σ_j for the flat-bottom basin (Fig. 3.4b and c) once the shelf width is wide enough compared to the mode wavelengths, which happens near the lowest modes for both the baroclinic and barotropic modes. While the modes do not stay lined up perfectly with the shelf-weighted estimates for σ_n, there is a one-to-one ratio of peaks and predicted σ_n modes for baroclinic responses, with each peak near its predicted σ_n, whereas there is not a one-to-one ratio of peaks and predicted modes for σ_j.

One of the most striking things about the results in the basin with wide shelves is that there are now 6 barotropic peaks for this range of σ, versus only 3 for the flat and narrow-shelved basins (Fig. 3.2). Four of these barotropic peaks are associated with the first four estimated shelf-weighted σ_n (for $n = 1, 2, 3$, and 4), which have shifted to low enough values to (almost) fit within the plotted range of σ (barotropic σ_n for

$n = 4$ is just beyond the range, at 11.06). But the other two peaks are associated with σ_m (equation (3.22)), the values of σ at which quarter wavelengths fit over the shelves. That is, one barotropic peak is associated with a quarter wavelength fitting over each shelf ($\sigma_{m=1}$), and one is associated with three quarter wavelengths over each shelf ($\sigma_{m=2}$). The six peaks for barotropic basin modes advance in order from one to six zero crossings, such that the value of n in σ_n is no longer necessarily the number of zero crossings, now that the quarter shelf waves are part of the series of basin modes. The two barotropic modes associated with σ_m have sea surface amplitudes that are amplified over the shelves relative to the deep basin, and thus are referred to as shelf-amplified basin modes.

Note that although in both the basins with narrow and wide shelves, baroclinic quarter waves fit over the shelves within the range of σ that we sweep through (Figs. 3.2c and 3.2e, solid vertical green lines), there are no baroclinic basin modes uniquely associated with the values of σ_m (there are no baroclinic shelf-amplified basin modes); each baroclinic peak is associated with a predicted shelf-weighted σ_n. The reason that there are barotropic shelf-amplified basin modes but no baroclinic shelf-amplified basin modes is that the barotropic phase speeds over the shelf and deep basin are sufficiently different from each other, whereas the shelf and deep basin baroclinic phase speeds are not sufficiently different.

Using the homogeneous phase speed, the barotropic ratio of phase speeds between the shelf and deep basin, δ_{BT}, is fairly small,

$$\delta_{BT} = \frac{c_{BT_{shelf}}}{c_{BT_{deep}}} = \sqrt{\frac{h_s}{H}} \approx 0.22\,, \tag{3.23}$$

indicating separation of the shelf and deep basin scales ($h_s = 0.05$, $H = 1$). However, using the rigid lid phase speed, we see that the baroclinic phase speed ratio between the shelf and deep basin, δ_{BC}, for this stratification is closer to 1,

$$\delta_{BC} = \frac{c_{BC_{shelf}}}{c_{BC_{deep}}} = \frac{\sqrt{\frac{\rho h_1 (h_s - h_1)}{h_s}}}{\sqrt{\frac{\rho h_1 (H - h_1)}{H}}} = \sqrt{\frac{H(h_s - h_1)}{h_s(H - h_1)}} \approx 0.70\,, \tag{3.24}$$

and thus there is less separation of shelf and deep basin scales ($h_1 = 0.02625$). The phase speed ratio, δ, must be small in order to shift the frequencies of basin modes to align with each σ_m and yield shelf-amplified basin modes, in addition to aligning with each shelf-weighted σ_n for basin modes. This will be further shown below, in section 3.4.3.3. Note that even if δ is not small enough to yield shelf-amplified basin modes, if a mode occurs near a value of σ_m (while still being associated with a σ_n basin mode), it can still have an amplitude that is larger over the shelves than in the deep basin.

3.4.3.2 Mode structures

The mode structures become more complicated for the basin with wide shelves. There is even less distinction between barotropic and baroclinic modes, mode frequencies are shifted to even lower values, and there are barotropic shelf-amplified basin modes. As shelf widths increase, categorizing the modes becomes more and more difficult. To aid in this, the phase between the sea surface and interface motions across the basin were compared, the variance of the sea surface and interface

were compared, and wavenumber spectra were investigated to determine the dominant components of the coupled modes (not shown). However, there is still some ambiguity in categorization for these coupled barotropic-baroclinic modes.

For example, barotropic mode 1 and baroclinic mode 11 both contain larger barotropic and smaller baroclinic wave scales superimposed, and the two modes are very similar to each other (Fig. 3.6a and b, blue and cyan lines). In barotropic shelf-amplified basin mode 1, which is associated with one quarter wavelength fitting across the shelves, while the baroclinic component dominates in the deep basin, the shelves are dominated by the quarter barotropic wave; whereas in baroclinic mode 11, the small-scale baroclinic waves dominate the amplitudes across the entire basin.

While barotropic mode 1 is more barotropic over the shelves and more baroclinic in the deep basin, the opposite can also occur, as for barotropic mode 3, which is more barotropic in the deep basin (Fig. 3.6a and c). This mode also clearly shows the widening of the wavelength in the deep basin compared to the flat basin barotropic mode 3 (Fig. 3.6c), correlating with the much lower frequency of barotropic mode 3 in the wide shelf basin (Fig. 3.2a and e).

3.4.3.3 Altering the ratio between phase speeds over the shelf and deep basin

In order to have baroclinic shelf-amplified basin modes, the ratio between shelf and deep basin baroclinic phase speeds, δ_{BC}, must be smaller. Looking at δ_{BC} from equation (3.24), because $h_1 << H$, we can approximate the lower layer depth in the

deep basin, $(H - h_1)$, to be the total depth, H, to show that increasing the upper layer thickness, h_1, thus decreasing the lower layer thickness over the shelf, $h_{2_{shelf}}$, will decrease the ratio:

$$\sqrt{\frac{H(h_s - h_1)}{h_s(\cancel{H - h_1})^{H}}} \approx \sqrt{\frac{h_{2_s}}{h_1 + h_{2_s}}} = \sqrt{\frac{1}{\frac{h_1}{h_{2_s}} + 1}}\,, \tag{3.25}$$

where the shelf depth is defined by the thickness of the two layers over the shelf: $h_s = h_1 + h_{2_s}$. Increasing the upper layer thickness to $h_1 = 0.0475$ for the basin with wide shelves to give approximately the same value for δ_{BC} as for δ_{BT} (~ 0.22), does result in baroclinic shelf-amplified basin modes (figure 3.7). Looking at the distribution of peaks compared to predicted σ shows that, whereas for the original basin with $\delta_{BC} = 0.70$, there are only peaks associated with basin modes σ_n and no peaks associated with shelf-amplified basin modes σ_m, for the basin with a thicker upper layer and $\delta_{BC} = 0.22$, there are both basin modes and shelf-amplified basin modes (Fig. 3.7). For the shelf-amplified basin modes, the interface displacement is amplified over the shelves relative to the deep basin.

Likewise, for the barotropic phase speed ratio (equation 3.23), when the depth of the shelf is increased to $h_s = 0.49$ such that δ_{BT} is increased to 0.70, there is no longer enough phase speed separation to have barotropic shelf-amplified basin modes (not shown). For barotropic and baroclinic modes, as their respective δ are shifted gradually from 0.22 to 0.70, modes shift gradually away from lining up with both σ_m and σ_n, to just lining up with σ_n. Thus, basins with small enough δ will have more modes occurring within a given range of σ, with both basin modes, σ_n, and shelf-

amplified basin modes, σ_m, and their structures will more often be amplified over the shelves. Basins with δ closer to 1 will have less modes occurring within a given range of σ, and their structures will less often be amplified over the shelves (although they will still be amplified over the shelves if occurring near a predicted σ_m).

3.4.4 Width of peaks

Inspection of the frequency response for the basins reveals that some resonant peaks have broader or narrower bases than others (Fig. 3.2). In the flat basin, the barotropic mode peaks are much broader than all but the peak for the lowest baroclinic mode. For the basin with wide shelves, however, the structures of the peak bases have changed such that some baroclinic modes now have broader peaks. As shelf widths increase, baroclinic mode peaks tend to broaden and rise above the forcing variance. For any mode, if it has a broad peak that is elevated above the variance of the forcing (Fig. 3.2, horizontal red lines), then that mode has a wider range of σ over which it can be excited, making it more likely for that mode to be able to be excited, or "tuned into". Thus, as shelf widths increase, some modes become easier to excite.

The width of a peak depends in part on the wavelength of the forcing relative to that of the mode. For example, we tested a forcing wavelength that was much smaller relative to the basin (approximately $\frac{1}{6}$th the basin length), and found that the higher modes, especially around (baroclinic) mode 12, had broader bases than the low modes. This could partly explain why the barotropic modes and the first

baroclinic mode have wider peaks: because they have large wavelengths, closer to the wavelength of the forcing. This could be in part why the peak widths vary as shelf widths increase: as shelf widths increase, the wavelengths of the modes change, getting longer in the deep basin and thus closer to the large scale of the forcing wavelength.

Note also that it is unlikely that numerical damping is very big, and is thus not the factor controlling the width of the base of the peaks. This is based on the fact that as the resolution of σ is increased, refining the grid about resonance, the response peak heights continue to grow. As well, when looking at a damped linear oscillator, the off-resonant response is independent of the damping coefficient except very near the resonant frequency, resulting in identical peak base structures as damping strength is varied.

3.5 Two-dimensional problem, no rotation

When we add the y-dimension to the basins (Fig. 3.8), in addition to basin modes that can be predicted by the shelf-weighted phase speed or shelf-amplified basin modes predicted by quarter-wavelengths fitting across the shelves, a new type of resonant response can occur: edge wave modes that are evanescent in the deep basin.

3.5.1 Estimating resonant frequencies

3.5.1.1 Edge wave modes

For the shelf/deep basin geometry used here, edge wave modes are predicted to occur when quarter-waves fit across the shelves and when the response is evanescent in the deep basin (Chapman 1982). Evanescence in the deep basin can be predicted for basins with shelves only at the eastern and western boundaries, with no bathymetric variability in the y-direction (Fig. 3.8). In these limits, the equations for the free (unforced) solutions are separable in x and y, and can thus be used to determine the behavior of solutions in the deep basin. It is easiest to look at homogeneous and rigid lid basins to derive a condition for when modes will be evanescent in the deep basin and thus trapped to the shelves, and then to confirm this condition for the coupled barotropic-baroclinic basins.

For a homogeneous basin, the unforced equation is

$$\frac{\partial^2 N'}{\partial x^2} + \frac{\partial^2 N'}{\partial y^2} + \frac{1}{h}\frac{\partial h}{\partial x}\frac{\partial N'}{\partial x} + \frac{\sigma^2}{h}N' = 0\,. \tag{3.26}$$

Separating the sea surface motion into x- and y-components, $N'(x,y) = X(x)Y(y)$, reveals that $Y(y)$ is just a series of cosines with wavenumber $\nu_q = q\pi/L_y$ (for $q = 0, 1, 2, ...$), as expected for no bathymetric variability in that direction. Thus the $X(x)$ equation to solve is

$$X'' + \frac{\partial h}{\partial x}\frac{1}{h}X' + \left(\frac{\sigma^2}{h} - \nu_q^2\right)X = 0\,. \tag{3.27}$$

In the deep basin, $\frac{\partial h}{\partial x} = 0$ and $h = 1$, and therefore we see that solutions in x are

exponential in the deep basin, and thus evanescent, when $\sigma^2 < \nu_q^2$.

The same process can be followed for a two-layer rigid lid basin, revealing that solutions in x are evanescent in the deep basin when $\sigma^2 < \rho h_1(1-h_1)\nu_q^2$. Therefore, in both the homogeneous and rigid lid cases, the trapping condition for evanescence is that the frequency must be less than the deep basin phase speed (which is just 1 for the homogeneous basin) times the y-wavenumber. Applying that rule to the coupled system predicts that modes will be evanescent in the deep basin when $\sigma < c_d \frac{q\pi}{L_y}$, where the deep basin phase speed, c_d, is defined as in equation (3.20). Therefore, edge wave modes are predicted when that trapping condition is met and quarter waves fit across the shelf (Figs. 3.9 and 3.10, black circles), as follows:

$$\sigma_{m,q} = \sqrt{c_s^2 \left[\left(\frac{(2m-1)\pi}{2L_s} \right)^2 + \left(\frac{q\pi}{L_y} \right)^2 \right]}, (m = 1, 2, 3, ...;\ q = 1, 2, 3, ...)\,, \qquad (3.28)$$

where the equation structure is the same as for the one-dimensional problem in x, now with the y component added to it, and the phase speed for the shelf, c_s, is defined in equation (3.19).

Next, we can look at the equations for the coupled barotropic-baroclinic system (equations 3.10 and 3.11) to see if they derive the same condition for evanescence in the deep basin. Combining those equations into one fourth-order equation with $\frac{\partial h}{\partial y} = 0$, $f = 0$, and no forcing, then breaking the solution into separable components and assuming the $Y(y)$ solutions are cosines with wavenumber $\nu = q\pi/L_y$, yields the

$X(x)$-equation

$$X''''+\left[\frac{\sigma^2(h+\rho(h-h_1))}{\rho h_1(h-h_1)}-2\nu^2\right]X''+\left[\nu^4-\frac{\sigma^2(h+\rho(h-h_1))}{\rho h_1(h-h_1)}\nu^2+\frac{\sigma^4}{\rho h_1(h-h_1)}\right]X=0\,. \tag{3.29}$$

For ease of notation in the following solution, we define two parameters: $\phi = 1 + \rho(1-h_1)$ and $\theta = \rho h_1(1-h_1)$. In the deep basin, $h = 1$, and seeking solutions of the form $e^{\mu x}$ yields:

$$\mu = \pm\sqrt{-\left(\frac{\sigma^2\phi-2\nu^2\theta}{2\theta}\right)\pm\frac{1}{2}\sqrt{\left(\frac{\sigma^2\phi-2\nu^2\theta}{\theta}\right)^2-4\left(\frac{\sigma^4-\sigma^2\phi\nu^2+\nu^4\theta}{\theta}\right)}}\,. \tag{3.30}$$

When μ is imaginary, solutions are oscillatory sines and cosines. When μ is real, solutions are exponential, indicating evanescence in the deep basin. It is not immediately clear what conditions lead to real μ, but solving for μ using values of the parameters for our basins and comparing the results to the predicted trapping condition confirms that the prediction is correct: solutions are evanescent when $\sigma < c_d\frac{q\pi}{L_y}$.

Above this trapping condition, $\sigma_{m,q}$ results in shelf-amplified basin modes (Figs. 3.9 and 3.10, red circles). Thus, for a fixed alongshelf (North-South) mode number, q, as σ increases, modes that fit a quarter wave across the shelf (described by $\sigma_{m,q}$, equation 3.28, red and black circles in Figs. 3.9 and 3.10) transition from being edge modes to being shelf-amplified modes as σ increases beyond the trapping limit. There are a fixed number of trapped edge modes for each alongshelf mode number. As alongshelf mode number increases, this trapping limit occurs for higher and higher σ, similar to the trapping condition found in Huthnance (1975) for barotropic (su-

perinertial) edge waves in a homogeneous ocean on an f-plane, beyond which exists a Poincaré continuum of waves that are not trapped.

We will show below that because edge modes are evanescent in the deep basin, they should not be affected by the deep basin geometry. Shelf-amplified modes do depend on the deep basin geometry.

3.5.1.2 Basin modes

We predict basin modes in the two-dimensional problem in the same way as for the one-dimensional problem, now with the contributions from modes in the y-direction included. The shelf-amplified basin modes that come from fitting a quarter wavelength across the shelf thus share equation (3.28) with the edge wave modes, except here we want the imaginary solutions that oscillate in the deep basin, so we must have $\sigma > c_d \frac{q\pi}{L_y}$ (Figs. 3.9 and 3.10, red circles). The other basin modes (Figs. 3.9 and 3.10, green circles) come from:

$$\sigma_{n,p} = \sqrt{\left[2L_s c_s + (1-2L_s)c_d\right]^2 (n\pi)^2 + c_d^2 \left(\frac{p\pi}{L_y}\right)^2}\,, (n = 1, 2, 3, ...;\; p = 1, 2, 3, ...)\,. \tag{3.31}$$

3.5.2 Mode structures

We solved the two-dimensional problem in a flat-bottom basin and in a basin with wide shelves on the east and west, with bathymetry that varies only in the x-direction

with the same x-structure as for the one-dimensional problem (Fig. 3.8). Thus, as described above, the modes are separable in x and y, so the x-wavenumber does not vary in y and vice-versa.

Introducing the y-dimension into the basins results in more modes within a given range of σ and in mode structures that are more complicated, and modes do not always occur in the order they are predicted to occur in by the series of $\sigma_{n,p}$ and $\sigma_{m,q}$. Thus, it is increasingly challenging to resolve all of the peaks for all of the predicted modes and to identify which peak is associated with each mode. For example, in the basin with wide shelves and small phase speed ratios (0.22) for both δ_{BT} and δ_{BC}, there are 415 modes predicted to occur for a range of σ from 0 to 5.25, but only 103 peaks were resolved in our method of sweeping through discrete σ (Fig. 3.11, comparing number of vertical lines (415) to number of peaks (103)). In the basins that follow, we did not identify each predicted mode, but found examples of each type of predicted mode: barotropic and baroclinic basin modes, shelf-amplified basin modes, and edge modes. We will show examples of barotropic structures below for the basin with wide continental shelves and large $\delta_{BC} = 0.70$, and baroclinic mode structures for the basin with wide continental shelves, comparing the results between $\delta_{BC} = 0.70$ and $\delta_{BC} = 0.22$ (all basins have small $\delta_{BT} = 0.22$).

Exploring the results for baroclinic modes, we found that edge modes take the place of their "equivalent" basin modes. For example, we could find a resonant peak in response for each predicted edge mode with a quarter wave across the shelf in the x-direction and any multiple of half-wavelengths along the shelf, but we could not find resonant peaks for any of the predicted basin modes with no zero-crossings in

the x-direction and the same multiple of half-wavelengths in the y-direction along the shelf as for the edge mode. Full basin modes cannot occur for these wave scales because they are evanescent in the deep basin, which is what makes them occur as edge modes and only as edge modes.

3.5.2.1 Flat basin

The modes in the flat basin occur at predicted $\sigma_{n,p}$ (for $L_s = 0$) and the structures are what we would expect: barotropic or baroclinic standing cosine waves in the x- and y-directions, with the number of zero crossings in the x- and y-directions (the mode numbers) indicated by the subscript values of n and p, respectively. Note that as you advance through increasing $\sigma_{n,p}$, n and p do not increase monotonically: one of them can decrease as the other increases. For example, as σ increases, the first peak in response is baroclinic mode one in the x-direction and zero in the y-direction; the second peak is baroclinic mode zero in the x-direction and one in the y-direction; and the third peak is mode two in the x-direction and zero in the y-direction.

3.5.2.2 Basins with wide continental shelves

In the basin with wide shelves and $\delta_{BC} = 0.70$ (that is, when the baroclinic phase speeds over the shelves and deep basin are similar), there are barotropic and baroclinic basin modes and shelf-trapped edge modes, but shelf-amplified basin modes only occur for barotropic modes, not for baroclinic. This was seen by comparing (not

shown) the frequency and structure of each resonant response with the frequencies and structures of predicted possible modes in Figs. 3.9 and 3.10 (from equations 3.31 and 3.28). This basin mode behavior is consistent with the results from the one-dimensional problem: in order for shelf-amplified basin modes to occur, δ must be small enough. For this basin, δ is small enough for barotropic modes, but not for baroclinic. When the interface is deepened to decrease δ_{BC} to 0.22, just as for the one-dimensional problem, baroclinic shelf-amplified basin modes occur. Thus, in the basin with $\delta_{BC} = 0.22$, there are both barotropic and baroclinic shelf-amplified basin modes, as well as basin modes and shelf-trapped edge modes.

Note that δ does not need to be small in order to have shelf-trapped edge modes: barotropic and baroclinic edge modes occur regardless of the ratio of shelf and deep basin phase speeds. But the ratio δ is important in determining how much mode structures are affected by shelves. A lower ratio shifts the series of edge modes and shelf-amplified basin modes to lower values of σ, resulting in more edge modes within a given range of σ (Fig. 3.10b versus 3.10c). As well, we show below that a lower ratio results in edge modes that are more shelf-confined than in a basin with a larger ratio.

The barotropic modes all include baroclinic wave scales superimposed in their structures (Figs. 3.12 - 3.14), just as in the one-dimensional problem. This is true even for the barotropic shelf-trapped edge modes, for which the baroclinic part is not necessarily evanescent in the deep basin, causing shelf trapping to be imperfect (Fig. 3.14). The result is a structure that is barotropic over the shelves, with the barotropic component decaying into the deep basin, and a baroclinic component that

persists with large amplitudes throughout the basin (Fig. 3.14). As in the one-dimensional problem, some two-dimensional baroclinic modes have coupling of large-scale barotropic waves superimposed (not shown).

The first three barotropic modes demonstrate the three mode types, as predicted (Fig. 3.9b): a shelf-amplified basin mode that is mode one in the x-direction (for the barotropic wave scale) and mode zero in the y-direction (Fig. 3.12); a basin mode that is mode two in the x-direction (for the barotropic wave scale, which has its two crests over the shelves and its trough throughout the deep basin) and mode zero in the y-direction (Fig. 3.13); and a shelf-trapped edge mode that fits a barotropic quarter-wave across the shelves and is mode one in the y-direction (Fig. 3.14). All of the mode structures are standing waves.

Because these basins have a shelf on both the east and west ends of the basin, for each predicted shelf-trapped edge mode, there are two peaks that can be found, with slightly different frequencies: one which has symmetric signs on the opposite shelf, and one which has opposite signs on the opposite shelf. This is a consequence of the basin geometry we chose, with symmetric shelves on either end of the basin. (Fig. 3.14 shows that with opposite signs.)

The first three peaks for the basin with $\delta_{BC} = 0.22$ demonstrate the three types of baroclinic modes (Figs. 3.10c and 3.11). The first peak is a baroclinic basin mode, and is mode one in the x-direction and mode zero in the y-direction, as predicted by shelf-weighted $\sigma_{n,p}$ (Fig. 3.15b and 3.15d). While this is not a shelf-amplified basin mode, the interface motions are still amplified over the shelf relative to the deep basin, because this mode occurs at a value of σ near that of a shelf-amplified

basin mode. The same mode in the basin with $\delta_{BC} = 0.70$ shows a structure that is not affected by the shelves (Fig. 3.15a and 3.15c). Peak two for $\delta_{BC} = 0.22$ is a baroclinic shelf-amplified basin mode (Fig. 3.16b and 3.16d). The equation for $\sigma_{m,q}$ that predicts shelf-amplified basin modes predicts this to be a quarter wave across the shelf and mode zero in the y-direction, and this mode is consistent with that, while serving as mode two in the x-direction and mode zero in the y-direction. Here, amplification over the shelf is more pronounced than for the preceding peak. For the equivalent mode–a basin mode–in the basin with $\delta_{BC} = 0.70$, the structure is only slightly affected by the shelves (Fig. 3.16a and 3.16c). The third peak for $\delta_{BC} = 0.22$ is a baroclinic shelf-trapped edge mode, with a quarter wave across the shelves and mode one in the y-direction, as predicted by $\sigma_{m,q}$ (Fig. 3.17b and 3.17d). The decay in amplitude into the deep basin is more pronounced in the interface than sea surface because the amplitudes over the shelf are much greater in the interface than sea surface. The "equivalent" mode in the basin with $\delta_{BC} = 0.70$ is a basin mode with amplitudes over its shelves similar to in its deep basin (Fig. 3.17a and 3.17c).

For edge modes, as mode number increases in the y-direction (i.e. as q increases in equation 3.28), the decay of amplitude into the deep basin is more rapid in x, and over the shelf, the interface amplitude becomes even larger relative to the sea surface (compare Fig. 3.18c and 3.18d to Fig. 3.17b and 3.17d), reaching a relative amplitude approximately consistent with rigid lid theory over the shelf depth ($\eta_{BC} \sim -\rho\frac{h_2}{h_s}\zeta_{BC}$, so for $\delta_{BC} = 0.22$, $\eta_{BC} \sim 0.0125\zeta_{BC}$ and thus $\zeta_{BC} \sim -80\eta_{BC}$, and for $\delta_{BC} = 0.70$, $\eta_{BC} \sim 0.119\zeta_{BC}$ and thus $\zeta_{BC} \sim -8.4\eta_{BC}$). Comparing the same baroclinic edge mode between the basins with $\delta_{BC} = 0.70$ and $\delta_{BC} = 0.22$, we see that the edge mode

is more shelf-confined (decays more rapidly in x) in the basin with the smaller δ_{BC} (Fig. 3.18a and 3.18b versus 3.18c and 3.18d). In our basins presented here, shelf depth has been held fixed at $h_s = 0.05$. We also looked at the resonant modes in basins with a much deeper shelf depth, $h_s = 0.5$, and by choosing the appropriate upper layer depth, h_1, compared the resonant modes between $\delta_{BC} = 0.70$ and $\delta_{BC} = 0.22$. We found that the modes in the basins with $h_s = 0.5$ were qualitatively similar to those in the basins with $h_s = 0.05$ with the same δ_{BC} value (not shown). Thus, even though the shelves were dramatically deeper in the second set of basins, the impact of the shelves on the mode structures was dominated by the value of δ_{BC}. Additionally, we looked at the resonant modes in a basin like our original basin with $h_s = 0.05$ and $\delta_{BC} = 0.22$, but with a much weaker stratification ($\rho = 0.025$), and the modes were qualitatively the same as those in the basin with ($\rho = 0.25$) (not shown). The value of δ is important in determining the effects of shelves on resonant mode structures.

To demonstrate that edge modes do not depend on deep basin geometry, we extended the deep basin in the basin with $\delta_{BC} = 0.22$ such that the total basin length is 50% larger than the original length, keeping all other basin geometry the same, and show that the response at the same dimensional forcing frequency, σ^*, is the same edge mode (Fig. 3.18e and 3.18f). The non-dimensional σ does change, because it is non-dimensionalized using the basin length, such that because the extended basin length, $L^*_{x_2}$, is 1.5 times the original length, $L^*_{x_1}$, $\sigma_2 \approx 1.5\sigma_1$. For this mode, $\sigma_1 = 0.557$, and both predicted and actual $\sigma_2 = 0.836$. This indicates that because edge modes do not depend on deep basin geometry, they do not need to communicate across the entire basin to develop, meaning they can set up more quickly than basin modes in

the same basin.

3.5.3 Width of peaks for the two-dimensional problem with no rotation

In the two-dimensional problem without rotation, the series of peaks in variance show that wide peaks only occur for baroclinic and barotropic basin modes that are mode zero in the y-direction, and that most shelf-amplified modes, even if mode zero in the y-direction, have fairly narrow peaks. Basin modes that are mode zero in the y-direction do not always have wide peaks, but they are the only ones that can have wide peaks. For example, in the basin with wide shelves and $\delta_{BC} = 0.22$, the first peak, baroclinic basin mode $x1$ and $y0$, has a wide base; the second peak, shelf-amplified baroclinic basin mode $x2$ and $y0$, has a narrow peak; and the third and fourth peaks, one-quarter wave shelf-trapped baroclinic edge mode and $y1$, have very narrow peaks (Fig. 3.11).

The equilibrium tide forcing does not vary much in the y-direction, so that helps to keep the modes with y-variability narrow-peaked. In these basins without rotation and with $\partial h/\partial y = 0$, the solution for the modes is separable in x and y (as discussed in the derivation of predicting edge modes). Thus, the y-component of a mode's structure is not affected by variability in the x-direction (it has a zero derivative in x). It may be that these peak width differences are a consequence of our basin geometry. If our basin geometry were rotated by 90°, we would have non-zero $\partial h/\partial y$ and $\partial h/\partial x = 0$. In that case, we might see wider peaks for the higher y-modes and

more narrow peaks for the higher x-modes, however we did not test this.

3.6 Two-dimensional problem, with rotation

Adding rotation (on an f-plane) to the basins, the solution is no longer separable in x and y, so the y mode structure can vary in x and vice-versa. Rotation allows for Kelvin waves (in addition to the Poincaré waves and edge waves). The previously standing seiche mode structures can now have phase that propagates. We do not have equations for predicting modes when rotation is included, but we see that there are the same kinds of modes as in the basin without rotation: basin modes; shelf-amplified basin modes, and shelf-trapped edge modes. With rotation, the modes become even more complicated and difficult to interpret as barotropic or baroclinic, and whereas before we could consider mode numbers in the x- and y-directions, we can no longer count zero crossings in the two directions independently, because the zero-crossings propagate.

Phase propagation in these basins can be very complicated, especially for higher-wavenumber modes. Phase can propagate counterclockwise (CCW, cyclonically) or clockwise (CW, anticyclonically), or have opposite senses of rotation over the shelves versus deep basin. Neighboring amphidromes on the shelf or in the deep basin can have alternating senses of rotation and, depending on the amplitude distribution, lead to waves that clearly propagate phase around amphidromes, or that appear almost as standing high and low bands that oscillate. Edge modes can propagate phase along the shelf or appear to have an almost standing pattern due spatially variable

amplitude along the shelf and high-wavenumber shelf structure. We will show several examples of these different structures in the two-dimensional rotating basin with wide shelves, below.

Because of the large value of ρ used which emphasizes the coupled baroclinic response of the sea surface, barotropic modes were difficult to distinguish from baroclinic modes. The method of sweeping through σ to find resonant modes resolved two resonant responses in the basin with $\delta_{BC} = 0.70$ that have barotropic components that closely resemble barotropic modes in the non-rotating basin. The first looks similar to the barotropic shelf-amplified basin mode that is mode one in the x-direction and mode zero in the y-direction (Fig. 3.19 compared to Fig. 3.12). In the rotating basin, the barotropic structure over the shelves propagates phase along the shelves, cyclonically, and the sea surface has its greatest amplitudes over the shelves, while the coupled baroclinic component phase propagation is more complicated, and with the amplitude distribution, results in what almost looks like standing oscillating high and low bands oriented along the y-direction, across the deep basin (Fig. 3.19). The coupled baroclinic component in the rotating basin has a lower wavenumber in the x-direction than in the non-rotating basin, but in the y-direction the rotating basin appears to have a higher wavenumber baroclinic structure than in the non-rotating basin. The second example looks similar to the barotropic edge mode that has a quarter wave across the shelves and that is mode one in the y-direction (Fig. 3.20 compared to Fig. 3.14). Again, the barotropic component is of maximum amplitude over the shelves and has phase that propagates alongshelf, cyclonically. The smaller-scale baroclinic structures over the shelf also have phase that propagates alongshelf,

cyclonically. In this resonant, perhaps barotropic edge mode, response, the largest amplitudes for the baroclinic interface are also isolated to the shelves, although there is still baroclinic energy that persists throughout the deep basin (Fig. 3.20).

The first three resonant peaks in the basin with wide continental shelves, on an f-plane, with $\delta_{BC} = 0.22$, correspond to the baroclinic modes of the first three peaks in the same basin without rotation, discussed previously in Figs. 3.15-3.17, appearing similar to Kelvin waves in a channel in the basin with rotation. These modes (and others) show that if a basin mode is close to a Kelvin wave dispersion curve, we get a mode that is close to a Kelvin wave. The first peak is like the baroclinic basin mode with one zero crossing in the x-direction (Fig. 3.15), but that node is now a central amphidrome around which phase propagates cyclonically (Fig. 3.21). As in the non-rotating basin, motions are amplified over the shelf, particularly in the interface, but amplitudes are still substantial in the deep basin. If we use the rigid lid baroclinic phase speed to solve for the predicted alongshore wavelength of an internal Kelvin wave in the deep basin for the given frequency ($\lambda = 2\pi\sqrt{\rho h_1(1-h_1)}/\sigma$), we get 2.479. This is a little large for what is observed in the mode structure, in part because this is an enclosed basin and because there are shallower shelves that also affect the basin mode structure. If we use a shelf-weighted rigid lid phase speed, similar to that used for σ_n (equation 3.21), but using rigid lid phase speeds, to account for the shelves, the predicted wavelength is 1.974, which is closer to what is observed in the mode. The second peak is like the baroclinic shelf amplified basin mode with two zero crossings in the x-direction (Fig. 3.16), but now those two nodes are two central amphidromes around which phase propagates cyclonically, and shelf amplification is larger than in

the previous mode (Fig. 3.22). The interface motions are dominated by a quarter-wavelength across the shelves, that propagates cyclonically along the shelves, but the mode is still visible throughout the basin. The predicted internal Kelvin wavelength for this mode in the deep basin is 1.867, which looks very close to that observed (using a shelf-weighted phase speed gives 1.487). The third peak is like the baroclinic shelf-trapped edge mode with a quarter wave across the shelves and one zero crossing in the y-direction (Fig. 3.17), but now the previously standing shelf wave propagates phase along the shelves, with little motion in the deep basin relative to the shelves, like a shelf-trapped alongshore propagating superinertial ($f = 0.73$) internal tide (Fig. 3.23). For this mode, the predicted deep basin internal Kelvin wavelength is 1.751, which seems big for the alongshore structure in the deep basin, and the shelf-weighted phase speed gives 1.395, which seems closer, but because this is likely an edge mode, the response over the shelf should be a result of the shelf structure. Solving for the predicted internal Kelvin wavelength along the shelf ($\lambda = 2\pi\sqrt{\rho h_1(h_s - h_1)/h_s}/\sigma$) gives 0.401, which looks close (a little small) to that seen alongshelf. It would make sense for an internal Kelvin-like wave to be able to exist over the shelf, because the flat shelf meets a coastal boundary that is a vertical wall, and the stratification does not intersect the bathymetry, so it sees the coastal wall as its boundary.

To test if this third mode is an edge mode, we searched for the same edge mode in a basin with an extended deep region but forced at the same dimensional frequency, and we found that the same edge mode structure occurred, indicating that it is an edge mode (Fig. 3.24 compared to Fig. 3.23). Interestingly, the deep basin in the regular basin and the extended basin both have a single amphidrome around which

a baroclinic response propagates. The non-dimensional σ at which this edge mode occurs in the extended basin should be around 1.5 times that for the regular basin mode, which, for $\sigma_1 \approx 0.382$, should be around $\sigma_2 \approx 0.573$. However, the edge mode in the extended basin was found at a slightly lower value, at $\sigma_2 \approx 0.556$. It may be that this value is slightly low because the deep basin is still closer to one amphidrome fitting across it than two, so since that wavelength is a little longer in the extended deep basin length, it makes the frequency slightly lower. We hypothesize that if we keep extending the deep basin length, there would eventually be two amphidromes along x in the deep region, increasing the frequency slightly to be closer to 1.5 times the original frequency. Thus, as the basin were continually expanded, the frequency of this edge mode would slightly decrease and increase in this manner, as more amphidromes were added to the deep region. This lower than predicted σ value could also be related to the fact that the edge mode equation does not include the effects of rotation, but this basin does have rotation.

Looking at some higher baroclinic modes for the standard basin with wide shelves and $\delta_{BC} = 0.22$, we see examples of the different general types of phase propagation, other than just the cyclonic phase propagation around the basin and along the shelves seen in the first three baroclinic mode examples. In Fig. 3.25, we see a baroclinic mode in which large amplitudes of the sea surface and in the deep basin of the interface have phase that propagates CCW around the boundary of the deep basin while large amplitudes (in the interface) over the shelf have phase that propagates in the opposite direction, CW along the coasts. In the next example (Fig. 3.26), the large-amplitudes of the sea surface and in the deep basin of the interface have phase

that propagates CCW around the perimeter of the basin, appearing Kelvin wave-like, while the large amplitudes of the interface over the shelf have a row of amphidromes along the coast that are CCW and another row along the shelf edge that are CW. The resulting shelf interface motion looks like three somewhat circular blobs of positive and negative pairs of interface displacement, that propagate alongshelf northward, with pulsing between maximum amplitudes being positive or negative, on each shelf. Calculating the deep basin alongshore Kelvin wavelength gives 0.481, while the shelf-weighted rigid lid phase speed gives 0.383. The actual alongshore wavelength of the deep basin is ~ 0.412.

While all of the previous baroclinic modes presented for the basin with rotation have phase that can be seen to propagate, complicated phase structures and amplitude distribution can also result in what appears to be phase that does not propagate, creating a pattern of bands that oscillate between high and low, appearing more like the modes in the non-rotating basin. This can happen over the shelf (Fig. 3.27) or in the deep basin (Fig. 3.28). These structures look somewhat like Poincaré waves in a channel with an along-channel wavenumber of zero, therefore not propagating but acting as standing waves spanning the channel (Gill 1982), with either the shelf (Fig. 3.27) or the deep basin (Fig. 3.28 and 3.19) acting as the "channel". Sometimes these banded structures do propagate, as in the example in Fig. 3.29, where the interface over the shelf looks similar to the standing banded pattern in Fig. 3.27, but now the bands propagate CW along the shelves as they pulse between high and low. At least one of the baroclinic modes that we hypothesize to be an edge mode has a similar banding pattern over the shelf, with the bands now oriented across-shelf,

with a high wavenumber along the shelf and three-quarter wavelengths across the shelf (the quarter closest to the coast can be seen at another time step) (Fig. 3.30). For this mode, the large-amplitude bands appear almost standing, although phase is propagating CW around small-scale amphidromes over the shelf.

It is not clear if perhaps some of the other baroclinic examples presented are edge modes, but some of them do show multiples of quarter-wavelengths fitting across the shelves with amplitudes much larger on the shelf than in the deep basin (e.g. Figs. 3.26, 3.27, 3.29). This could be tested for select modes by extending the deep basin and forcing at the same dimensional frequency, as done before for the confirmed baroclinic edge mode in the rotating basin with a quarter wave across the shelf and one zero crossing along the shelf (Fig. 3.24), to see if we get the same shelf response. If these modes (and other examples from the hundreds of resonant peaks resolved) are edge modes, this demonstrates that resonant mode large-amplitude superinertial internal tides can occur over the shelf with many different (complicated) phase propagation structures.

Looking at the resonant baroclinic modes overall, we see that the lowest modes seem to be more Kelvin wave-like, with CCW propagation around amphidromes, and that as σ increases, we start to see modes that can propagate CW, so they must also include Poincaré waves, because the sense of propagation can be in either direction for Poincaré waves. For barotropic Poincaré waves to exist in a channel, the channel width squared must be greater than $\pi^2 c^2/(\sigma^2 - f^2)$ (Gill 1982). If we use the baroclinic rigid lid phase speed for c in that equation, if our basin was a channel in the y-direction, for the basin with $\delta_{BC} = 0.22$, we would get that the dimensional width

of the "channel" in the y-direction, L_y^*, must be greater than 693 km. If we consider variations in σ to be due to changing basin size, then this occurs for $\sigma = 0.984$. For a channel in the x-direction, the "channel" is wide enough for $\sigma = 0.492$. The first mode in our basin that has CW rotation somewhere in the basin occurs when $\sigma = 0.521$, and this is along the shelf edge. By $\sigma = 0.908$, there is CW rotation in the deep basin. Perhaps the reason the lowest modes in our basins are more Kelvin like is because the basin is not yet large enough (or the frequency is not yet high enough) to allow for Poincaré modes.

3.6.1 Width of peaks for the two-dimensional problem with rotation

The third peak in the basin with $\delta_{BC} = 0.22$ (that of the first baroclinic edge mode, with one-quarter wave across shelf and mode one in the y-direction, Fig. 3.23) has a width that is almost as wide as the first peak (that of the first baroclinic basin mode, with one central amphidrome, Fig. 3.21) (not shown), indicating that with rotation, wide peaks are no longer limited to modes that are mode zero in the y-direction. Therefore, with rotation, certain modes can become easier to excite. This is because when rotation is added, the solution for modes is no longer separable in x and y, so the y-component of a mode's structure is affected by variability in the x-direction.

3.7 Discussion and conclusions

To study coupled barotropic-baroclinic basin modes, we began with the one-dimensional problem with no rotation, first in a flat basin and then in basins with varying bathymetry, moving to two dimensions, and finally to include rotation, in order to begin with an analytical solution for the modes that could be built upon as the basins became more complicated. From the analytical solution, we saw that a two-layered basin has both barotropic and baroclinic basin modes that can be resonantly excited, even without bathymetric variability. Modes that were standing cosine waves in non-rotating basins become waves with phase that propagates in rotating basins.

We have shown the types of coupled resonant modes that can exist (basin modes, shelf-amplified basin modes, and shelf-trapped edge modes) and how they are affected by basin size, continental shelves, the ratio of the shelf and deep basin phase speeds (δ), and rotation on an f-plane. If we consider changes in σ to be changes in basin length, L_x^*, for the fixed dimensional forcing frequency of the $M2$ tide, then the basin size affects whether or not a resonant basin mode will occur. Note that as L_x^* increases, so does the shelf width in our basins (except in the extended basin cases shown), thus affecting whether or not a shelf-amplified mode or an edge mode will occur. In real ocean basins, thus, the basin geometry or shelf geometry must be appropriately tuned to that required by a basin mode or edge mode in order for a mode to be excited. A shelf must be at least as wide as a quarter the wavelength of a mode in order to influence (lower) mode frequencies and wavelengths. δ must be fairly small (0.70 is too large, 0.22 is small enough) to shift mode frequencies low enough to line up with

both basin mode and shelf-amplified basin mode predicted frequencies, thus yielding even more modes within a range of σ. In addition to affecting the frequencies at which modes occur, δ also dictates how much mode structures will be affected by shelves, with shelf amplitudes larger relative to the deep basin for basins with lower δ, and with edge modes being more shelf-confined (decaying faster into the deep basin) for basins with lower δ. Note that as the shelf phase speed decreases, giving a lower δ, the Rossby radius of deformation over the shelf, which is just the phase speed over the shelf divided by f, also decreases, perhaps aiding in the enhanced off-shelf decay of edge modes. Rotation introduces Kelvin waves and phase-propagation into the modes, and by making the problem no longer separable, allows the y-structure to vary in x and vice-versa. Phase can propagate CW or CCW and, in combination with amplitude distribution, result in structures that look like propagation of phase along the entire shelf, propagation around small-scale cells, or almost standing structures like those in the non-rotating basins.

In the real ocean, there is another aspect of the basin size that is important in determining whether a resonant mode can be excited, which depends also on time scales over which stratification changes. In order for a basin to come into equilibrium to fully develop a resonant basin mode, each part of the basin must communicate with the rest, which means that a full basin mode can only set up if its wave can propagate across the entire basin before stratification changes detune the mode. Since barotropic waves depend minimally on stratification and since they propagate much faster than baroclinic waves (two orders of magnitude faster in ocean basins), only barotropic basin modes will develop in large basins. A barotropic wave can propagate

across a large ocean basin such as the North Pacific in less than a day, so barotropic basin modes should be able to develop in almost any basin that is properly tuned for a barotropic mode, as demonstrated by the works of Platzman showing the agreement of some observed barotropic tides with various basin modes (Platzman et al. 1981; Platzman 1984b). The larger the basin, the longer it will take to propagate across it, so it is very unlikely that basin mode internal tides would exist in a large ocean basin such as the North Pacific or North Atlantic, because it would take seasonal time scales for a baroclinic wave to propagate all the way across these basins, and in that time, stratification changes would significantly impact the structure of baroclinic waves, detuning the mode. Even if stratification did stay constant in time, stratification across a large basin is not in general uniform in space. However, in a smaller basin, such as the Gulf of California, Gulf of Mexico, or Red Sea, an internal wave could propagate fully across the basin in about a week (based on an internal wave with a 3 m/s phase speed propagating across the full basins) and thus potentially develop a basin mode internal tide before changes in stratification, such as seasonal changes, occur. This is in agreement with observations of resonant internal tides in Upper Loch Linnhe fjord (Allen and Simpson 2002; Winant 2010) and the Strait of Juan de Fuca/Strait of Georges system (Martin et al. 2005; Winant 2010).

The fact that modes in the coupled barotropic-baroclinic system in basins with bathymetric variability often contain both barotropic and baroclinic wave scales superimposed (always for barotropic modes, and often for baroclinic modes occurring near barotropic modes in σ-space), means that in basins that are small enough, resonant excitation of a mode could result in both large-amplitude barotropic and

large-amplitude baroclinic tides. However, because their wavelengths are very large, barotropic modes for the $M2$ forcing frequency exist only in very large basins, such as the Atlantic and Pacific Oceans, and these basins are far too large to have resonant baroclinic tides. So, for the $M2$ frequency, it is unlikely that this kind of coupled mode excitation, with both large-amplitude barotropic and baroclinic tides, will be observed. But perhaps this kind of coupled mode excitation could be seen in a smaller basin that is tuned to a coupled mode with one of the higher frequency tidal constituents. Note that when a smaller (more realistic) value for ρ is used, this mixing of modes still occurs, just with smaller baroclinic sea surface displacements and smaller baroclinic wavelength scales for a particular barotropic mode.

Shelf-trapped edge modes do not need to communicate with the entire basin, but just with the shelf, in order to develop. We demonstrated this for two edge mode examples by extending the deep basin length and showing that the same edge mode occurs at the same dimensional forcing frequency as in the basin with the shorter deep basin length. Thus, resonant edge modes can develop relatively quickly and could be important for coastal-trapped superinertial internal tides in basins of any size, as long as the shelf structure and stratification are tuned to the tide frequency. When considering barotropic shelf-trapped edge modes, the shelf width has to be fairly wide to allow a quarter wave to fit across it. For a shelf that is 100 to 200 m deep, using the shallow water barotropic phase speed and the $M2$ frequency results in barotropic wavelengths of about 1,400 to 1,980 km. This means that for a shelf width to be a quarter of these wavelengths, it would need to be about 350 to 500 km wide. There are not many continental shelves wide enough to meet this requirement, but one

example is the continental shelf off of Argentina. Indeed, studies there have shown large amplitude barotropic $M2$ tides over the shelf and related them to resonance (Glorioso and Flather 1995; Ke and Yankovsky 2010; Rivas 1997). Baroclinic edge modes do not require such a wide shelf to fit a quarter-wave across them, as their wavelengths are smaller than barotropic waves of the same frequency, so it is highly possible that there exists a continental shelf at mid-latitudes that is the appropriate width.

We have seen that some modes are easier to tune in σ-space than others, based on the widths of their resonant peaks. Barotropic modes tend to have wider peaks than baroclinic modes; some modes have wider peaks in basins with wider shelves; and modes with only variability in the x-direction are often wider than those with y-variability, for the basins we have chosen. Much of this is due to the equilibrium tide forcing having little variability in the y-direction and having large wavelength scales, thus more easily exciting modes that have larger wavelengths and no variability in the y-direction. But it is not clear why increasing shelf widths does not increase the widths of each of the modes; why, for example, baroclinic mode three in the one-dimensional flat basin does not have as broad a peak as barotropic mode three in that basin, even though their wavelengths are identical (Fig. 3.2a); or why at times it appears that odd modes have broader peaks than even modes (Fig. 3.2), although this does not hold true consistently.

We hypothesize that in real ocean basins, changes in stratification that cause a basin or shelf to be tuned toward or detuned away from exciting a resonant mode, could explain some observations of temporal and spatial variability in internal tides.

Baroclinic mode eleven in the one-dimensional basin with wide shelves and $\delta_{BC} = 0.70$, has a broad peak elevated above the forcing variance (Fig. 3.2e, eleventh green peak and Fig. 3.6b). Solving for the structure of the off-resonant (but still with amplitudes greater than the forcing) response within the range of σ of the base of the peak shows that while the overall qualitative structure of the mode remains the same (eleven baroclinic zero crossings with one superimposed barotropic zero crossing), there is variability in the relative amplitudes of the barotropic and baroclinic waves and of the shelf and deep basin responses (not shown). When forcing at the lower σ end of the peak base, the response is still dominated by variance on the shelves, but the barotropic wave scale becomes more important relative to the baroclinic one. At the higher σ end of the peak base, the response is no longer dominated by shelf variance, but is now of similar amplitude in the deep basin and shelves. Thus, perhaps slight internal tide structural variability like this could be observed as a basin is tuned toward and away from resonant baroclinic basin mode or shelf-trapped edge mode excitation as stratification changes. For example, perhaps the changes of the phasing between interfering eastbound and westbound alongshore propagating internal tides that sometimes result in the nearly standing pattern observed in Alford et al. (2006) due to ambient stratification changes altering the waves' group velocity and thus arrival times, could be viewed as a shelf region being tuned toward and away from a resonant response that would result in a standing wave.

Many questions remain about how applicable resonant mode excitation is for generating large-amplitude barotropic and baroclinic tides in the real ocean. How much can stratification vary and still allow a mode to develop, and what kind of temporal

intermittency timescales are expected by the tuning/detuning of modes as stratification changes? What would alongshore variability in shelf structure do to basin and edge mode structures and predilection for mode excitation? How much do interactions with other physical processes impact mode excitation? Stratification strength and shelf structure could be varied in the linear model developed here, to see how peak widths change in stratification-space and to explore the spatial variation in mode structures that result from alongshore varying shelves. Some of these questions could perhaps be addressed by using a numerical model that allows for observing the temporal evolution of modes and for including other physical processes, such as the Regional Ocean Modeling System (ROMS). The insight gained from our linear analysis could be used help to set up a basin in ROMS that would generate a resonant mode, but it could still be challenging to find a particular mode in ROMS. Nonetheless, it seems likely that in small enough basins, resonant excitation of basin mode internal tides could be an important source of baroclinic variability, and in any basin, baroclinic edge-mode excitation could be an important source of shelf-trapped superinertial internal tides.

3.8 Acknowledgements

We thank Kraig Winters for the many discussions we had about this research. We thank our funding provider, the National Science Foundation (grants OCE 1155799 and OCE 1756752).

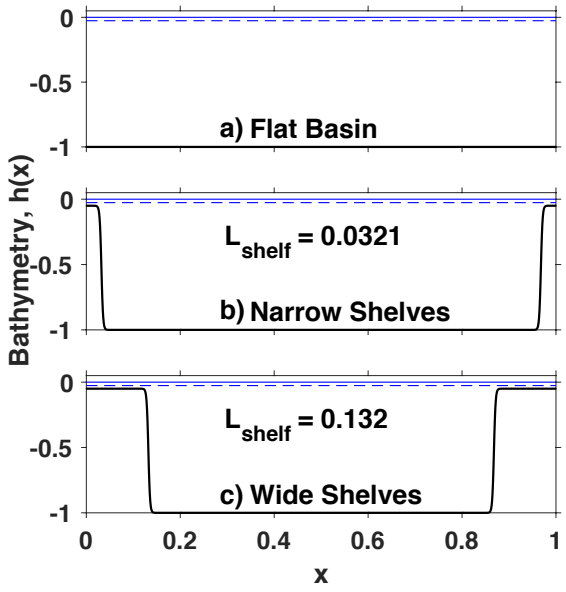

Figure 3.1: The three non-dimensional basins used in the one-dimensional problem with no rotation. They have identical, two-layered stratification (the solid blue line is the sea surface and the dashed blue line is the interface, at $z = -0.02625$). Panel (a) is a deep basin with flat bathymetry, (b) has narrow continental shelves, and (c) has wide continental shelves. Shelf depths are identical, with $h_s = 0.05$.

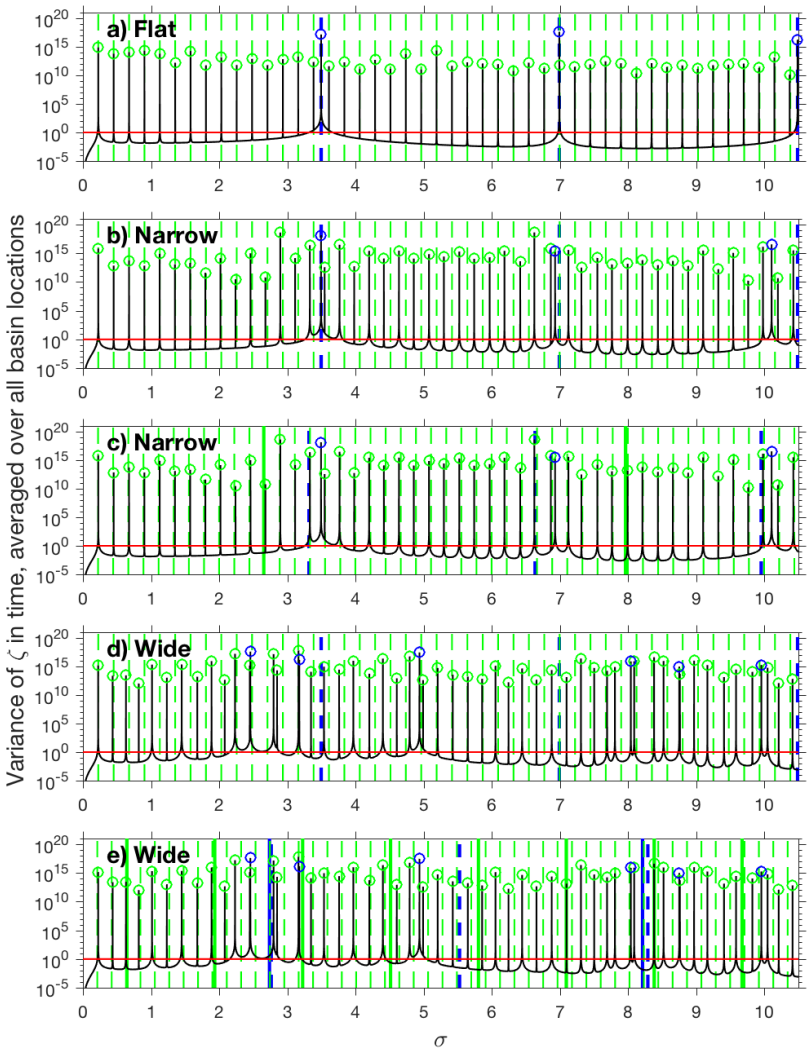

Figure 3.2: Variance of interface motions (ζ) averaged over the basin and normalized by forcing variance (black lines) from solutions to the forced one-dimensional problem versus σ, for the (a) flat basin, (b) and (c) narrow shelf basin, and (d) and (e) wide shelf basin, all with $h1 = 0.02625$, $\delta_{BC} = 0.70$, and $\rho = 0.25$. Blue circles denote peaks of barotropic modes; green circles denote peaks of baroclinic modes. The horizontal red line in all panels is the normalized forcing variance. In panels (a), (b), and (d), vertical dashed lines show predicted σ_j for barotropic (blue) and baroclinic (green) modes (equation 3.17). In panels (c) and (e), vertical dashed lines show predicted σ_n for barotropic (blue) and baroclinic (green) modes (equation 3.21). Vertical solid lines in panels (c) and (e) are values of σ_m (equation 3.22), which show when multiples of quarter barotropic (blue) and baroclinic (green) wavelengths fit across the shelf width. Vertical solid blue lines appear only in panel (e): just to the left of the first and third vertical blue dashed lines.

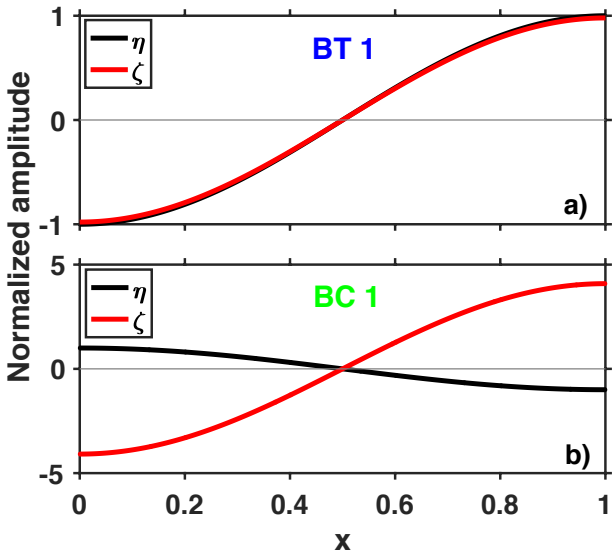

Figure 3.3: Mode structures of the sea surface, η, (black) and interface, ζ, (red) for the flat basin. Amplitudes are normalized by the sea surface. (a) Barotropic mode 1 ($\sigma = 3.4959$). (b) Baroclinic mode 1 ($\sigma = 0.2257$). In panel (a), the red line covers most of the black line.

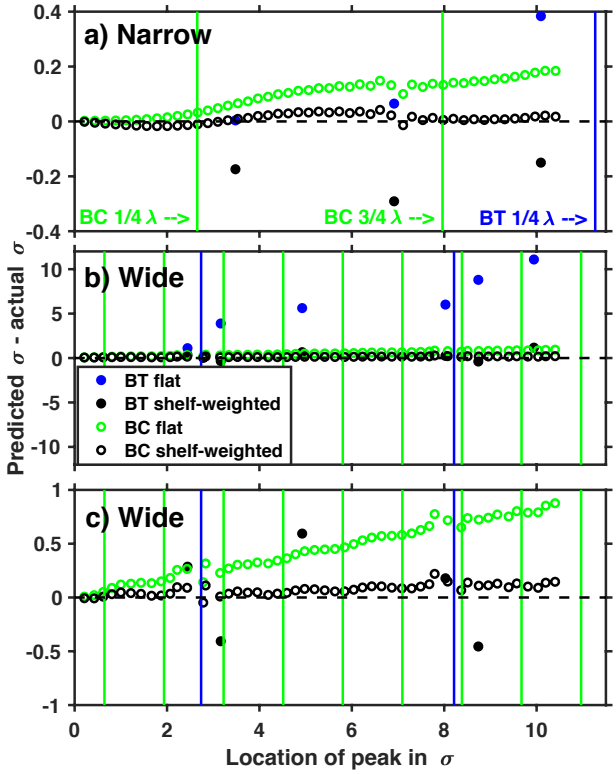

Figure 3.4: Predicted σ minus the actual location of each resonant peak in σ-space, comparing predictions for σ_j using the flat basin analytical equation (equation 3.17) and σ_n using the shelf-weighted estimate (equation 3.21). Values closer to the black dashed zero-line indicate better predictions. The legend in panel (b) applies to all panels. (a) Narrow shelves; (b) wide shelves; (c) wide shelves, zoomed in to better show baroclinic mode results. Vertical solid lines are values of σ_m (equation 3.22), indicating when multiples of quarter barotropic (blue) and baroclinic (green) wavelengths fit across the shelf width. Note that near the values of $\sigma_{m=1}$, where 1/4-wavelength (baroclinic or barotropic) fits across the shelf width, the flat basin analytical σ_j (blue and green circles) start to stray from the actual peak locations, and the shelf-weighted predictions for σ_n (black circles) become better estimates.

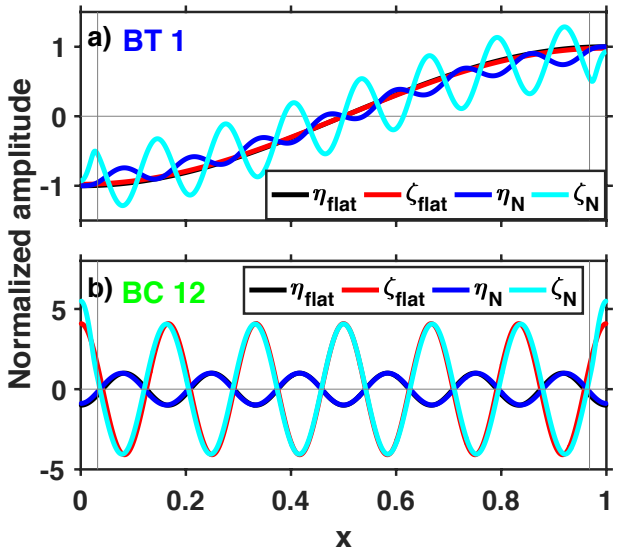

Figure 3.5: Mode structures of the sea surface, η, (blue) and interface, ζ, (cyan) for the basin with narrow shelves, plotted over those for the flat basin (black and red). Vertical grey lines indicate the midpoint of the continental slope (the shelf width). Amplitudes are normalized by the sea surface. (a) Barotropic mode 1, with coupled smaller scale baroclinic waves across the basin ($\sigma = 3.4944$). (b) Baroclinic mode 12 ($\sigma = 2.6780$). In panel (b), the blue line is on top of the black line.

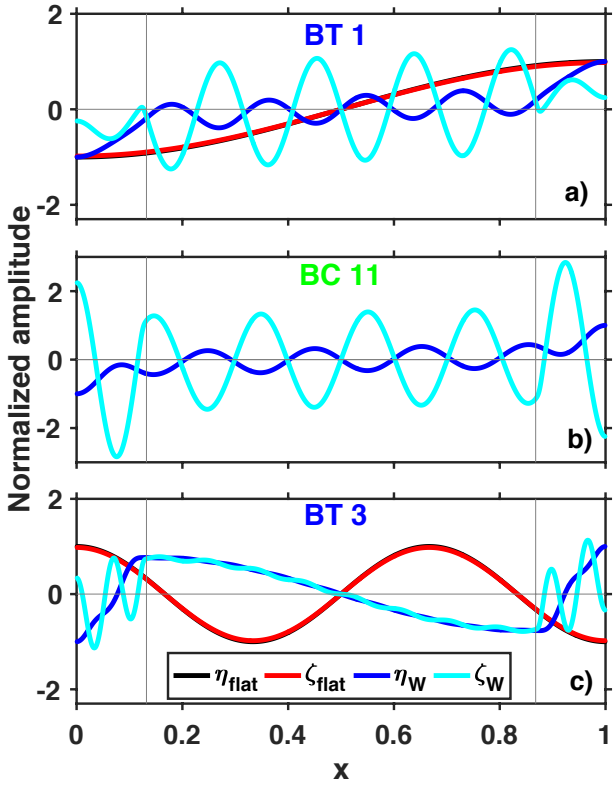

Figure 3.6: Mode structures of the sea surface, η, (blue) and interface, ζ, (cyan) for the basin with wide shelves, plotted over those for the flat basin (black and red, panels (a) and (c)). Vertical grey lines indicate the midpoint of the continental slope (the shelf width). Amplitudes are normalized by the sea surface. (a) Barotropic mode 1, with coupled smaller scale baroclinic waves across the basin ($\sigma = 2.4573$). (b) Baroclinic mode 11, with coupled larger scale barotropic wave across the basin ($\sigma = 2.2318$). (c) Barotropic mode 3, with coupled smaller scale baroclinic waves across the basin ($\sigma = 4.9387$). The legend in panel (c) applies to all panels, except flat basin results are not plotted in panel (b). In panels (a) and (c), the red lines are on top of the black lines.

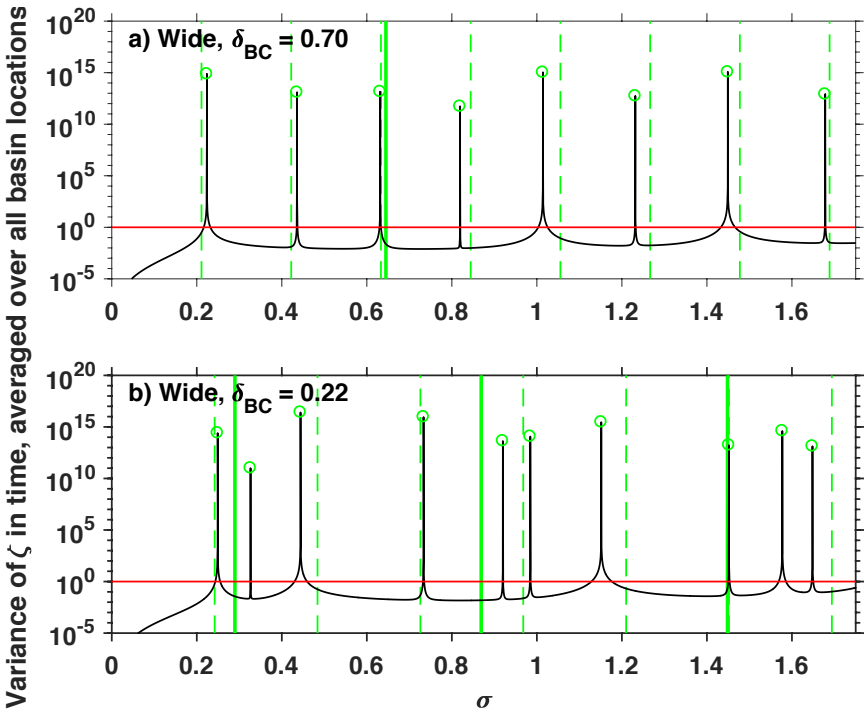

Figure 3.7: Variance of interface motions (ζ) averaged over the basin and normalized by forcing variance (black lines) from solutions to the forced one-dimensional problem versus σ, for the (a) wide shelf basin with $\delta_{BC} = 0.70$ and (b) the wide shelf basin with $\delta_{BC} = 0.22$. Green circles denote peaks of baroclinic modes. The horizontal red line in both panels is the normalized forcing variance. Green vertical dashed lines show predicted σ_n for baroclinic basin modes (equation 3.21) and green vertical solid lines are σ_m for baroclinic shelf-amplified basin modes (equation 3.22). For $\delta_{BC} = 0.70$, resonant mode peaks only occur for each basin mode, σ_n, but for $\delta_{BC} = 0.22$, resonant mode peaks occur for each basin mode, σ_n, and for each shelf-amplified basin mode, σ_m Note that the third solid vertical green line in panel (b) is covering a green vertical dashed line.

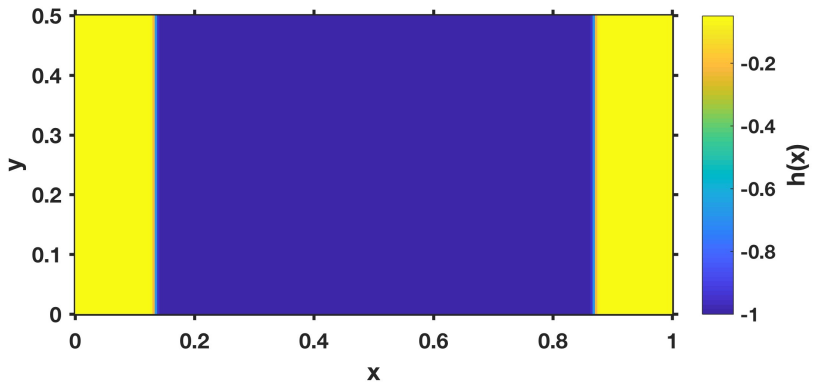

Figure 3.8: Plan view of the bathymetric structure of the non-dimensional basin for the two-dimensional problem with wide shelves. The bathymetry varies only in the x-direction, and its x-structure is the same as in the one-dimensional problem with wide shelves (Fig. 3.1c).

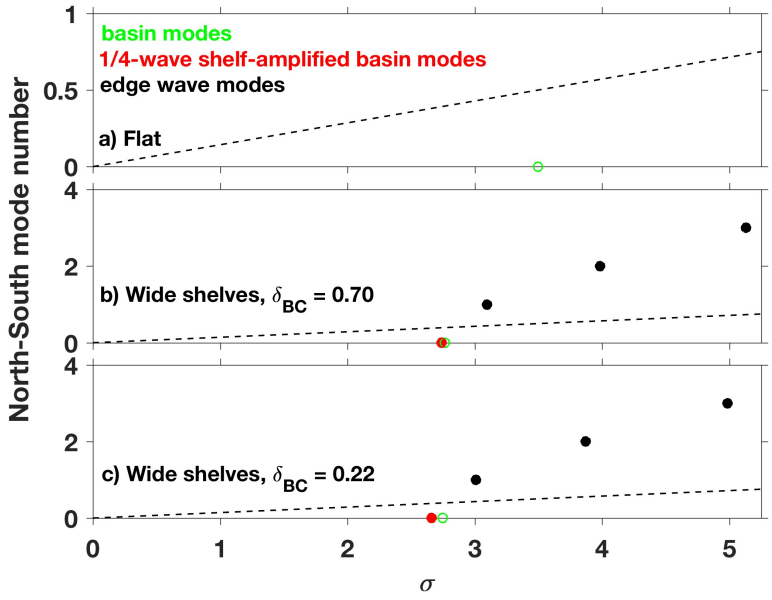

Figure 3.9: Predicted coupled barotropic modes for the (a) flat basin; (b) basin with wide shelves; and (c) basin with wide shelves and deeper surface layer. Above the black dashed line, the trapping condition is met ($\sigma < c_d \frac{q\pi}{L_y}$).

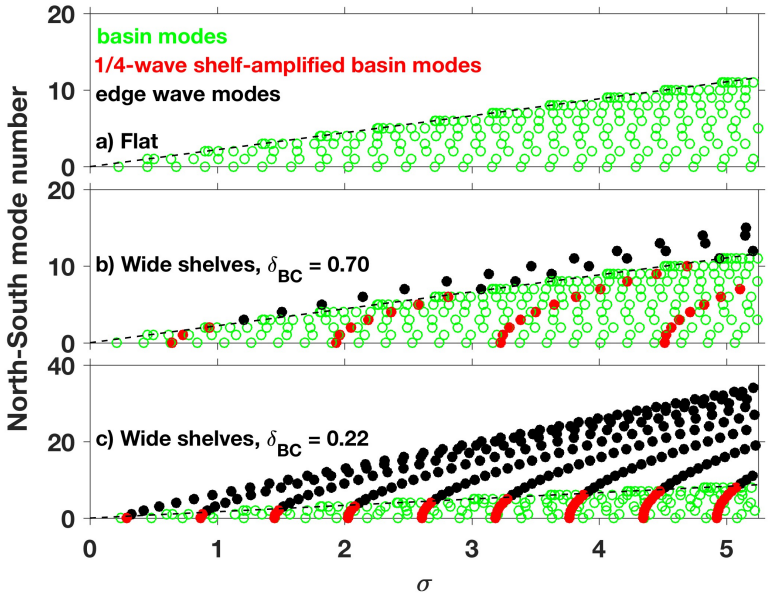

Figure 3.10: Predicted coupled baroclinic modes for the (a) flat basin; (b) basin with wide shelves; and (c) basin with wide shelves and deeper surface layer. Above the black dashed line, the trapping condition is met ($\sigma < c_d \frac{q\pi}{L_y}$).

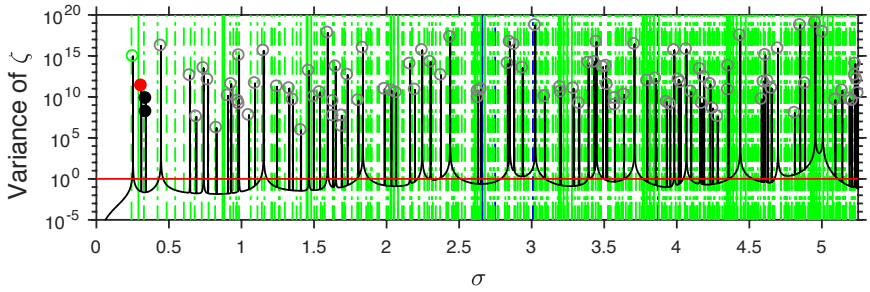

Figure 3.11: Variance of interface motions (ζ) averaged over the basin and normalized by forcing variance (black lines) from solutions to the forced two-dimensional problem versus σ, for the wide shelf basin with $\delta_{BC} = 0.22$ and $\rho = 0.25$. Several predicted modes have not had their peaks resolved. The green circle denotes the peak for the first baroclinic basin mode, $x1$ and $y0$; the red circle denotes the peak for the first baroclinic shelf-amplified basin mode, which yields $x2$ and $y0$; and the two black circles denote the peaks associated with the first baroclinic shelf-trapped edge mode, which fits a quarter wave across the shelves and is mode 1 along the shelves. The grey circles mark the other peaks without identifying their mode types. The horizontal red line is the normalized forcing variance. Vertical lines show the various predicted modes, but there are so many (415) that it is not possible to discern each line. Vertical dashed lines are predicted basin modes $\sigma_{n,p}$, for barotropic (blue) and baroclinic (green) modes (equation 3.31). Vertical solid lines are values of $\sigma_{m,q}$ (equation 3.28) for $\sigma > c_d \frac{q\pi}{L_y}$, which show predicted shelf-amplified barotropic (blue) and baroclinic (green) basin modes. Vertical dash-dotted lines show predicted shelf-trapped edge barotropic (blue) and baroclinic (green) modes (equation 3.28 for $\sigma < c_d \frac{q\pi}{L_y}$).

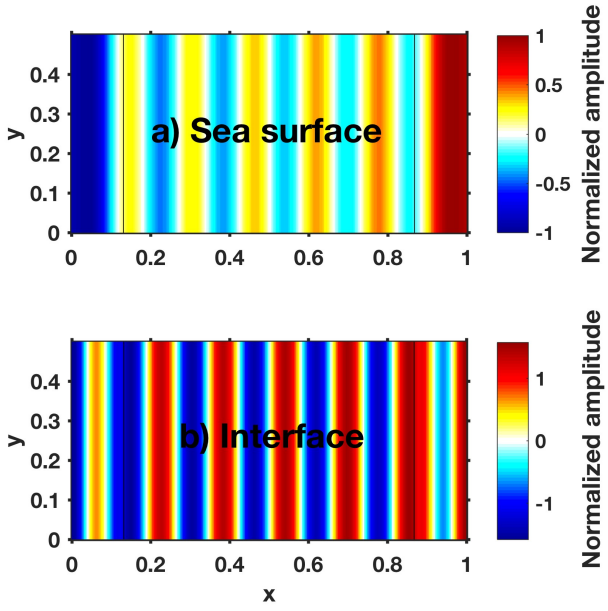

Figure 3.12: Barotropic shelf-amplified basin mode for the basin with wide shelves and $\delta_{BC} = 0.70$: mode one in the x-direction, mode zero in the y-direction ($\sigma = 2.8697$). Smaller scale baroclinic waves across the basin are coupled with the barotropic mode. Normalized amplitudes (relative to sea surface) for the (a) sea surface and (b) interface. Vertical grey lines denote shelf width.

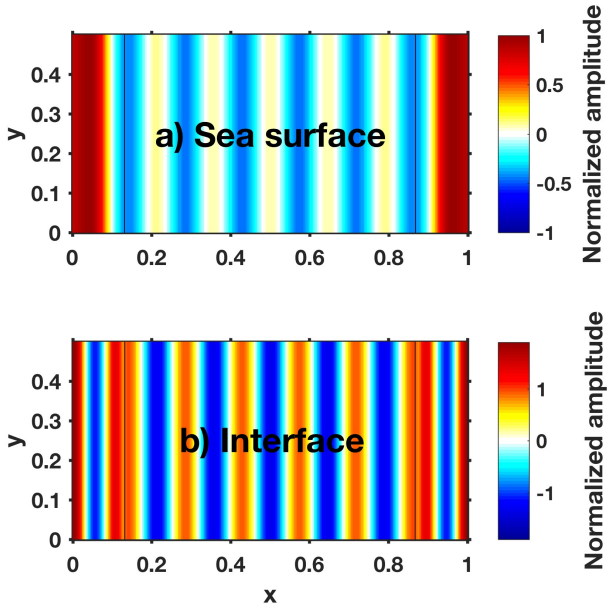

Figure 3.13: Barotropic basin mode for the basin with wide shelves and $\delta_{BC} = 0.70$: mode two in the x-direction (which has its two crests over the shelves and its trough throughout the deep basin), mode zero in the y-direction ($\sigma = 3.1261$). Smaller scale baroclinic waves across the basin are coupled with the barotropic mode. Normalized amplitudes (relative to sea surface) for the (a) sea surface and (b) interface. Vertical grey lines denote shelf width.

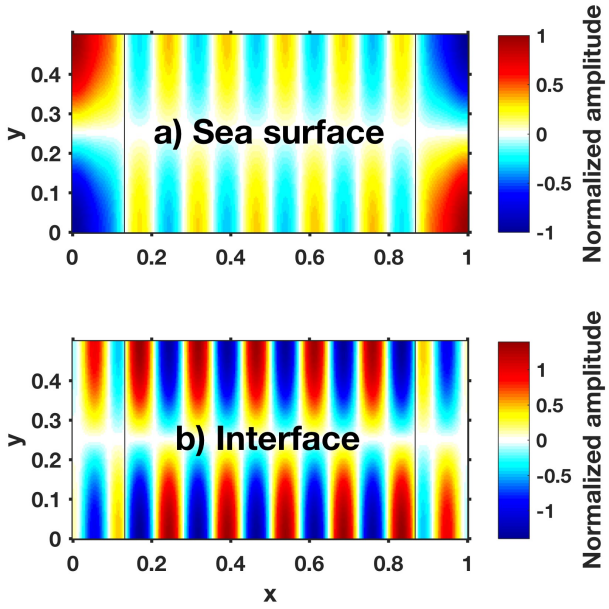

Figure 3.14: Barotropic shelf-trapped edge mode for the basin with wide shelves and $\delta_{BC} = 0.70$: 1/4-wavelength across the shelf, mode one in the y-direction ($\sigma = 3.2545$). Smaller scale baroclinic waves across the basin are coupled with the barotropic edge mode. Normalized amplitudes (relative to sea surface) for the (a) sea surface and (b) interface. Vertical grey lines denote shelf width. Here, the signs of the sea surface are opposite on the opposite shelf, but note that there is another peak of the same structure, but with signs that are symmetric on the opposite shelves.

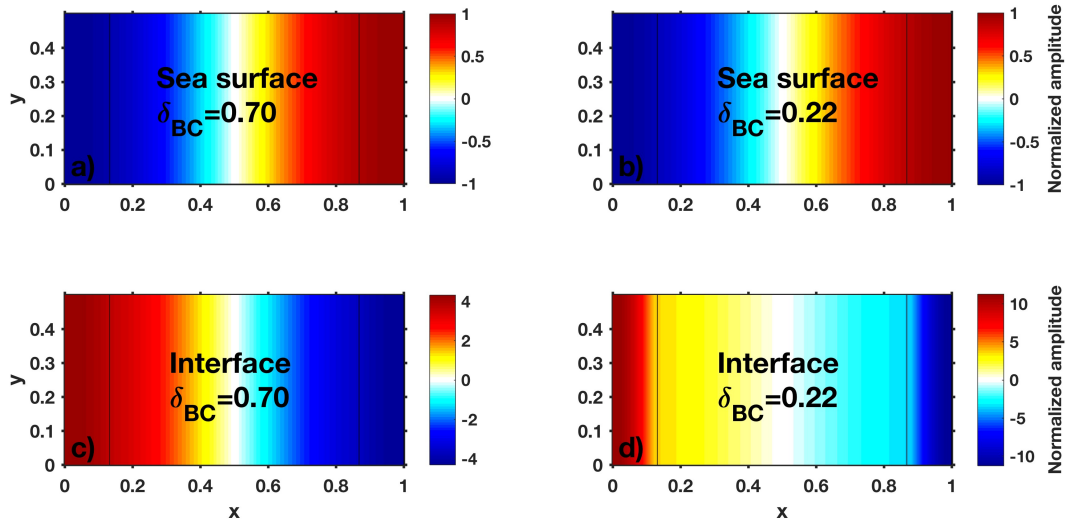

Figure 3.15: Baroclinic basin mode for the basin with wide shelves, $\delta_{BC} = 0.70$ ($\sigma = 0.2246$) versus $\delta_{BC} = 0.22$ ($\sigma = 0.2521$): mode one in the x-direction, mode zero in the y-direction. Normalized amplitudes (relative to sea surface) for the (a) and (b) sea surface and (c) and (d) interface. Vertical grey lines denote shelf width.

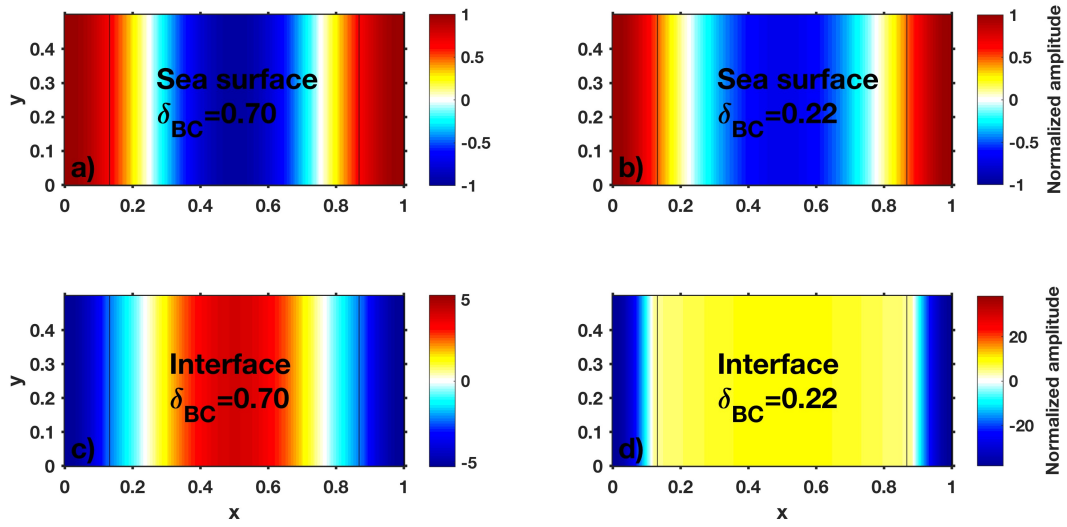

Figure 3.16: Baroclinic basin mode for the basin with wide shelves, $\delta_{BC} = 0.70$ ($\sigma = 0.4337$) versus baroclinic shelf-amplified basin mode for $\delta_{BC} = 0.22$ ($\sigma = 0.3095$): mode two in the x-direction, mode zero in the y-direction. Normalized amplitudes (relative to sea surface) for the (a) and (b) sea surface and (c) and (d) interface. Vertical grey lines denote shelf width.

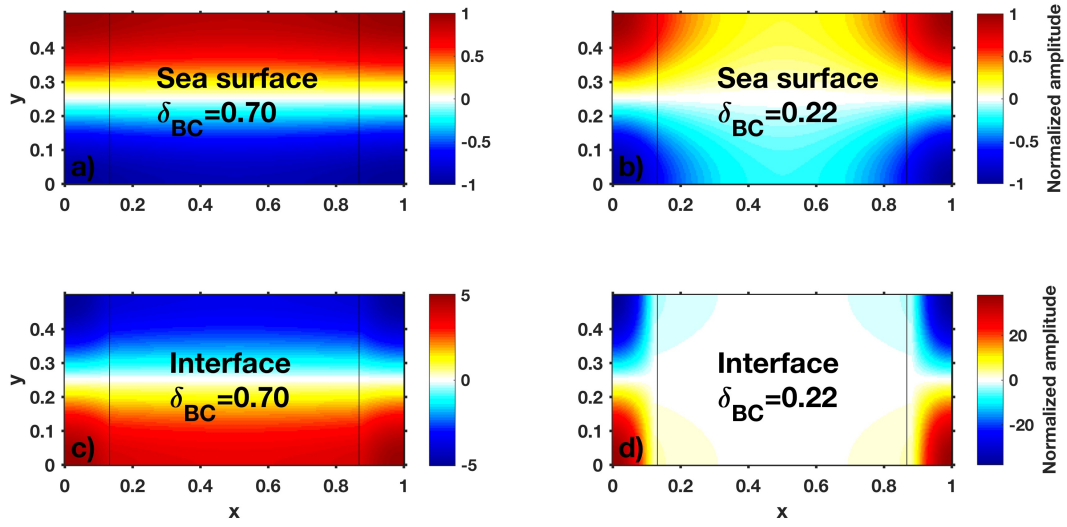

Figure 3.17: Baroclinic basin mode for the basin with wide shelves and $\delta_{BC} = 0.70$ ($\sigma = 0.4439$, mode zero in the x-direction and mode 1 in the y-direction) versus shelf-trapped edge mode for the basin with wide shelves and $\delta_{BC} = 0.22$ ($\sigma = 0.3407$, 1/4-wavelength across the shelf, mode one in the y-direction). Normalized amplitudes (relative to sea surface) for the (a) and (b) sea surface and (c) and (d) interface. Vertical grey lines denote shelf width. Here, for the edge mode in the basin with $\delta_{BC} = 0.22$, the signs of the sea surface and interface are symmetric on the opposite shelf, but note that there is another peak of the same structure, but with signs that are opposite on the opposite shelves.

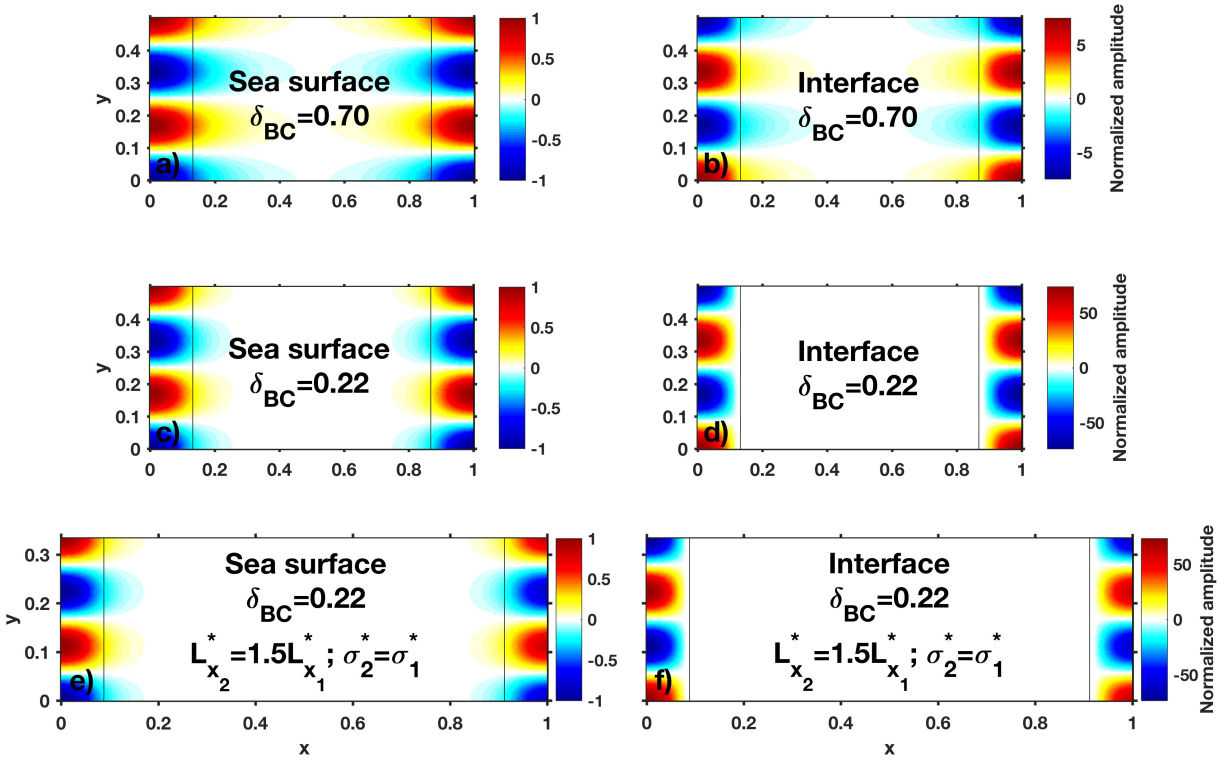

Figure 3.18: Baroclinic edge mode for the basin with wide shelves and $\delta_{BC} = 0.70$ ($\sigma = 1.1631$) versus $\delta_{BC} = 0.22$ ($\sigma = 0.5572$), and for the same basin with $\delta_{BC} = 0.22$, but with an extended deep basin that results in a total basin length that is 50% larger ($\sigma = 0.8362$) (1/4-wavelength across the shelf, mode three in the y-direction). Normalized amplitudes (relative to sea surface) for the sea surface (a, c, e) and interface (b, d, f). Vertical grey lines denote shelf width, which is identical in all basins. Note that the edge mode is more confined to the shelves in the basins with $\delta_{BC} = 0.22$. The basin with the extended deep basin (e, f) shows that the edge mode does not care about the deep basin structure: the same edge mode occurs at the same dimensional frequency as in the basin without the extended deep section.

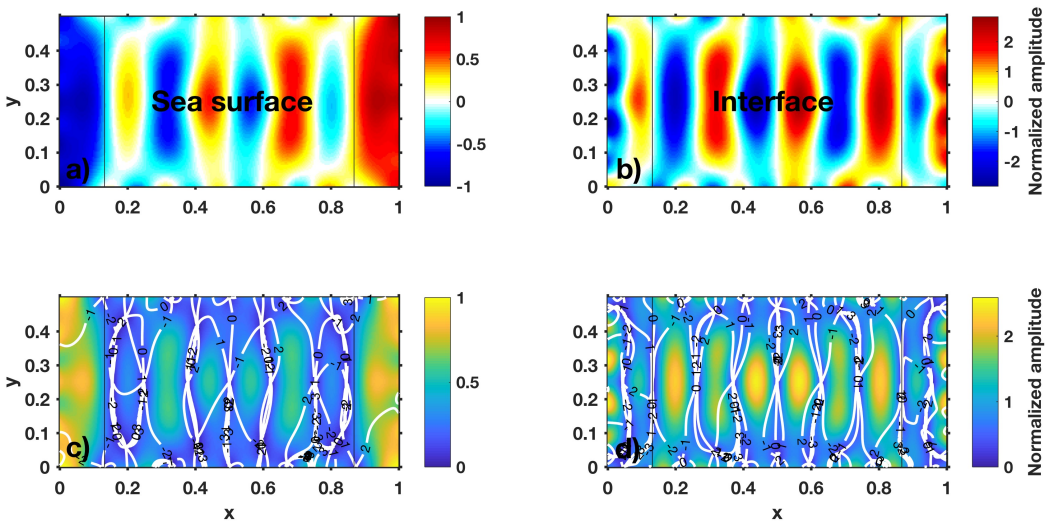

Figure 3.19: Possibly barotropic basin mode for the basin with wide shelves, on an f-plane, with $\delta_{BC} = 0.70$, with coupled smaller scale baroclinic waves across the basin ($\sigma = 2.8339$). The barotropic component corresponds to the barotropic shelf-amplified basin mode in the non-rotating basin that is mode one in the x-direction and mode zero in the y-direction (Fig. 3.12). Normalized displacement (relative to sea surface) for the (a) sea surface and (b) interface; and normalized amplitudes (relative to sea surface, colors) and phases (white contours, propagation direction is toward lower phase) for the (c) sea surface and (d) interface. Vertical grey lines denote shelf width. The barotropic shelf component propagates phase along the shelves, cyclonically, and the sea surface has its greatest amplitudes over the shelves, associated with that motion.

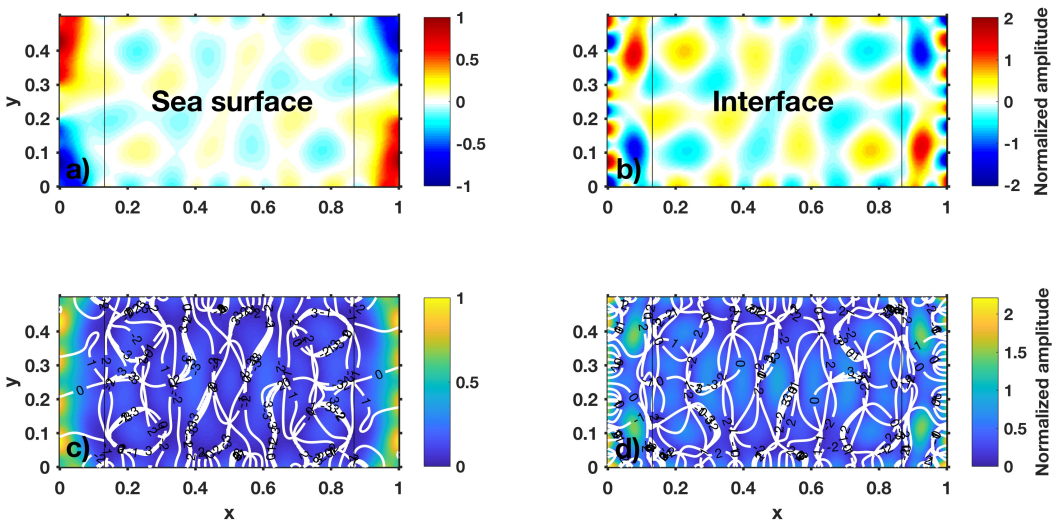

Figure 3.20: Possibly barotropic basin mode for the basin with wide shelves, on an f-plane, with $\delta_{BC} = 0.70$, with coupled smaller scale baroclinic waves throughout the basin ($\sigma = 3.3603$). The barotropic component corresponds to the barotropic edge mode in the non-rotating basin that has 1/4-wavelength across the shelf and is mode one in the y-direction (Fig. 3.14). Normalized displacement (relative to sea surface) for the (a) sea surface and (b) interface; and normalized amplitudes (relative to sea surface, colors) and phases (white contours, propagation direction is toward lower phase) for the (c) sea surface and (d) interface. Vertical grey lines denote shelf width. The barotropic shelf component propagates phase along the shelves, cyclonically, and the sea surface has its greatest amplitudes over the shelves, associated with that motion.

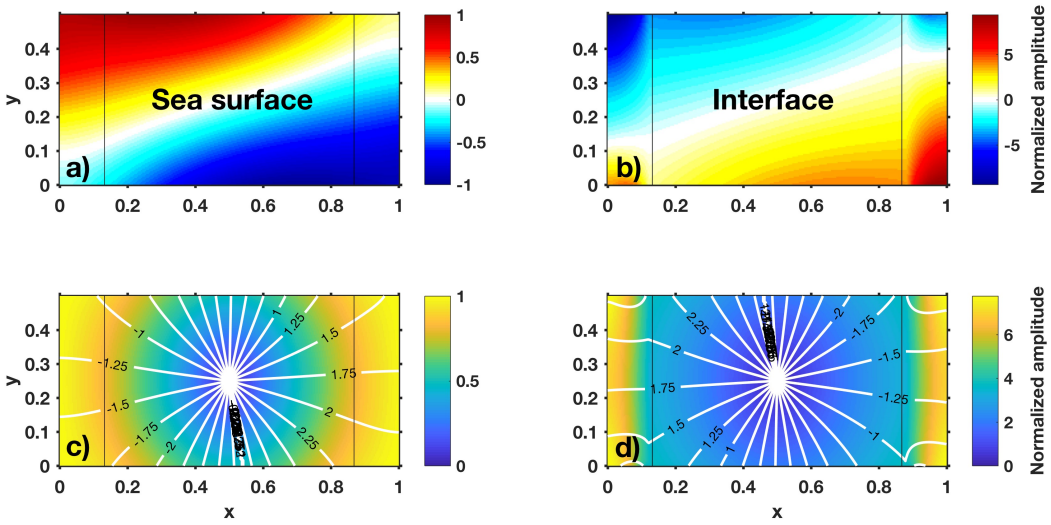

Figure 3.21: Baroclinic basin mode for the basin with wide shelves, on an f-plane, with $\delta_{BC} = 0.22$ ($\sigma = 0.2696$). This corresponds to the baroclinic basin mode in the non-rotating basin that is mode one in the x-direction and mode zero in the y-direction (Fig. 3.15b and 3.15d). Normalized displacement (relative to sea surface) for the (a) sea surface and (b) interface; and normalized amplitudes (relative to sea surface, colors) and phases (white contours, propagation direction is toward lower phase) for the (c) sea surface and (d) interface. Vertical grey lines denote shelf width. The mode propagates around a central cyclonic amphidrome, with maximum amplitudes in the interface over the shelf.

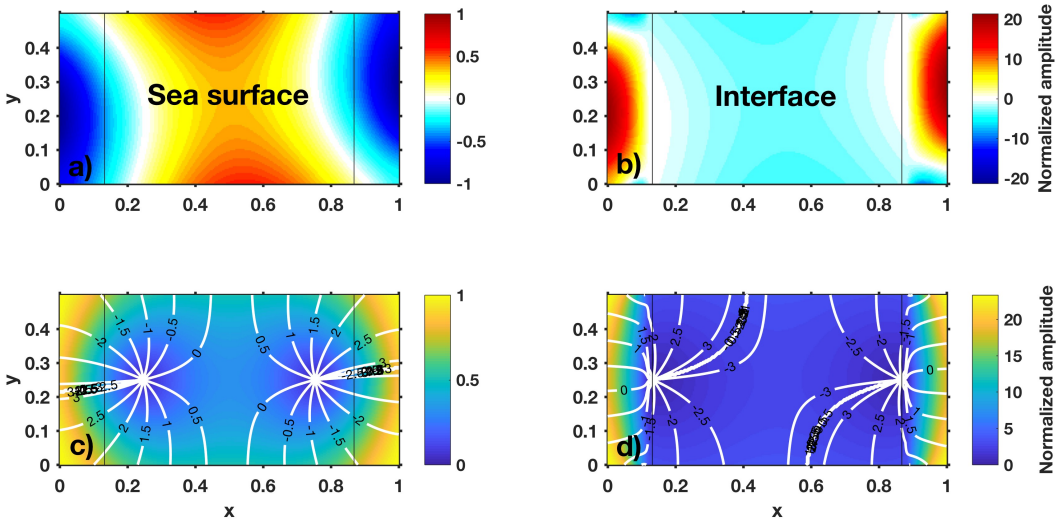

Figure 3.22: Baroclinic shelf-amplified basin mode for the basin with wide shelves, on an f-plane, with $\delta_{BC} = 0.22$ ($\sigma = 0.3579$). This corresponds to the baroclinic shelf-amplified basin mode in the non-rotating basin that is mode two in the x-direction and mode zero in the y-direction (Fig. 3.16b and 3.16d). Normalized displacement (relative to sea surface) for the (a) sea surface and (b) interface; and normalized amplitudes (relative to sea surface, colors) and phases (white contours, propagation direction is toward lower phase) for the (c) sea surface and (d) interface. Vertical grey lines denote shelf width. The mode propagates around two cyclonic amphidromes, with maximum amplitudes in the interface over the shelf.

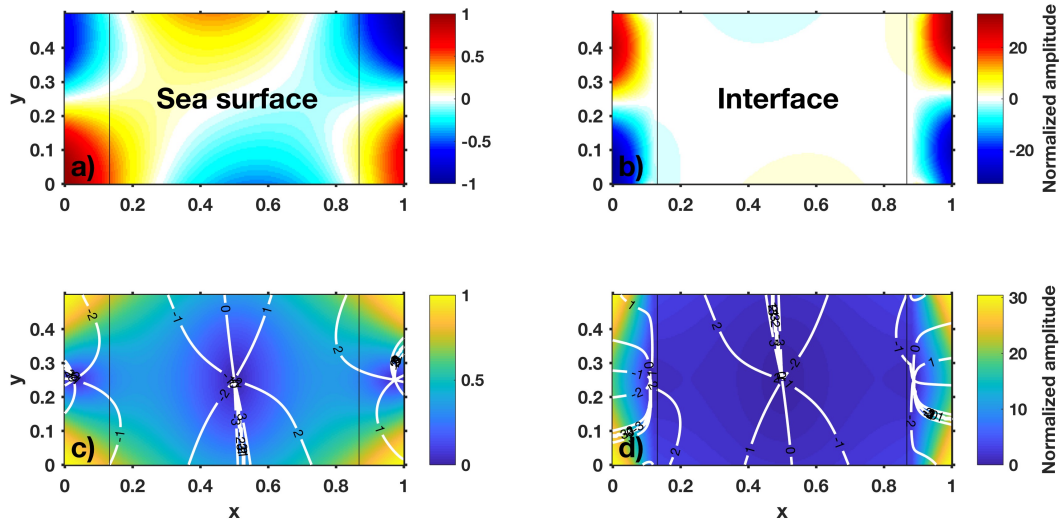

Figure 3.23: Baroclinic shelf-trapped edge mode for the basin with wide shelves, on an f-plane, with $\delta_{BC} = 0.22$ ($\sigma = 0.3816$). This corresponds to the baroclinic edge mode in the non-rotating basin that is 1/4-wavelength across the shelf and mode one in the y-direction (Fig. 3.17b and 3.17d). Normalized displacement (relative to sea surface) for the (a) sea surface and (b) interface; and normalized amplitudes (relative to sea surface, colors) and phases (white contours, propagation direction is toward lower phase) for the (c) sea surface and (d) interface. Vertical grey lines denote shelf width. Interface amplitudes decay greatly into the deep basin, with cyclonic alongshore propagation on the shelves and small-amplitude cyclonic propagation in the deep basin.

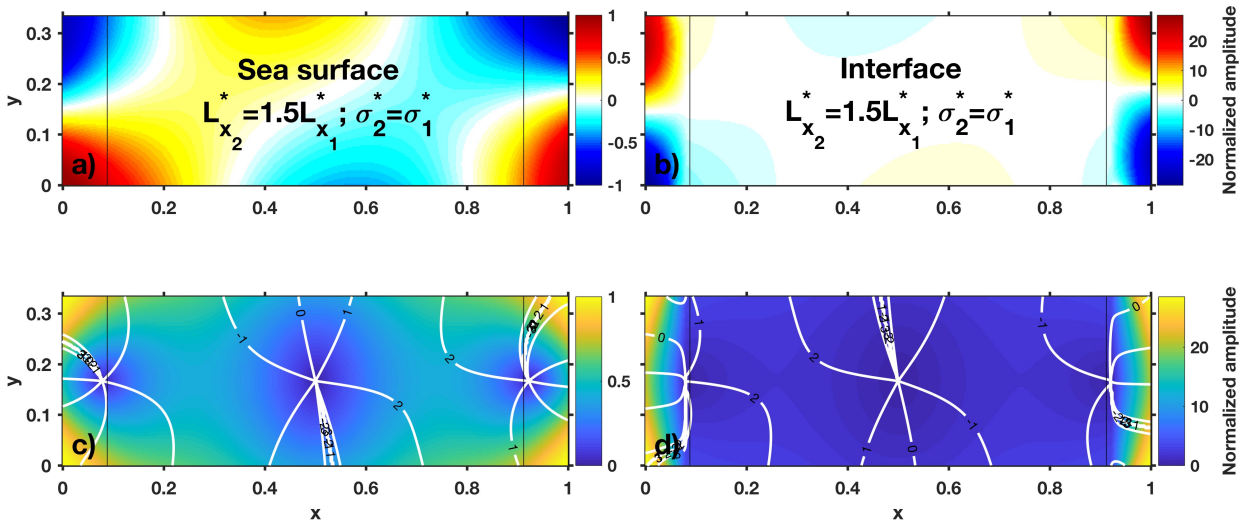

Figure 3.24: Baroclinic shelf-trapped edge mode for the basin with wide shelves, on an f-plane, with $\delta_{BC} = 0.22$, with the deep basin extended so that the total basin length that is 50% larger ($\sigma = 0.5565$). This is the same edge mode as in the regular basin length in Fig. 3.23, and is forced at the same dimensional frequency. This corresponds to the baroclinic edge mode in the non-rotating basin that is 1/4-wavelength across the shelf and mode one in the y-direction (Fig. 3.17b and 3.17d). Normalized displacement (relative to sea surface) for the (a) sea surface and (b) interface; and normalized amplitudes (relative to sea surface, colors) and phases (white contours, propagation direction is toward lower phase) for the (c) sea surface and (d) interface. Vertical grey lines denote shelf width. Interface amplitudes decay greatly into the deep basin, with cyclonic alongshore propagation on the shelves and small-amplitude cyclonic propagation in the deep basin.

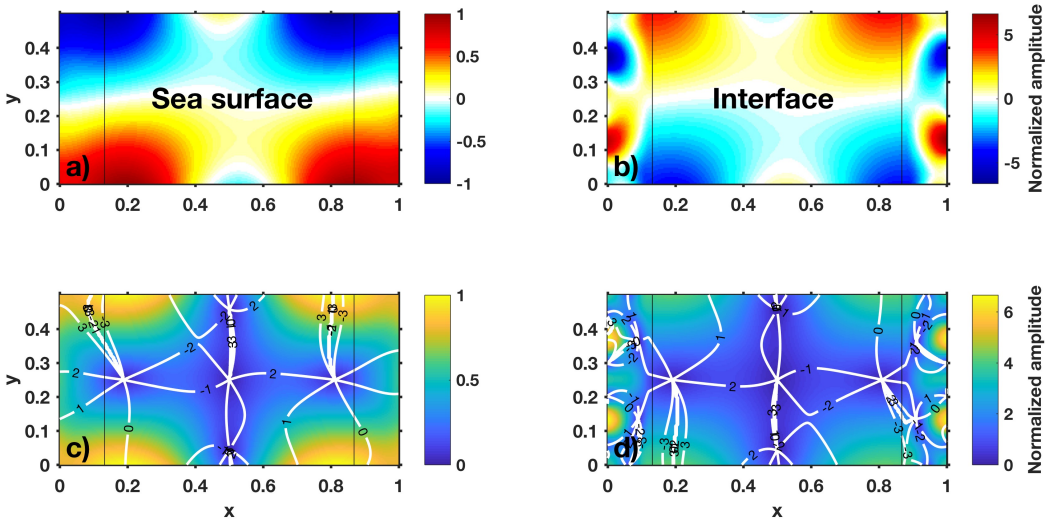

Figure 3.25: Baroclinic mode for the basin with wide shelves, on an f-plane, with $\delta_{BC} = 0.22$ ($\sigma = 0.9085$). Normalized displacement (relative to sea surface) for the (a) sea surface and (b) interface; and normalized amplitudes (relative to sea surface, colors) and phases (white contours, propagation direction is toward lower phase) for the (c) sea surface and (d) interface. Vertical grey lines denote shelf width.

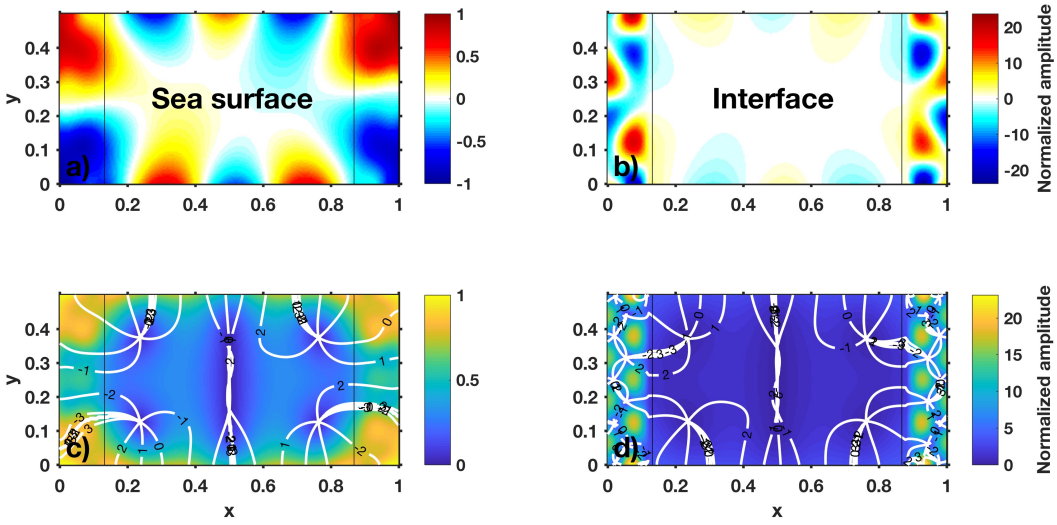

Figure 3.26: Baroclinic mode for the basin with wide shelves, on an f-plane, with $\delta_{BC} = 0.22$ ($\sigma = 1.3883$). Normalized displacement (relative to sea surface) for the (a) sea surface and (b) interface; and normalized amplitudes (relative to sea surface, colors) and phases (white contours, propagation direction is toward lower phase) for the (c) sea surface and (d) interface. Vertical grey lines denote shelf width.

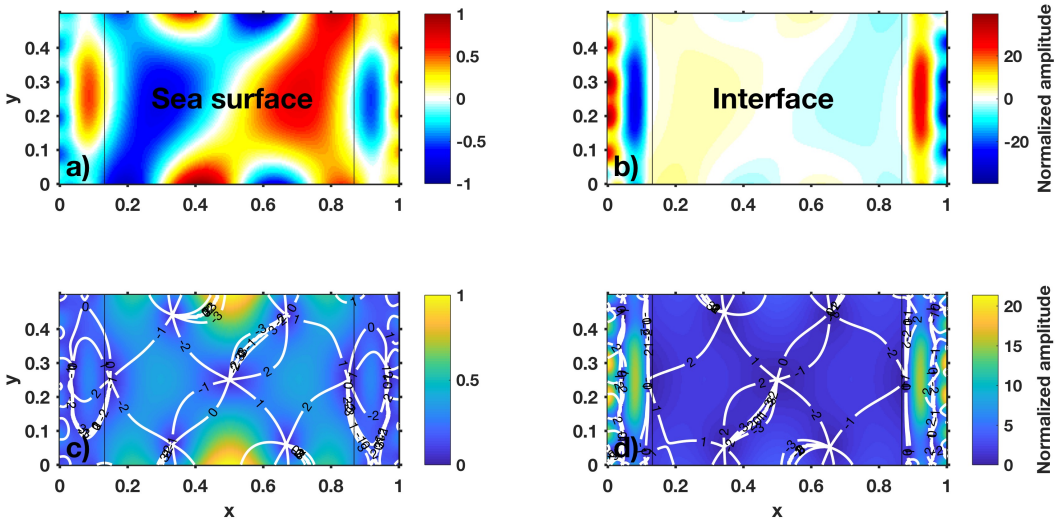

Figure 3.27: Baroclinic mode for the basin with wide shelves, on an f-plane, with $\delta_{BC} = 0.22$ ($\sigma = 1.4337$). Normalized displacement (relative to sea surface) for the (a) sea surface and (b) interface; and normalized amplitudes (relative to sea surface, colors) and phases (white contours, propagation direction is toward lower phase) for the (c) sea surface and (d) interface. Vertical grey lines denote shelf width.

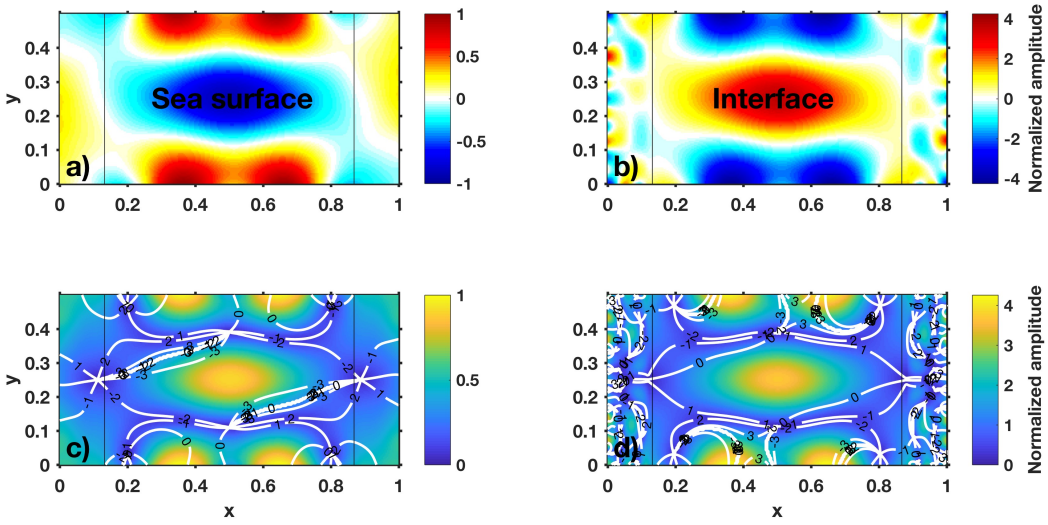

Figure 3.28: Baroclinic mode for the basin with wide shelves, on an f-plane, with $\delta_{BC} = 0.22$ ($\sigma = 1.8681$). Normalized displacement (relative to sea surface) for the (a) sea surface and (b) interface; and normalized amplitudes (relative to sea surface, colors) and phases (white contours, propagation direction is toward lower phase) for the (c) sea surface and (d) interface. Vertical grey lines denote shelf width.

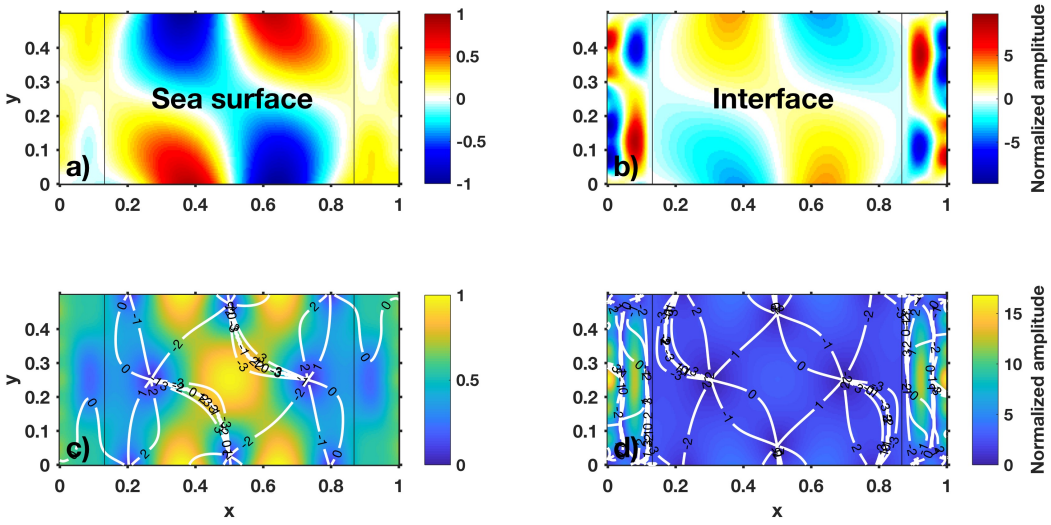

Figure 3.29: Baroclinic mode for the basin with wide shelves, on an f-plane, with $\delta_{BC} = 0.22$ ($\sigma = 1.5322$). Normalized displacement (relative to sea surface) for the (a) sea surface and (b) interface; and normalized amplitudes (relative to sea surface, colors) and phases (white contours, propagation direction is toward lower phase) for the (c) sea surface and (d) interface. Vertical grey lines denote shelf width.

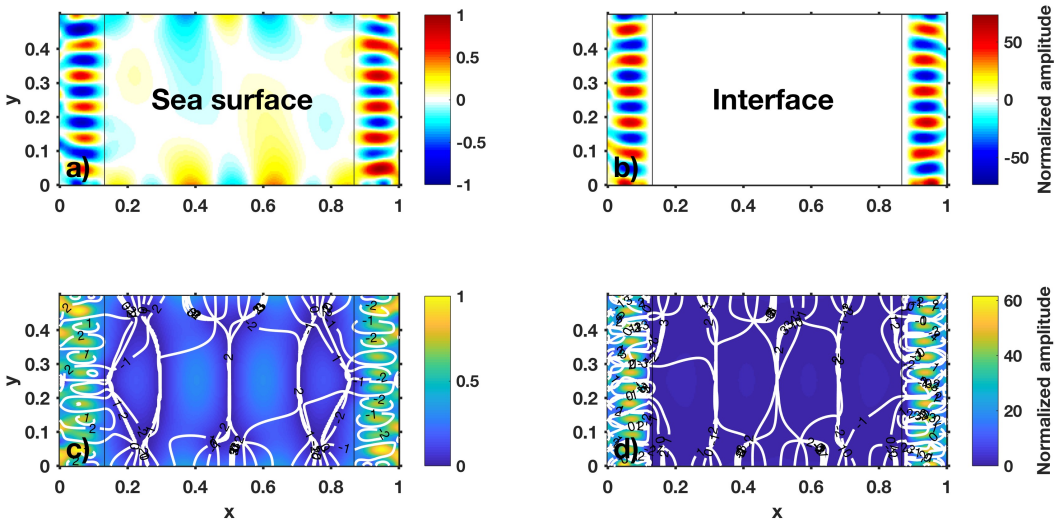

Figure 3.30: Baroclinic shelf-trapped edge mode for the basin with wide shelves, on an f-plane, with $\delta_{BC} = 0.22$ ($\sigma = 2.6544$). Normalized displacement (relative to sea surface) for the (a) sea surface and (b) interface; and normalized amplitudes (relative to sea surface, colors) and phases (white contours, propagation direction is toward lower phase) for the (c) sea surface and (d) interface. Vertical grey lines denote shelf width. Interface amplitudes decay greatly into the deep basin.

Chapter 4: Effects of alongshore shelf width variability on coupled barotropic-baroclinic resonant modes: a potential source of large-amplitude coastal-trapped superinertial internal tides

Jennifer Thomas, James Lerczak, and Clinton Winant

To be submitted to Journal of Physical Oceanography

45 Beacon Street

Boston, MA 02108-3693

USA

4.1 Abstract

This study explores the effects of alongshore shelf width variability on coupled barotropic-baroclinic resonant modes, in order to understand when resonant mode excitation can result in large-amplitude superinertial internal tides with alongshelf dependence on the continental shelf. In nature, continental shelves are not uniform alongshore, so these simulations are performed to understand what might happen with resonant modes in the real ocean, building on the knowledge gained by studying basins with alongshore uniform shelves in thesis Chapter 3. A shelf is on the western boundary of an idealized basin, and is narrow to the north and south, with a wide middle section. Some resonant modes have large amplitudes isolated to the wide section of the shelf, some have large amplitudes along the entire shelf, but more confined to the narrow width extent, and some have large amplitudes distributed over the entire shelf. Phase on the shelf can propagate in either direction, alongshelf or rotating around complicated amphidrome structures that result in various patterns over the shelf. Along- and across-shelf wavelength scales in a resonant response can be different for the narrow versus wide sections of shelf, as can sense of phase propagation. These results indicate that large-amplitude superinertial internal tides should be able to occur on realistic continental shelves of ocean basins, due to resonance associated with small segments of a shelf, not needing to communicate with the entire alongshelf distance of a basin. This could account for some observations of alongshelf variability in superinertial internal tides.

4.2 Introduction

Observations of structures that are consistent with coastal-trapped superinertial internal tides exist (Alford et al. 2006; Klymak et al. 2016; Lerczak et al. 2003), but their dynamics are not well understood. Previous theoretical studies have shown that below the inertial frequency, barotropic and baroclinic coastal-trapped waves are perfectly trapped, losing no energy to the deep basin (Huthnance 1975, 1978). Above the inertial frequency, trapping is perfect for barotropic modes in a homogeneous basin and for baroclinic modes in a two-layer rigid lid basin, but in continuously stratified basins, linear theory shows that trapping is no longer perfect, with barotropic and baroclinic edge waves losing energy through internal wave scattering in all directions offshore (Huthnance 1978; Chapman 1982; Dale and Sherwin 1996; Dale et al. 2001). Dale et al. (2001) indicate that the change from perfectly trapped waves to nearly trapped is gradual as the frequency becomes superinertial. They show in a primitive equation model that locally generated strongly superinertial alongshore propagating internal tides with large amplitudes can form through the interaction of the barotropic tide with alongshore variable bathymetry, propagating long distances (hundreds of kilometers), of course still scattering some energy to the deep sea. It is not clear how quickly imperfectly trapped superinertial waves lose energy to the deep sea, however it has been suggested that continental shelf geometry that is appropriately tuned to a superinertial frequency (e.g. the $M2$ tide frequency at mid-latitudes) could, through resonance, result in large-amplitude coastal-trapped superinertial internal tides with alongshelf dependence (Dale and Sherwin 1996).

We explore this possibility by studying superinertial coupled barotropic-baroclinic resonant modes in an idealized rotating basin with alongshore variability in continental shelf width, with a particular focus on the baroclinic response over the shelf. We build on the knowledge gained in our work on these modes in basins with alongshore uniform shelves (thesis Chapter 3), here using a small ratio between shelf and deep basin phase speeds because this enhances shelf trapping of modes. In nature, shelves are not uniform alongshore as in the basins of thesis Chapter 3. Thus, there can be localized shelf responses that depend on both across- and alongshelf shape, which we explore in this study. Our specific objectives are to:

1. compare some resonant mode structures from this basin with alongshore shelf-width variability to like modes from the basin with alongshore uniform shelves, describing how alongshore variable shelves change particular mode responses;
2. describe some of the different types of mode structures that can exist, focusing on the baroclinic response over the shelf;
3. and compare the shelf response between narrow and wide shelf regions.

As shown in thesis Chapter 3, here we will see that the shelf width must be at least a quarter-wavelength of a mode to start to influence the structure of a basin mode; that barotropic modes have coupled baroclinic scales and that baroclinic modes can have coupled barotropic scales; that resonant large amplitudes can be confined to the shelf; that phase propagation in the rotating basin can be in either direction, and with amplitude structures, can result in complicated wave patterns that appear to propagate in some cases and in others appear more standing; and that some modes appear more Kelvin-like. And now with the introduction of alongshore variability in

shelf width, here we will show that a mode can be influenced by a segment of shelf, with the shelf response of lower modes being affected only by wider shelf sections while having the same behavior over narrow shelf sections as in the deep basin; that trapping can be confined to a particular section of shelf; and that wavelengths and sense of phase propagation can be different for shelf regions with different widths, even within the same resonant mode.

Superinertial trapped edge modes can propagate in either direction, cyclonically or anticyclonically. Whereas in basins without rotation, edge modes in the two directions are symmetric, having the same wavelengths and frequencies for propagation along a particular shelf width, in basins with rotation, that symmetry is broken, such that for a given alongshore wavelength and shelf width, an edge wave propagating anticyclonically has a greater frequency than the corresponding cyclonic edge wave (Huthnance 1975). Another way to think of that is that for a fixed frequency and shelf width, an edge mode that propagates cyclonically would have a smaller alongshore wavelength than an anticyclonic edge mode. Thus, an edge mode for certain shelf geometry (width and length) will have a preferred propagation direction for a given superinertial frequency. The different propagation directions and wavelengths that we will show over the wide versus narrow shelf regions demonstrate this asymmetry.

The sections in this paper are organized as follows: In section 4.3, we describe the set up of the problem and the basin. In section 4.4, we present resonant mode structures that compare to like modes in the basin with alongshore uniform shelves (thesis Chapter 3), showing that the dominating large amplitudes distributed along the entire wide shelf from the alongshore uniform shelves are now isolated to the wide

portion of the shelf, for these low wavenumber modes. In section 4.5, we present and describe various baroclinic modes of increasing frequency, σ, comparing the response over the wide versus narrow portions of the shelf. In section 4.6, we summarize the results and discuss implications for coastal superinertial internal tides.

4.3 Setting up the problem

We use the set of second-order partial differential equations and boundary conditions derived from the forced, linear, inviscid, Boussinesq, shallow water equations, for a two-layered basin with a free surface, rotating on an f-plane, in thesis Chapter 3 to solve for the displacement of the free sea surface and internal interface, similar to the method used in Winant (2010), as follows:

$$\frac{h_1}{\sigma^2(1-f^2)}\left(\frac{\partial^2}{\partial x^2}+\frac{\partial^2}{\partial y^2}\right)N'+N'-Z=-\overline{N}\,,\text{ and} \tag{4.1}$$

$$\begin{aligned}\frac{1}{\sigma^2(1-f^2)}\Bigg[(h(x,y)-h_1)\left(i\frac{\partial^2}{\partial x^2}+i\frac{\partial^2}{\partial y^2}\right)+\frac{\partial h}{\partial x}\left(i\frac{\partial}{\partial x}+f\frac{\partial}{\partial y}\right)\\ +\frac{\partial h}{\partial y}\left(-f\frac{\partial}{\partial x}+i\frac{\partial}{\partial y}\right)\Bigg](N'+\rho Z)+iZ=0\,,\end{aligned} \tag{4.2}$$

where

$$\overline{N}(x,y)=\frac{A^*}{H^*}cos(ly)e^{ikx}\,, \tag{4.3}$$

and where all variables and parameters without the symbol * are non-dimensional, $\overline{N}$ is the idealized equilibrium tide forcing (with dimensional amplitude A^*), N' is the

deviation of sea level from the forcing, Z is the deviation of the internal interface, and the solutions and forcing are assumed to be periodic in time at superinertial frequency σ. The parameter $h(x, y)$ is bathymetry, and h_1 is the resting thickness of the upper layer. The non-dimensional parameters σ, f, and ρ come from:

$$\sigma = \frac{\sigma^* L_x^*}{\sqrt{g^* H^*}};\ f = \frac{f^*}{\sigma^*};\ \text{and}\ \rho = \frac{\Delta\rho^*}{\rho_o^*}\,, \tag{4.4}$$

where σ^* is the forcing frequency; L_x^* is the basin length in the x-direction; and H^* is the maximum deep basin depth, and all other variables are non-dimensionalized using L_x^* for horizontal scales, H^* for vertical scales and bathymetry, and σ^* for time. See thesis Chapter 3 for more details.

At the solid basin boundaries ($x^* = 0, L_x^*$; $y^* = 0, L_y^*$; or $x = 0, 1$; $y = 0, \frac{L_y^*}{L_x^*}$), normal transport must vanish, resulting in four boundary conditions:

$$f\frac{\partial N'}{\partial y} + i\frac{\partial N'}{\partial x} = 0\Big|_{x=0,1}\,, \tag{4.5}$$

$$-f\frac{\partial N'}{\partial x} + i\frac{\partial N'}{\partial y} = 0\Big|_{y=0,\frac{L_y^*}{L_x^*}}\,, \tag{4.6}$$

$$f\frac{\partial Z}{\partial y} + i\frac{\partial Z}{\partial x} = 0\Big|_{x=0,1}\,, \tag{4.7}$$

$$-f\frac{\partial Z}{\partial x} + i\frac{\partial Z}{\partial y} = 0\Big|_{y=0,\frac{L_y^*}{L_x^*}}\,. \tag{4.8}$$

The equations are solved using the computational method of Lindzen and Kuo (1969), keeping f constant and superinertial, at $f = 0.73$, and solving over a range of

σ to identify unbounded resonant peaks in response amplitude. Our previous work (in thesis Chapter 3) showed that a small shelf-deep basin phase speed ratio leads to greater trapping of modes over the shelf, so this basin uses a small baroclinic (and barotropic) ratio of $\delta = 0.22$, which is set by choosing an upper layer thickness of $h_1 = 0.0475$ for the shelf depth of $h_s = 0.05$.

The two-layered basin geometry is similar to that in thesis Chapter 3, but now with a shelf only on the western end of the basin (Fig. 4.1). The shelf is narrow to the north and south (each narrow segment is approximately 0.12 long and 0.039 wide), with a wide middle section that has the same width as that of the basins with wide shelves in thesis Chapter 3 (approximately 0.26 long and 0.13 wide). The shelf is flat, and the continental slope down to the deep basin has the same structure as in the basins of thesis Chapter 3 (see Chapter 3 Fig. 3.1).

4.4 Low mode resonant structures for the alongshore variable shelf compared to an alongshore uniform shelf

Comparing particular modes from this basin to that with alongshore uniform shelves in thesis Chapter 3, we find in general that the lower modes that had dominating large amplitudes along the entire wide shelf now have their largest amplitudes isolated to the wide section of shelf. As for the uniform shelf basins, the lowest baroclinic modes appear Kelvin-like, with phase propagating cyclonically around the basin and amplitude increasing with distance from amphidromes.

For the first baroclinic basin mode, the amplitudes are less confined to the shelf

for the variable shelf than for the basin with uniform shelves (Fig. 4.2 compared to thesis Chapter 3 Fig. 3.21). Here, there is a slight increase in amplitude over the wide portion of the shelf, and deep basin amplitudes are relatively large. This basin mode is not yet being heavily influenced by the shelf, because unlike for basin with alongshore uniform shelves, much of the shelf here is too narrow for the large wavelength mode to be affected by it.

The next baroclinic mode looks like a shelf-amplified basin mode, with the shelf-amplified interface response similar to that along the entire shelves of the basin with alongshore uniform shelves for the second baroclinic mode (see thesis Chapter 3, Fig. 3.22), but here isolated to just the wide section of the shelf (Fig. 4.3). Compared to the first baroclinic mode, this mode is affected by the presence of the wide part of the shelf more strongly, because the smaller wave scale now approximately fits a quarter wave across the wide shelf region. The amplitudes over the narrow shelf regions are the same as in the deep basin, because these shelf regions are too narrow for the mode to notice. So, we see that a full basin mode can result in dramatic alongshore variability in internal tide amplitudes due to alongshore variability in shelf width, and generate large-amplitude alongshore phase propagation of the superinertial internal tide over this wider portion of shelf.

The third baroclinic mode is a shelf-trapped edge mode, equivalent to the third baroclinic edge mode from the basin with alongshore uniform shelves in thesis Chapter 3 (see thesis Chapter 3, Figs. 3.23 and 3.24). Here, the shelf-trapping is isolated to the wide portion of the shelf, where phase propagates alongshore cyclonically (Fig. 4.4). This mode demonstrates that baroclinic edge modes can be isolated to an

alongshore segment of shelf with an appropriate width and result in what looks like a coastal-trapped alongshore propagating superinertial internal tide.

If we try to apply the equation for predicting baroclinic edge mode frequencies in a non-rotating basin with alongshore uniform shelves from thesis Chapter 3 to this basin with rotation and shelves that vary in width, solving it only for the geometry of the wide section of shelf, (equation 3.28: $\sigma_{m,q} = \sqrt{c_s^2 \left[\left(\frac{(2m-1)\pi}{2L_s} \right)^2 + \left(\frac{q\pi}{L_y} \right)^2 \right]}$, $(m = 1, 2, 3, ...;\ q = 1, 2, 3, ...)$, where c_s is the coupled baroclinic phase speed over the shelf), we find that the results do not compare well with observed frequencies. At the time step shown, the trapped wave has a full wavelength fitting along the wide section of shelf, but 90° later in phase, a half wavelength occupies the alongshelf extent of the region of wide shelf. If we solve for a half wavelength alongshelf (therefore, $q = 1$), we get $\sigma = 0.4155$, and for a full wavelength alongshelf ($q = 2$), we get $\sigma = 0.6531$. The actual frequency of this mode is $\sigma = 0.6045$, so the prediction using a full wavelength is closer to the actual frequency, but neither is very close. The edge mode equation does not account for rotation, and now that we have variable shelf width, the boundary conditions at the north and south "ends" of the wide segment are different from the boundary conditions at the coastal wall for which the equation was derived, so this non-rotating equation for approximating edge modes is not be suitable for use in this more realistic, rotating basin.

As done in thesis Chapter 3, we confirmed this is an edge mode by extending the deep basin, making it 50% longer, and forcing at the same dimensional frequency, finding that the shelf response stays the same, while the deep basin changes (Fig. 4.5). Note that based on the equation for predicting non-rotating edge modes just

discussed, σ for this mode would be approximately 50% larger than the original σ, but it is slightly lower than that. For the basin without the extended deep part, $\sigma = 0.6045$, so the predicted value for the non-rotating edge mode in the extended basin would be $\sigma = 0.9068$. But, the actual value is $\sigma = 0.8801$. This is related to the issues with applying that non-rotating equation here, just discussed.

As in the rotating basin with alongshore uniform shelves, the complicated coupled mode structures can be difficult to distinguish as barotropic or baroclinic, especially with the large value of ρ that we use ($\rho = 0.25$). We show two examples of modes that are possibly barotropic basin modes, both which are coupled with smaller scale baroclinic waves throughout the basin (Figs. 4.6 and 4.7). The first example has a barotropic component that corresponds to the barotropic basin mode from the non-rotating basin of thesis Chapter 3 that is mode one in the x-direction and mode zero in the y-direction. The barotropic sea surface structure in Fig. 4.6a compares well to the baroclinic interface structure of the first baroclinic basin mode in Fig. 4.2b, propagating phase cyclonically, with largest amplitudes over the shelf, particularly on the wide part. The baroclinic interface response for the mode is largest over the shelf, especially along the narrow extent where phase propagates cyclonically alongshelf, with amplitudes much greater than those of the barotropic sea surface.

The second barotropic example (Fig. 4.7) corresponds to the barotropic shelf-amplified basin mode in the non-rotating basin that is mode two in the x-direction and mode zero in the y-direction. The barotropic sea surface structure in Fig. 4.7a compares well to the baroclinic interface structure of the second baroclinic basin mode in Fig. 4.3b. The barotropic component propagates phase alongshelf cyclonically,

and sea surface has its greatest amplitudes over the wide portion of the shelf. The baroclinic interface response for this mode is also largest over the wide portion of shelf, where there is complicated phase rotation around amphidromes. Against the coast along the narrow extent, baroclinic phase propagates cyclonically. Thus, the resonant barotropic modes are coupled with large amplitude baroclinic scales confined to the shelf.

4.5 Higher baroclinic mode resonant structures and how their response compares for the narrow and wide shelf regions

Next we look at examples of higher baroclinic mode resonant structures, increasing in frequency σ, with a focus on interface shelf responses and how they vary between the narrow and wide shelf regions, also showing some examples of interesting deep basin responses.

The first example has a structure that is somewhat similar to the baroclinic edge mode presented in Fig. 4.4, with maximum amplitudes isolated to the wide shelf region, but here the distribution of amplitude is not uniform over the wide shelf region (Fig. 4.8). In the edge mode, phase propagated strictly southward over the wide shelf region, but here, the node of the cyclonic shelf amphidrome is located on the shelf, such that along the coast, the two regions of large amplitude look like a wave propagating southward, and farther out on the wide portion of the shelf, lower amplitudes have phase that propagates northward. In the deep basin, the eastern half has cyclonic phase propagation, but the western half is anticyclonic,

unlike in the similar edge mode, where all deep phase propagation was around cyclonic amphidromes.

Large amplitudes over the shelf can also be along the entire shelf, but somewhat confined to the narrow width even along the wide portion of shelf, as in this next baroclinic mode (Fig. 4.9). Here, large amplitudes have phase that propagates southward (cyclonically) along the entire shelf. In this mode, we see that the alongshore wavelengths over the narrow shelf portions are longer than over the wide shelf. Attempting to apply the thesis Chapter 3 edge mode equation for $\sigma_{m,q}$ to this mode: for the narrow shelf region with a quarter wave across shelf and a half wave alongshelf, $\sigma_{1,1} = 1.1713$; for the wide shelf region with a quarter wave across shelf and two waves alongshelf, $\sigma_{1,4} = 1.1975$. These two frequencies are close to each other, indicating that if shelf geometry is tuned just right, there may be edge modes over more than just one alongshelf segment, and the resulting structure could appear to propagate alongshore continuously, changing wavelengths as it transitions into new shelf widths. The actual frequency for this mode is 1.3577. If we extend the deep basin by 50% to test if this is an edge mode, we would predict the same edge mode to occur for $\sigma = 2.0365$, but the resonant peak occurs at $\sigma = 1.9508$ (Fig. 4.10). The shelf structures for the two basins are very similar for both the narrow and wide portions of shelf, but do have slight differences, so while it is likely this is an edge mode, it is not entirely clear. If this is an edge mode, it may be one that is tuned appropriately to exist over both the narrow and wide shelf segments.

The next baroclinic mode example has opposing propagation directions on the wide and narrow shelf sections, demonstrating the asymmetry of edge modes in ro-

tating basins described by Huthnance (1975) (Fig. 4.11). For this mode, large interface amplitudes are trapped on the shelf, especially on the wide section. Over the wide section of shelf, the structure that has three-quarter waves across-shelf and a half wavelength alongshelf (Fig. 4.11b) circulates clockwise (anticyclonically), while along the narrow portions of shelf, waves with smaller alongshelf wavelengths propagate phase alongshore cyclonically. Thus, for a fixed frequency, the alongshore wavelength of the cyclonic wave over the narrow shelf is smaller than that of the anticyclonic wave over the wide shelf.

The next example has a complicated phase structure of alternating cyclonic and anticyclonic direction throughout the entire shelf, which in combination with the amplitude distribution, in general results in phase that appears to propagate southward over the wide portion of shelf and northward over the narrow portion (Fig. 4.12). As σ increases, smaller and smaller wave scales occur with more and more complicated phase and amplitude structures that result in various interesting patterns over the shelf, more of which we will explore, below.

The next resonant mode that we show has a complicated small-scale interface phase and amplitude structure over the shelf, but what is unique about this mode is the large-scale baroclinic horizontal banded pattern that is most visible in the sea surface, over approximately the western half of the basin, including the shelf (Fig. 4.13). The phase and amplitude distribution of this structure results in an almost standing appearance of the large horizontal bands. Other modes with this kind of banded pattern (e.g. from thesis Chapter 3, Fig. 3.27, Fig. 3.28; as well as ones to come in this chapter) either occur throughout the deep basin or isolated to the

shelf, so this one is unique in that the banded pattern does not persist throughout the entire deep basin and in that it exists over both the shelf and deep basin.

While most of the higher modes that we have shown with small wavelength scales over the shelf have had large amplitudes over the entire shelf, higher shelf modes can also be confined to the wide region of shelf, as in Fig. 4.14. Here, large amplitudes confined to the wide shelf region are much larger in amplitude than the response in the rest of the basin, which could indicate that this is an edge mode for the wide shelf region. The phase structure over the wide shelf region alternates between clockwise and counterclockwise propagation, creating a complicated pattern of motion that stays confined to the wide shelf region.

The final four baroclinic mode structures we present all have unique large-amplitude patterns over the wide portion of the shelf. The wide shelf response alternates between being in the large-amplitude pattern and being smaller amplitude, resulting in the large-amplitude patterns appearing almost standing. They somewhat resemble a marching band, aligning and spelling letters (with the large amplitudes) and then scattering in all direction while crouching down (the smaller amplitudes), then popping up to spell the letter again; or like a group of square dancers, matching up in a uniform line, then "dosey doeing" around each other, then reforming the line.

The mode in Fig. 4.15 does this, with the large shelf amplitudes outlining the outer edge shape of the wide section of shelf, thus sort of spelling a "D". Along the narrow width extent of shelf, smaller scales with consistently large amplitudes propagate phase southward alongshore, and the sea surface shows coupling with barotropic mode 1.

The mode in Fig. 4.16 spells more of a "B", with three lines of large amplitudes over the wide portion of the shelf: two lines following the shelf edge, and one going straight offshore. Also like the previous mode, along the narrow width extent of the shelf, smaller scales with consistently large amplitudes propagate phase southward alongshore.

The next mode is interesting in that at one stage of the phase, the dominating structure in both the sea surface and interface is a set of baroclinic horizontal bands stretching across the deep basin (Fig. 4.17a and 4.17b), and at another stage of the phase 90° later, the dominating structure is an interface pattern over the shelf like the two modes before this one, with sort of two rows of large amplitudes that follow the shape of the outer edge of the wide portion of shelf (Fig. 4.17c and 4.17d). The phase propagation and amplitude distribution is such that these two structures appear almost standing. Also like the previous two modes, along the narrow width extent of the shelf, smaller scales with consistently large amplitudes propagate phase southward alongshore.

The final resonant mode example is similar to these "letter spelling" modes, except that its large amplitude response is isolated to just the wide section of the shelf (thus, there is no large-amplitude phase propagation southward along the coast), and over the wide section of shelf, it alternates between two large amplitude patterns, sort of spelling a "C" in the phase period that is shown (Fig. 4.18), and then 90° later in phase, spelling a "D". So, this mode has two dominant large-amplitude periods, similar to the previous mode (Fig. 4.17), but with both isolated to the wide portion of the shelf. This mode also appears to have coupling with the second barotropic

mode (Fig. 4.7).

4.6 Discussion and conclusions

We have presented superinertial, coupled barotropic-baroclinic, resonant mode structures for an idealized two-layer basin with a continental shelf that varies in width alongshore and demonstrated that localized shelf responses can depend on both across- and alongshore shelf geometry, resulting in large-amplitude superinertial internal tides over the continental shelf with alongshelf dependence.

Comparing like modes from this basin to those in a basin with alongshore uniform shelves, we showed that for variable shelf width, shelf-amplification of low wavenumber basin modes occurs only over the wide segment of shelf which is close to at least a quarter-wavelength of the modes. In the real ocean, in a basin small enough for baroclinic waves to propagate across a basin and form baroclinic basin modes before stratification changes (see thesis Chapter 3), low wavenumber baroclinic basin modes that are only amplified over segments of shelf that are close to at least a quarter-wavelength of the mode would result in continuous propagation along the entire shelf that dramatically increases in amplitude over wide enough shelf segments (as for the mode in Fig. 4.3). We also showed that barotropic modes can have coupled large-amplitude, high wavenumber baroclinic responses isolated to the shelf. An interesting question to explore with a barotropic mode like these would be to see if the large-amplitude baroclinic component over the shelf needs to communicate with just the shelf, or with the entire basin. If just the shelf, then in a real, large ocean basin, this

kind of resonant coupled mode excitation could result in large-amplitude baroclinic internal tides over the shelf coupled to the barotropic tide, with both being part of a single resonant mode response. One way to test this would be through using a numerical model that allows for watching the development of a mode through time, such as the Regional Ocean Modeling System (ROMS).

The resonant baroclinic modes that we presented demonstrate that in any size ocean basin with a segment of shelf geometry that is appropriately tuned to a resonant edge mode, large-amplitude coastal-trapped superinertial internal tides can occur due to resonance. A large-amplitude superinertial internal tide due to a resonant mode can result in many diverse structures over the continental shelf, depending on the shelf width and length relative to the superinertial frequency. Phase and amplitude structures over the shelf can be such that the wave appears to propagate alongshore (e.g. Figs. 4.4 and 4.9), or in circles over a section of shelf (e.g. Fig. 4.11), or around complicated amphidrome structures (e.g. Fig. 4.14), sometimes resulting in what appears almost as standing waves with interesting patterns related to the shape of the shelf segment (e.g. Figs. 4.15, 4.16, 4.17, and 4.18). Large amplitudes can be confined to a segment of shelf, not needing to communicate with the entire alongshelf extent to develop (e.g. Fig. 4.4), or exist over multiple shelf segments, with the behavior of a particular mode structure changing as shelf width changes, resulting in changes in wavelengths between narrow and wide shelf regions (e.g. Fig. 4.9) and the possibility for changes in sense of propagation between shelf segments of varying width (e.g. Fig. 4.11), even within the same resonant mode. This is due to the asymmetry of edge modes in rotating basins, which, for a fixed alongshore wavenumber and shelf width,

causes edge modes that are anticyclonic to have a greater frequency than cyclonic edge modes, resulting in preferred propagation directions for a given frequency and shelf geometry (Huthnance 1975).

Comparison of the baroclinic edge mode in Fig. 4.4 with the equivalent edge mode in the basin with uniform shelves (thesis Chapter 3 Figs. 3.23 and 3.24) and finding the same structure in the extended basin show that this is a baroclinic edge mode confined to the wide section of shelf. The similar shelf structures between the regular and extended basins for the baroclinic mode in Fig. 4.9 show this may be a baroclinic edge mode along the entire shelf. But none of the other resonant modes presented here have been proven to be edge modes. We have demonstrated that their shelf amplitudes are much larger than those in the deep basin, and that their shelf structures are different than in the deep basin, sometimes fitting multiples of quarter-wavelengths across-shore, but we have not shown that they are independent of the deep basin. We could test more modes to see if they are edge modes by extending the deep basin while keeping the rest of the basin unchanged, and seeing if we get the same shelf response for the same dimensional forcing frequency.

In a real ocean basin, while superinertial edge waves do lose energy from scattering of internal waves to the deep basin, resonant excitation allows for edge wave amplitudes to be large and to stay large as long as a shelf stratification (and geometry) remains tuned to the mode. We have shown that resonant edge mode excitation can occur over an appropriately tuned segment of shelf geometry and stratification, demonstrating that resonant baroclinic edge mode excitation can result in large-amplitude coastal-trapped superinertial internal tides with alongshelf dependence.

4.7 Acknowledgements

We thank our funding provider, the National Science Foundation (grants OCE 1155799 and OCE 1756752).

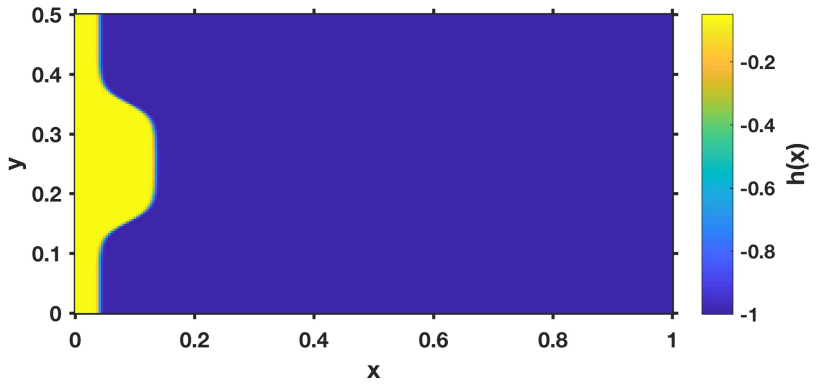

Figure 4.1: Plan view of the bathymetric structure of the non-dimensional basin. On the western end of the basin, the shelf is narrow to the north and south (each narrow segment is approximately 0.12 long and 0.039 wide), with a wide middle section (approximately 0.26 long and 0.13 wide). The wide middle section is the same width as in the basins with wide shelves in thesis Chapter 3. The shelf is flat, with a continental slope down to the deep basin as in the basins of thesis Chapter 3 (see Chapter 3, Fig. 3.1).

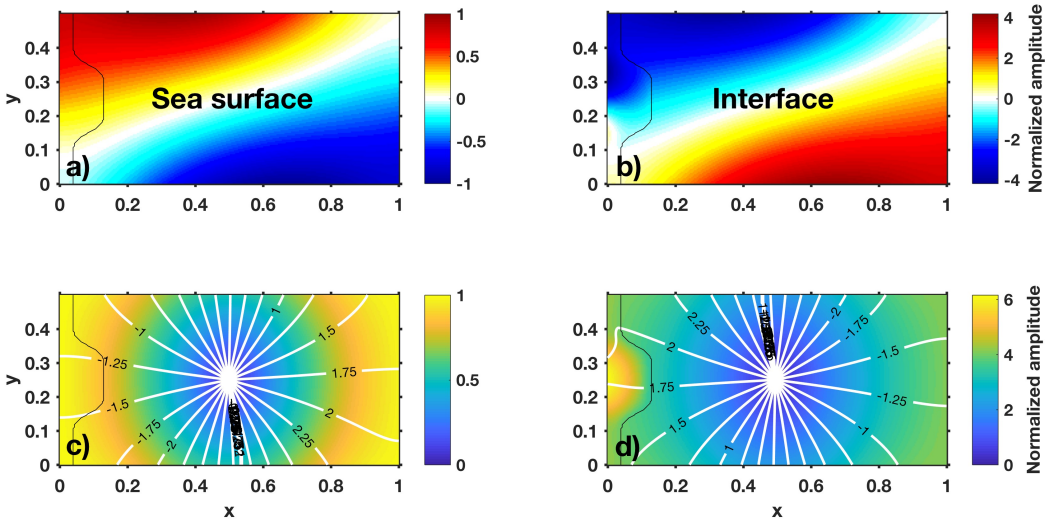

Figure 4.2: Baroclinic basin mode ($\sigma = 0.2896$). This corresponds to the baroclinic basin mode in the non-rotating basin of thesis Chapter 3 that is mode one in the x-direction and mode zero in the y-direction. Normalized displacement (relative to sea surface) for the (a) sea surface and (b) interface; and normalized amplitudes (relative to sea surface, colors) and phases (white contours, propagation direction is toward lower phase) for the (c) sea surface and (d) interface. Vertical grey line denotes shelf width. The mode propagates around a central cyclonic amphidrome, with maximum amplitudes in the interface over the wide portion of the shelf.

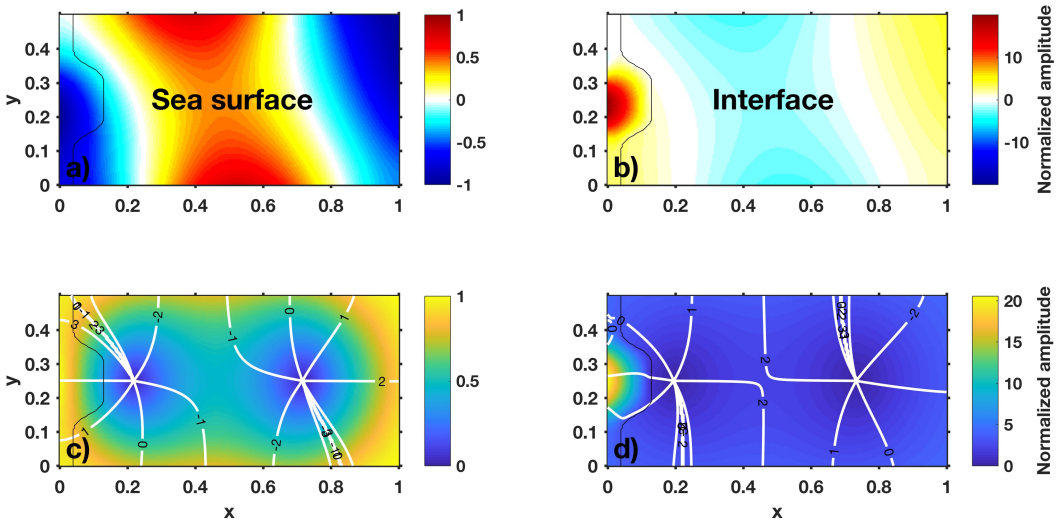

Figure 4.3: Baroclinic shelf-amplified basin mode ($\sigma = 0.5026$). This corresponds to the baroclinic shelf-amplified basin mode in the non-rotating basin of thesis Chapter 3 that is mode two in the x-direction and mode zero in the y-direction. Normalized displacement (relative to sea surface) for the (a) sea surface and (b) interface; and normalized amplitudes (relative to sea surface, colors) and phases (white contours, propagation direction is toward lower phase) for the (c) sea surface and (d) interface. Vertical grey line denotes shelf width. The mode propagates around two cyclonic amphidromes, with maximum amplitudes in the interface over the wide portion of the shelf.

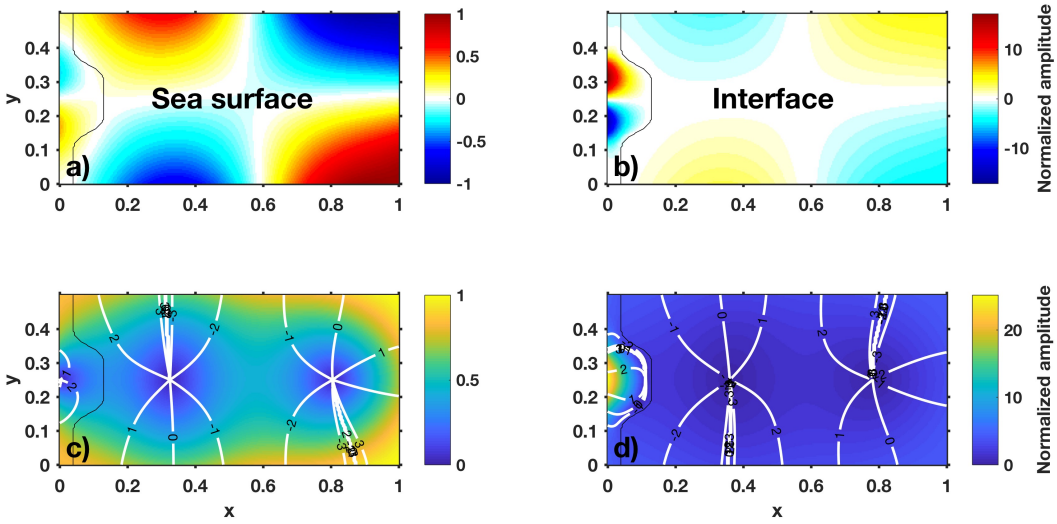

Figure 4.4: Baroclinic edge mode ($\sigma = 0.6045$). This corresponds to the baroclinic edge mode in the non-rotating basin of thesis Chapter 3 that is 1/4-wavelength across the shelf and mode one in the y-direction. Normalized displacement (relative to sea surface) for the (a) sea surface and (b) interface; and normalized amplitudes (relative to sea surface, colors) and phases (white contours, propagation direction is toward lower phase) for the (c) sea surface and (d) interface. Vertical grey line denotes shelf width. Interface amplitudes decay greatly away from the wide portion of the shelf, with cyclonic alongshore propagation on the shelf and small-amplitude cyclonic propagation in the deep basin.

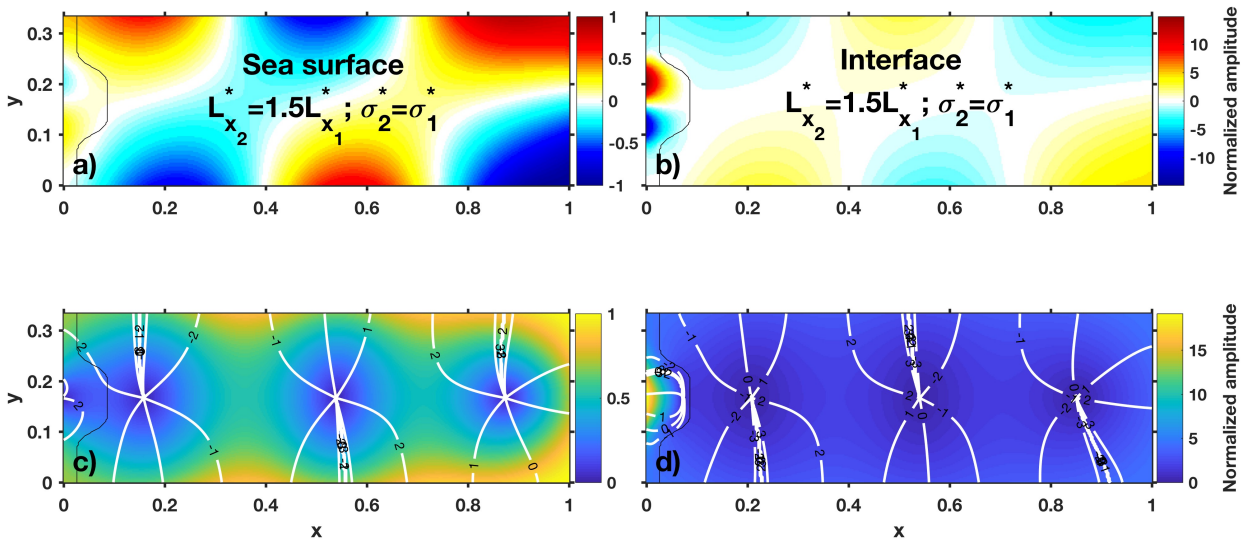

Figure 4.5: Baroclinic edge mode, but with the deep basin extended so that the total basin length that is 50% larger ($\sigma = 0.8801$). This is the same edge mode as in the regular basin length in Fig. 4.4, and is forced at the same dimensional frequency, showing that both show the same edge mode. Normalized displacement (relative to sea surface) for the (a) sea surface and (b) interface; and normalized amplitudes (relative to sea surface, colors) and phases (white contours, propagation direction is toward lower phase) for the (c) sea surface and (d) interface. Vertical grey line denotes shelf width.

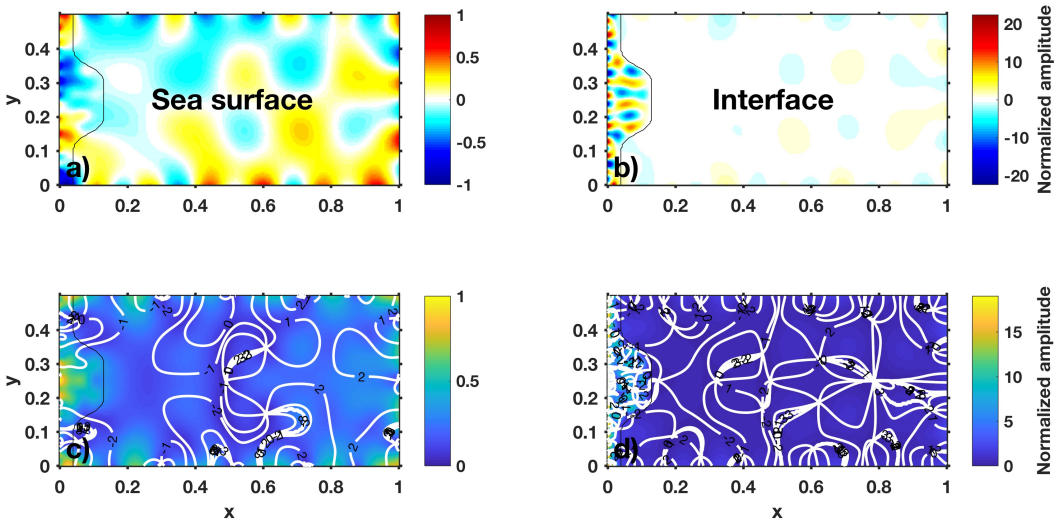

Figure 4.6: Possibly barotropic basin mode, with coupled smaller scale baroclinic waves throughout the basin ($\sigma = 3.6092$). The barotropic component corresponds to the barotropic shelf-amplified basin mode in the non-rotating basin of thesis Chapter 3 that is mode one in the x-direction and mode zero in the y-direction. Normalized displacement (relative to sea surface) for the (a) sea surface and (b) interface; and normalized amplitudes (relative to sea surface, colors) and phases (white contours, propagation direction is toward lower phase) for the (c) sea surface and (d) interface. Vertical grey line denotes shelf width. The barotropic component propagates phase cyclonically, and the sea surface has its greatest amplitudes over the shelf, particularly over the wide part, associated with that motion. The barotropic sea surface structure in (a) for this first barotropic basin mode compares well to the interface structure of the first baroclinic basin mode in Fig. 4.2.

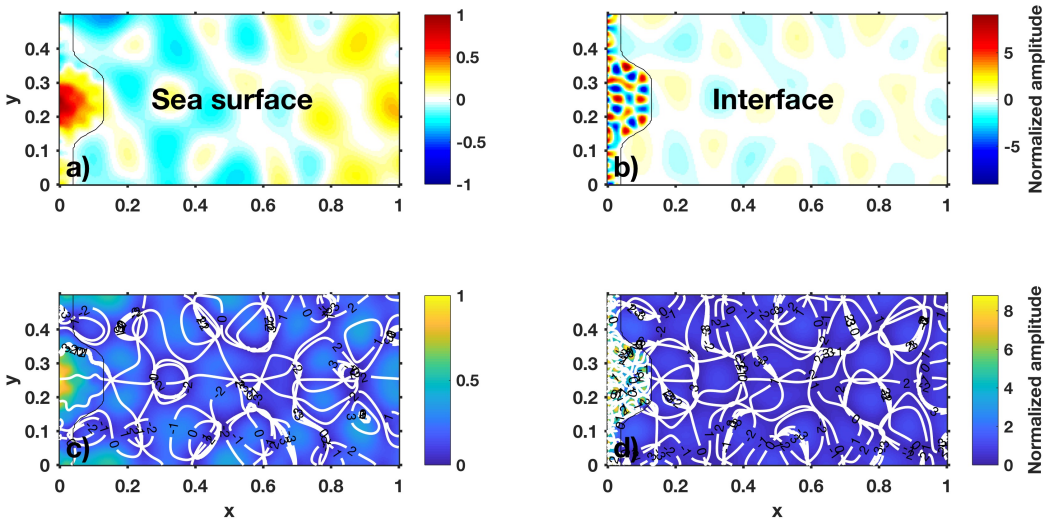

Figure 4.7: Possibly barotropic basin mode, with coupled smaller scale baroclinic waves throughout the basin ($\sigma = 4.6240$). The barotropic component corresponds to the barotropic basin mode in the non-rotating basin of thesis Chapter 3 that is mode two in the x-direction and mode zero in the y-direction. Normalized displacement (relative to sea surface) for the (a) sea surface and (b) interface; and normalized amplitudes (relative to sea surface, colors) and phases (white contours, propagation direction is toward lower phase) for the (c) sea surface and (d) interface. Vertical grey line denotes shelf width. The barotropic shelf component propagates phase along the shelf, cyclonically, and the sea surface has its greatest amplitudes over the wide portion of shelf, associated with that motion. The barotropic sea surface structure in (a) for this second barotropic basin mode compares well to the interface structure of the second baroclinic (shelf-amplified) basin mode in Fig. 4.3.

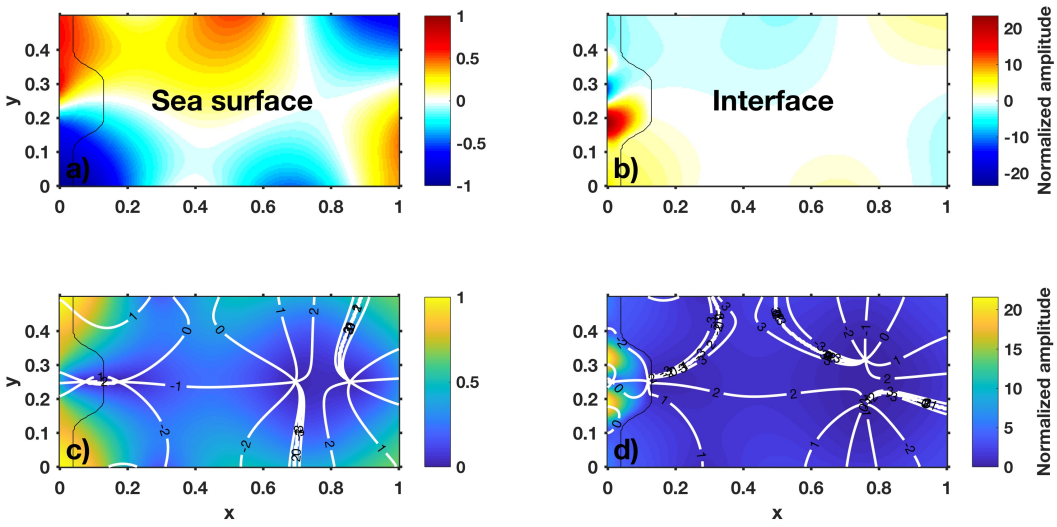

Figure 4.8: Baroclinic mode ($\sigma = 0.8567$). Normalized displacement (relative to sea surface) for the (a) sea surface and (b) interface; and normalized amplitudes (relative to sea surface, colors) and phases (white contours, propagation direction is toward lower phase) for the (c) sea surface and (d) interface. Vertical grey line denotes shelf width.

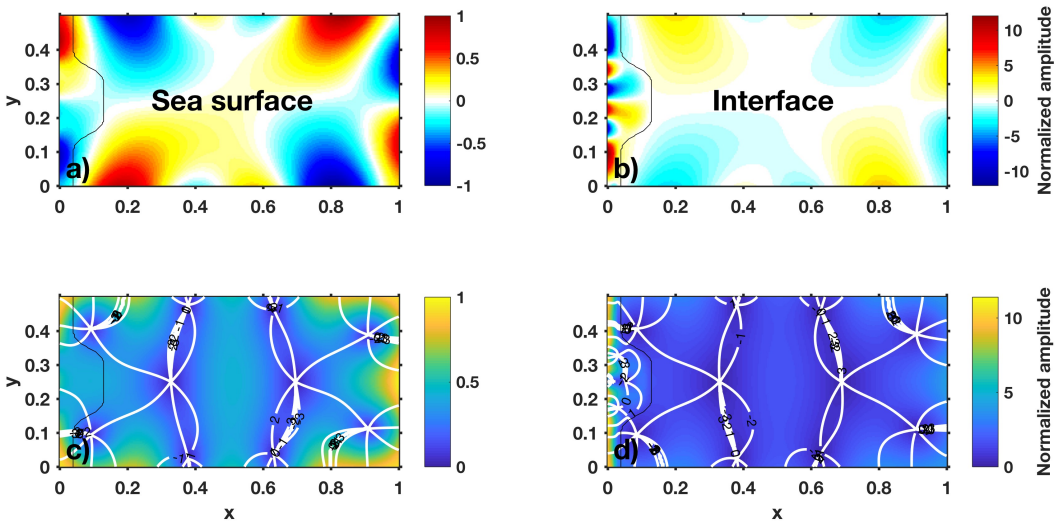

Figure 4.9: Baroclinic edge mode ($\sigma = 1.3577$). Normalized displacement (relative to sea surface) for the (a) sea surface and (b) interface; and normalized amplitudes (relative to sea surface, colors) and phases (white contours, propagation direction is toward lower phase) for the (c) sea surface and (d) interface. Vertical grey line denotes shelf width.

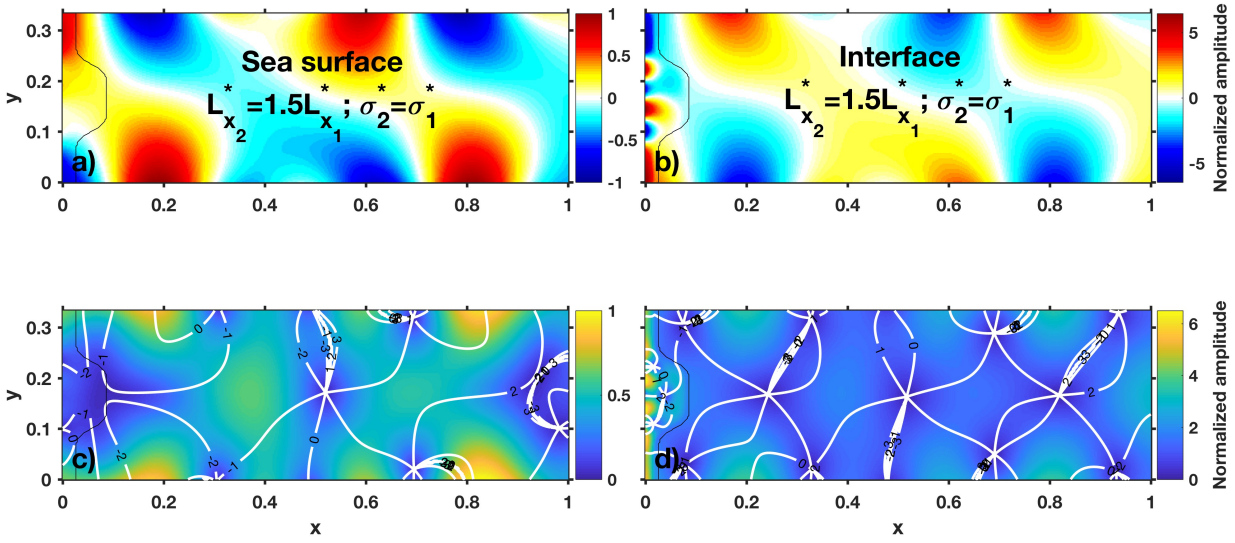

Figure 4.10: Baroclinic edge mode, but with the deep basin extended so that the total basin length that is 50% larger ($\sigma = 1.9508$). This is the same edge mode as in the regular basin length in Fig. 4.9, and is forced at the same dimensional frequency, proving that both show the same edge mode. Normalized displacement (relative to sea surface) for the (a) sea surface and (b) interface; and normalized amplitudes (relative to sea surface, colors) and phases (white contours, propagation direction is toward lower phase) for the (c) sea surface and (d) interface. Vertical grey line denotes shelf width.

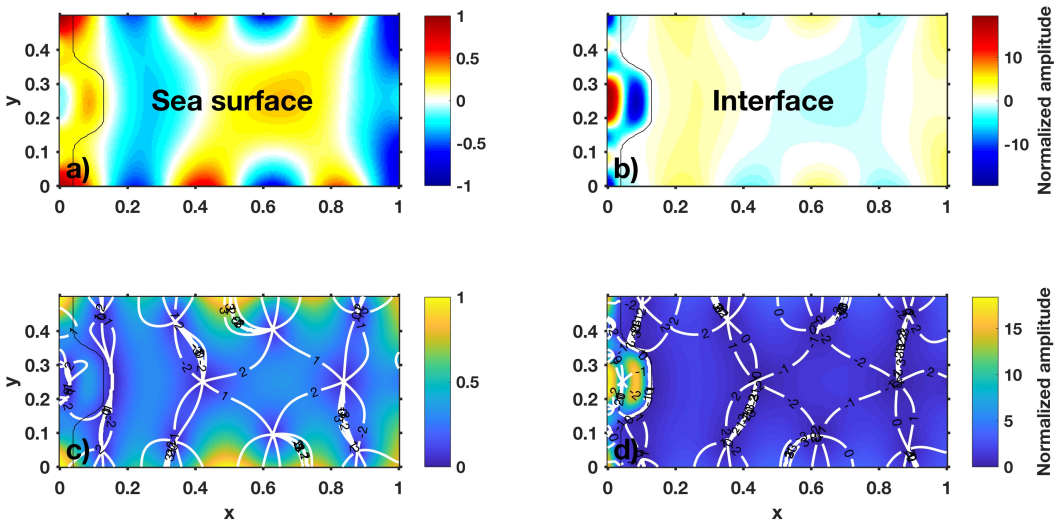

Figure 4.11: Baroclinic mode ($\sigma = 1.5170$). Normalized displacement (relative to sea surface) for the (a) sea surface and (b) interface; and normalized amplitudes (relative to sea surface, colors) and phases (white contours, propagation direction is toward lower phase) for the (c) sea surface and (d) interface. Vertical grey line denotes shelf width.

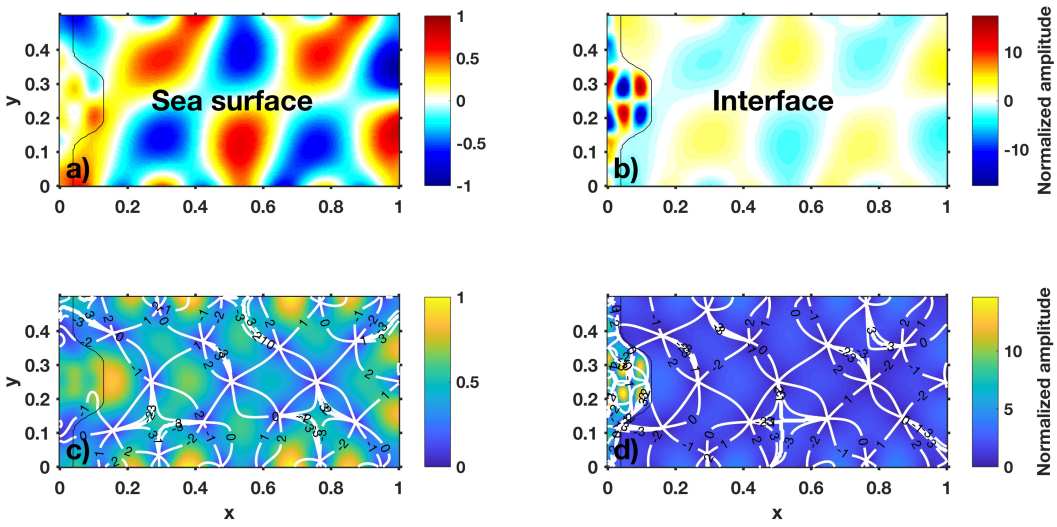

Figure 4.12: Baroclinic mode ($\sigma = 2.5702$). Normalized displacement (relative to sea surface) for the (a) sea surface and (b) interface; and normalized amplitudes (relative to sea surface, colors) and phases (white contours, propagation direction is toward lower phase) for the (c) sea surface and (d) interface. Vertical grey line denotes shelf width.

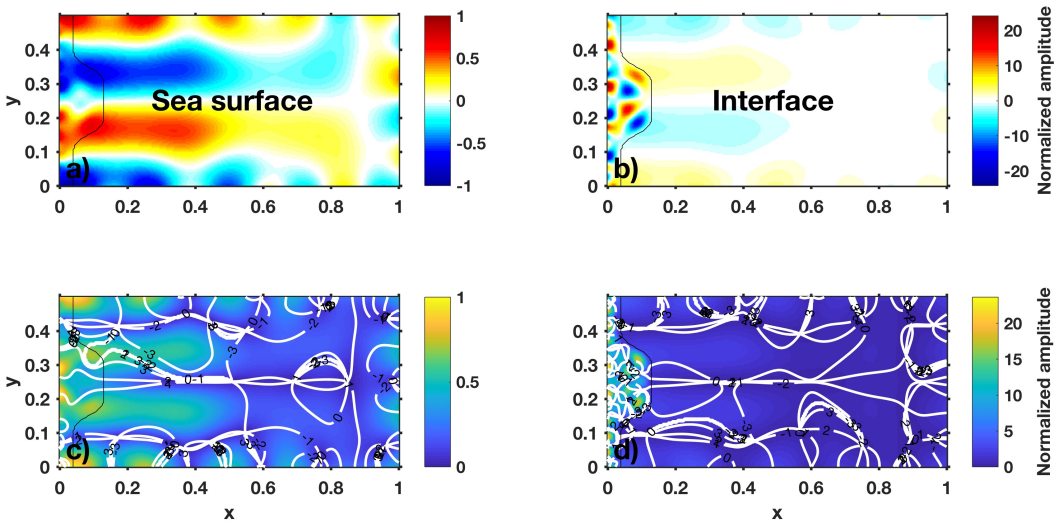

Figure 4.13: Baroclinic mode ($\sigma = 2.6547$). Normalized displacement (relative to sea surface) for the (a) sea surface and (b) interface; and normalized amplitudes (relative to sea surface, colors) and phases (white contours, propagation direction is toward lower phase) for the (c) sea surface and (d) interface. Vertical grey line denotes shelf width.

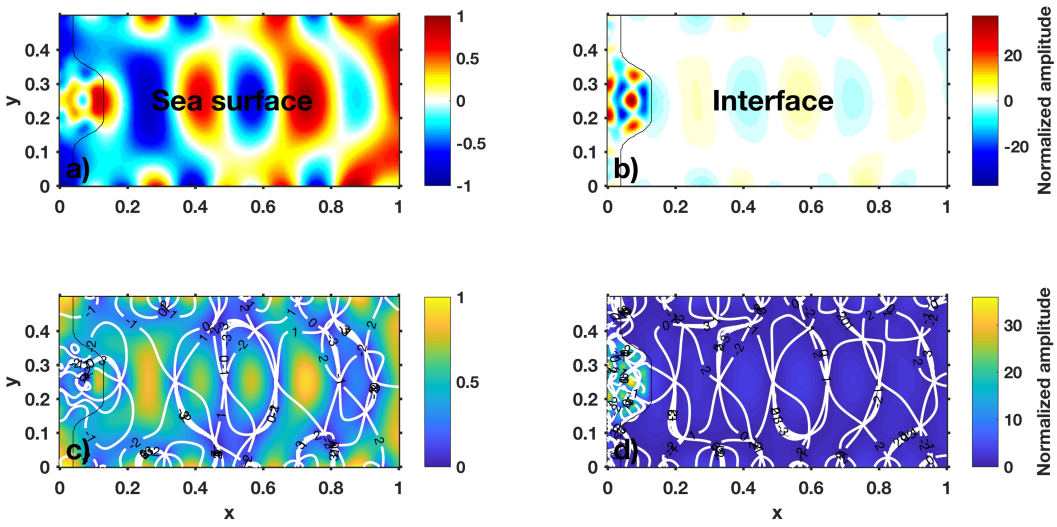

Figure 4.14: Baroclinic mode ($\sigma = 3.2008$). Normalized displacement (relative to sea surface) for the (a) sea surface and (b) interface; and normalized amplitudes (relative to sea surface, colors) and phases (white contours, propagation direction is toward lower phase) for the (c) sea surface and (d) interface. Vertical grey line denotes shelf width.

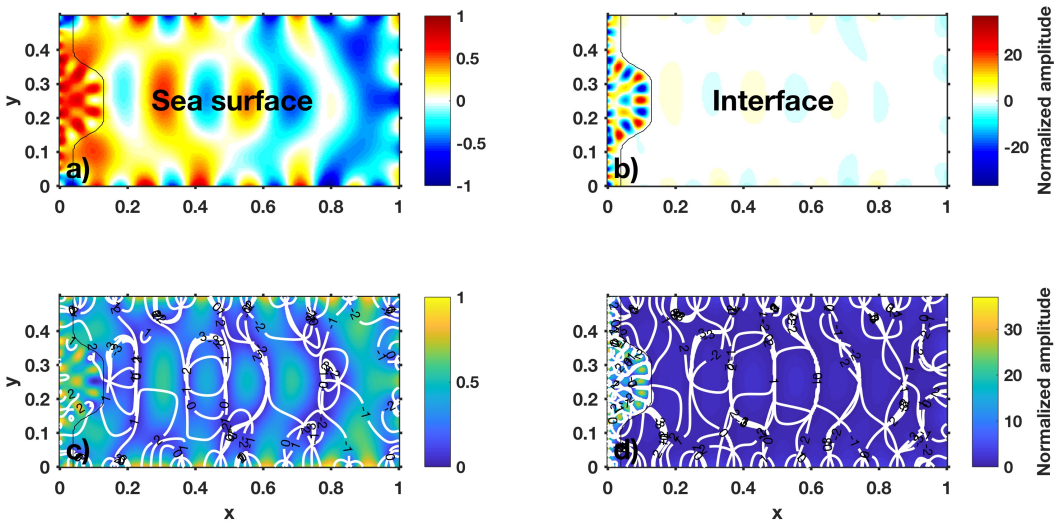

Figure 4.15: Baroclinic mode ($\sigma = 3.9813$). Normalized displacement (relative to sea surface) for the (a) sea surface and (b) interface; and normalized amplitudes (relative to sea surface, colors) and phases (white contours, propagation direction is toward lower phase) for the (c) sea surface and (d) interface. Vertical grey line denotes shelf width.

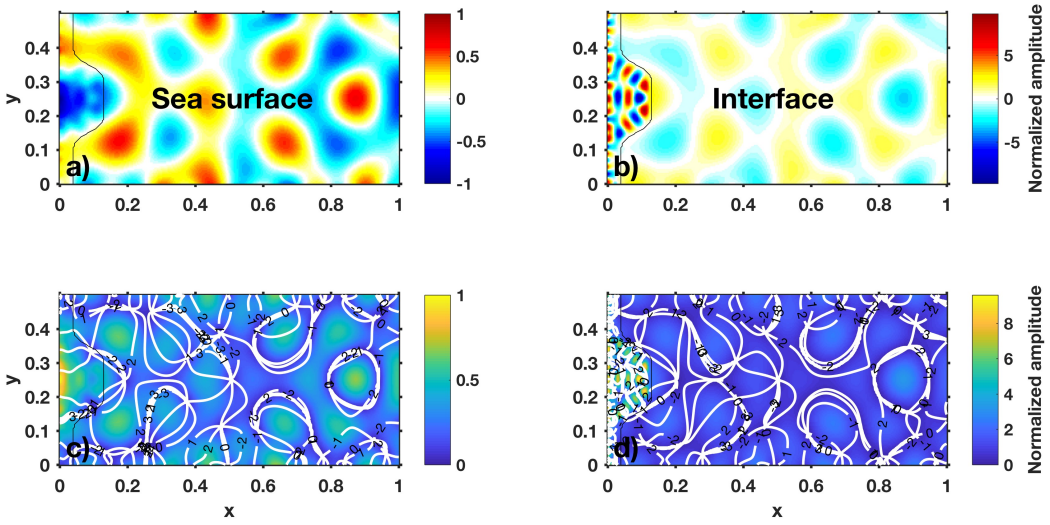

Figure 4.16: Baroclinic mode ($\sigma = 4.0085$). Normalized displacement (relative to sea surface) for the (a) sea surface and (b) interface; and normalized amplitudes (relative to sea surface, colors) and phases (white contours, propagation direction is toward lower phase) for the (c) sea surface and (d) interface. Vertical grey line denotes shelf width.

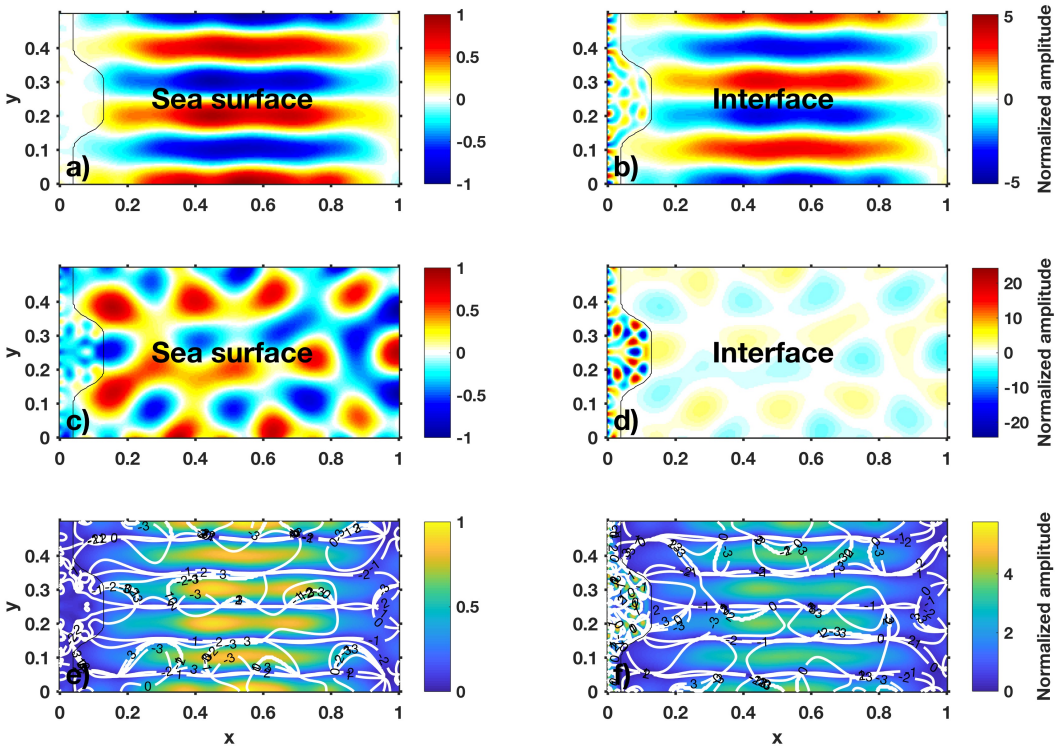

Figure 4.17: Baroclinic mode ($\sigma = 4.4599$). Normalized displacement (relative to sea surface) for the (a) and (c) sea surface and (b) and (d) interface; and normalized amplitudes (relative to sea surface, colors) and phases (white contours, propagation direction is toward lower phase) for the (e) sea surface and (f) interface. Vertical grey line denotes shelf width. Panels (a) and (b) are for the same time step; panels (c) and (d) are for a time step 90° later in phase.

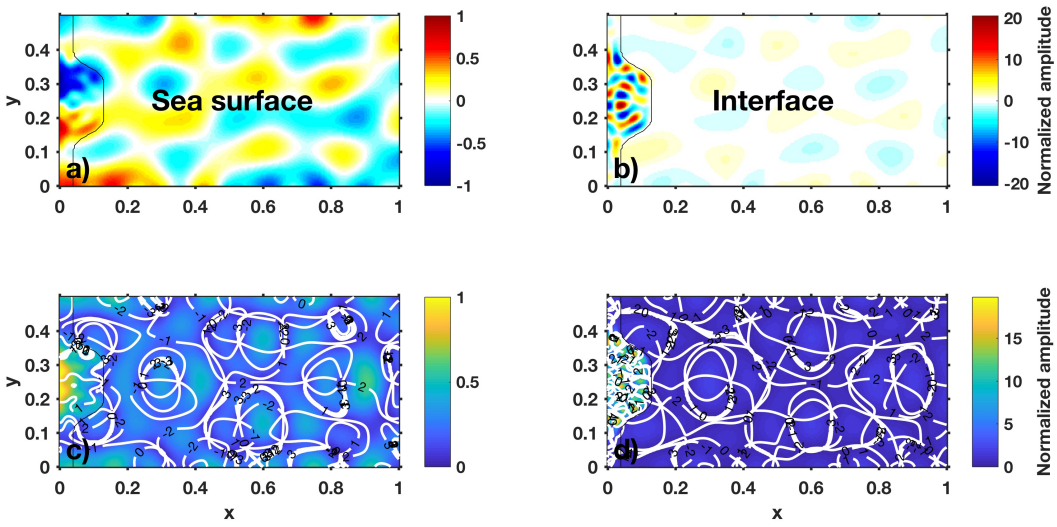

Figure 4.18: Baroclinic mode ($\sigma = 4.5179$). Normalized displacement (relative to sea surface) for the (a) sea surface and (b) interface; and normalized amplitudes (relative to sea surface, colors) and phases (white contours, propagation direction is toward lower phase) for the (c) sea surface and (d) interface. Vertical grey line denotes shelf width.

Chapter 5: General conclusions

This thesis has explored two different research directions associated with understanding horizontal (along- and across-shore) properties of internal waves, filling in gaps in our previous understanding of alongshore variability of internal waves and internal tides. From thesis Chapter 2, overall we found that seafloor pressure sensors are cost- and effort-efficient tools that are useful for determining the propagation direction and speed of high-frequency nonlinear internal waves and how those properties vary over a large horizontal extent on the continental shelf. While an array of these sensors can be used to qualitatively describe variations in internal wave kinetic energy, other methods (e.g. using ADCPs) are still necessary for quantitative analysis of internal wave energy, but the use of seafloor pressure sensors combined with these other methods can efficiently extend the ability to gain further understanding of horizontal variability of internal waves.

From thesis Chapters 3 and 4, we demonstrated that resonant mode excitation by the equilibrium tide can generate large-amplitude superinertial internal tides throughout smaller basins (e.g. Gulf of California, Gulf of Mexico) and on continental shelves of any size ocean basin, for appropriately tuned geometries and stratification. The structures of resonant basin and edge modes range from modes that appear to propagate alongshore, to modes that almost appear to be standing. Resonant modes can potentially explain some temporal variability observed in internal tides, with changes

in stratification tuning a basin or shelf toward or away from resonance over time. Resonant mode excitation can also explain some alongshelf variability of superinertial internal tides. Resonant edge modes can result in large-amplitude superinertial internal tides that are confined to a particular alongshelf segment, or they can result in alongshore variability in wavelengths and amplitudes as a superinertial internal tide propagates phase alongshore over regions of different shelf geometry, sometimes even having a different sense of phase propagation for different neighboring shelf regions.

The analytically derived equations and idealized basins used in Chapters 3 and 4 allow us to learn a lot about coupled barotropic-baroclinic resonant modes and their application to internal tides, but they do not allow us to study continuous stratification or the temporal evolution of modes. Perhaps a numerical model that allows for more complexity and for watching evolution through time, such as the Regional Ocean Modeling System (ROMS) could be used to explore: the effects of continuous stratification on resonant modes; or how much stratification can vary in time and still allow a mode to develop/the temporal intermittency timescales of superinertial internal tides due to stratification tuning toward/away from resonance. But, some challenges exist to working with ROMS to study resonant modes. For example, if setting up the problem in the same way as in this thesis, the bathymetry must encompass the range of depths from the coast to the deep basin, which can not occur steeply in ROMS. Another challenge is that resonant modes are difficult to find. The knowledge gained from the work in Chapters 3 and 4 could be used to narrow down the correct frequency/geometry/stratification combination that would result in a particular mode, but converging on the combination of parameters for a

particular resonance might take several model run attempts, requiring not only the time and resources for each model to run, but also analysis of each model run.

Bibliography

Aguirre, C., O. Pizarro, and M. Sobarzo, 2010: Observations of semidiurnal internal tidal currents off central Chile (36.6 °S). *Cont. Shelf Res.*, **30 (14)**, 1562–1574.

Alford, M. H., M. C. Gregg, and M. A. Merrifield, 2006: Structure, Propagation, and Mixing of Energetic Baroclinic Tides in Mamala Bay, Oahu, Hawaii. *J. Phys. Oceanogr.*, **36 (6)**, 997–1018.

Alford, M. H., R.-C. Lien, H. Simmons, J. Klymak, S. Ramp, Y. J. Yang, D. Tang, and M.-H. Chang, 2010: Speed and Evolution of Nonlinear Internal Waves Transiting the South China Sea. *J. Phys. Oceanogr.*, **40 (6)**, 1338–1355.

Allen, G., and J. Simpson, 2002: The Response of a Strongly Stratified Fjord to Energetic Tidal Forcing. *Estuar. Coast. Shelf Sci.*, **55 (4)**, 629–644.

Aristizábal, M. F., M. R. Fewings, and L. Washburn, 2016: Contrasting spatial patterns in the diurnal and semidiurnal temperature variability in the Santa Barbara Channel, California. *J. Geophys. Res. Ocean.*, **121 (1)**, 427–440.

Beardsley, R., R. Limeburner, and L. Rosenfeld, 1985: Introduction to the CODE-2 moored array and large-scale data report, in CODE-2: Moored array and large-scale data report, Tech. Rep. 85-35. Tech. rep., Wood Hole Oceanogr. Inst., Woods Hole, Mass., 1–21 pp.

Benney, D. J., 1966: Long non-linear waves in fluid flows. *J. Math. Phys.*, **45**, 52–63.

Bourgault, D., and D. E. Kelley, 2003: Wave-induced boundary mixing in a partially mixed estuary. *J. Mar. Res.*, **61 (5)**, 553–576.

Buijsman, M. C., Y. Uchiyama, J. C. McWilliams, C. R. Hill-Lindsay, M. C. Buijsman, Y. Uchiyama, J. C. McWilliams, and C. R. Hill-Lindsay, 2012: Modeling Semidiurnal Internal Tide Variability in the Southern California Bight. *J. Phys. Oceanogr.*, **42 (1)**, 62–77.

Butman, B., P. Alexander, A. Scotti, R. Beardsley, and S. Anderson, 2006: Large internal waves in Massachusetts Bay transport sediments offshore. *Cont. Shelf Res.*, **26 (17)**, 2029–2049.

Chapman, D. C., 1982: Nearly trapped internal edge waves in a geophysical ocean. *Deep Sea Res. II*, **29 (4A)**, 525–533.

Chereskin, T. K., 1983: Generation of internal waves in Massachusetts Bay. *J. Geophys. Res.*, **88 (C4)**, 2649.

Choi, W., 2006: The effect of a background shear current on large amplitude internal solitary waves. *Phys. Fluids*, **18 (3)**, 036 601.

da Silva, J. C. B., and K. R. Helfrich, 2008: Synthetic Aperture Radar observations of resonantly generated internal solitary waves at Race Point Channel (Cape Cod). *J. Geophys. Res.*, **113 (C11)**, C11 016.

Dale, A. C., J. M. Huthnance, and T. J. Sherwin, 2001: Coastal-Trapped Waves and Tides at Near-Inertial Frequencies. *J. Phys. Oceanogr.*, **31 (10)**, 2958–2970.

Dale, A. C., and T. J. Sherwin, 1996: The Extension of Baroclinic Coastal-Trapped Wave Theory to Superinertial Frequencies. *J. Phys. Oceanogr.*, **26 (11)**, 2305–2315.

de Young, B., and S. Pond, 1987: The internal tide and resonance in Indian Arm, British Columbia. *J. Geophys. Res.*, **92 (C5)**, 5191.

Gill, A. E., 1982: *Atmosphere-ocean dynamics*. Academic Press, 662 pp.

Glorioso, P. D., and R. A. Flather, 1995: A barotropic model of the currents off SE South America. *J. Geophys. Res.*, **100 (C7)**, 13 427.

Halpern, D., 1971: Semidiurnal internal tides in Massachusetts Bay. *J. Geophys. Res.*, **76 (27)**, 6573–6584.

Haury, L. R., M. G. Briscoe, and M. H. Orr, 1979: Tidally generated internal wave packets in Massachusetts Bay. *Nature*, **278 (5702)**, 312–317.

Helfrich, K. R., W. K. Melville, and J. W. Miles, 1984: On interfacial solitary waves over slowly varying topography. *J. Fluid Mech.*, **149 (-1)**, 305.

Hsu, M.-K., A. K. Liu, and C. Liu, 2000: A study of internal waves in the China Seas and Yellow Sea using SAR. *Cont. Shelf Res.*, **20 (4-5)**, 389–410.

Huthnance, J. M., 1975: On trapped waves over a continental shelf. *J. Fluid Mech.*, **69 (04)**, 689.

Huthnance, J. M., 1978: On Coastal Trapped Waves: Analysis and Numerical Calculation by Inverse Iteration. *J. Phys. Oceanogr.*, **8 (1)**, 74–92.

Ke, Z., and A. E. Yankovsky, 2010: The Hybrid Kelvin–Edge Wave and Its Role in Tidal Dynamics. *J. Phys. Oceanogr.*, **40 (12)**, 2757–2767.

Klymak, J. M., and Coauthors, 2016: Reflection of Linear Internal Tides from Realistic Topography: The Tasman Continental Slope. *J. Phys. Oceanogr.*, **46 (11)**, 3321–3337.

Lai, Z., C. Chen, G. W. Cowles, and R. C. Beardsley, 2010: A nonhydrostatic version of FVCOM: 2. Mechanistic study of tidally generated nonlinear internal waves in Massachusetts Bay. *J. Geophys. Res.*, **115 (C12)**, C12 049.

Lee, C.-Y., and R. C. Beardsley, 1974: The generation of long nonlinear internal waves in a weakly stratified shear flow. *J. Geophys. Res.*, **79 (3)**, 453–462.

Lerczak, J. A., C. D. Winant, and M. C. Hendershott, 2003: Observations of the semidiurnal internal tide on the southern California slope and shelf. *J. Geophys. Res.*, **108 (C3)**, 3068.

Lindzen, R. S., and H. l. Kuo, 1969: A Reliable Method for the Numerical Integration of a Large Class of Ordinary and Partial Differential Equations. *MON. WEA. REV*, 732—-734.

Martin, W., P. MacCready, and R. Dewey, 2005: Boundary Layer Forcing of a Semidiurnal, Cross-Channel Seiche. *J. Phys. Oceanogr.*, **35 (9)**, 1518–1537.

Maslowe, S. A., and L. G. Redekopp, 1980: Long nonlinear waves in stratified shear flows. *J. Fluid Mech.*, **101 (02)**, 321.

Moum, J. N., J. M. Klymak, J. D. Nash, A. Perlin, and W. D. Smyth, 2007: Energy Transport by Nonlinear Internal Waves. *J. Phys. Oceanogr.*, **37 (7)**, 1968–1988.

Moum, J. N., and J. D. Nash, 2008: Seafloor Pressure Measurements of Nonlinear Internal Waves. *J. Phys. Oceanogr.*, **38 (2)**, 481–491.

Moum, J. N., and W. D. Smyth, 2006: The pressure disturbance of a nonlinear internal wave train. *J. Fluid Mech.*, **558**, 153.

Nash, J., E. Shroyer, S. Kelly, M. Inall, T. Duda, M. Levine, N. Jones, and R. Musgrave, 2012a: Are Any Coastal Internal Tides Predictable? *Oceanography*, **25 (2)**, 80–95.

Nash, J. D., S. M. Kelly, E. L. Shroyer, J. N. Moum, and T. F. Duda, 2012b: The Unpredictable Nature of Internal Tides on Continental Shelves. *J. Phys. Oceanogr.*, **42 (11)**, 1981–2000.

Osborne, A. R., and T. L. Burch, 1980: Internal solitons in the andaman sea. *Science*, **208 (4443)**, 451–60.

Pedlosky, J., 2003: *Waves in the Ocean and Atmosphere: Introduction to Wave Dynamics*, Vol. 9. Springer Science & Business Media, 260 pp.

Platzman, G. W., 1978: Normal Modes of the World Ocean. Part I. Design of a Finite-Element Barotropic Model. *J. Phys. Oceanogr.*, **8 (3)**, 323–343.

Platzman, G. W., 1979: A Kelvin wave in the eastern North Pacific Ocean. *J. Geophys. Res.*, **84 (C5)**, 2525.

Platzman, G. W., 1984a: Normal Modes of the World Ocean. Part III: A Procedure for Tidal Synthesis. *J. Phys. Oceanogr.*, **14 (10)**, 1521–1531.

Platzman, G. W., 1984b: Normal Modes of the World Ocean. Part IV: Synthesis of Diurnal and Semidiurnal Tides. *J. Phys. Oceanogr.*, **14 (10)**, 1532–1550.

Platzman, G. W., G. A. Curtis, K. S. Hansen, and R. D. Slater, 1981: Normal Modes of the World Ocean. Part II: Description of Modes in the Period Range 8 to 80 Hours. *J. Phys. Oceanogr.*, **11 (5)**, 579–603.

Rivas, A. L., 1997: Current-meter observations in the Argentine Continental Shelf. *Cont. Shelf Res.*, **17 (4)**, 391–406.

Savidge, D. K., C. R. Edwards, and M. Santana, 2007: Baroclinic effects and tides on the Cape Hatteras continental shelf. *J. Geophys. Res.*, **112 (C9)**, C09 016.

Scotti, A., R. Beardsley, and B. Butman, 2006: On the interpretation of energy and energy fluxes of nonlinear internal waves: an example from Massachusetts Bay. *J. Fluid Mech.*, **561**, 103.

Scotti, A., R. C. Beardsley, and B. Butman, 2007: Generation and propagation of nonlinear internal waves in Massachusetts Bay. *J. Geophys. Res.*, **112 (C10)**, C10 001.

Scotti, A., R. C. Beardsley, B. Butman, and J. Pineda, 2008: Shoaling of nonlinear internal waves in Massachusetts Bay. *J. Geophys. Res.*, **113 (C8)**, C08 031.

Scotti, A., B. Butman, R. C. Beardsley, P. S. Alexander, and S. Anderson, 2005: A Modified Beam-to-Earth Transformation to Measure Short-Wavelength Internal Waves with an Acoustic Doppler Current Profiler. *J. Atmos. Ocean. Technol.*, **22 (5)**, 583–591.

Scotti, A., and J. Pineda, 2004: Observation of very large and steep internal waves of elevation near the Massachusetts coast. *Geophys. Res. Lett.*, **31 (22)**, L22 307.

Shroyer, E., J. Moum, and J. Nash, 2010: Energy transformations and dissipation of nonlinear internal waves over New Jersey's continental shelf. *Nonlinear Process. Geophys.*, **17 (4)**, 345–360.

Shroyer, E. L., J. N. Moum, and J. D. Nash, 2009: Observations of Polarity Reversal in Shoaling Nonlinear Internal Waves. *J. Phys. Oceanogr.*, **39 (3)**, 691–701.

Shroyer, E. L., J. N. Moum, and J. D. Nash, 2011: Nonlinear internal waves over New Jersey's continental shelf. *J. Geophys. Res.*, **116 (C3)**, C03 022.

Smyth, W. D., J. N. Moum, and J. D. Nash, 2011: Narrowband Oscillations in the Upper Equatorial Ocean. Part II: Properties of Shear Instabilities. *J. Phys. Oceanogr.*, **41**, 412–428.

Stastna, M., and K. G. Lamb, 2002: Large fully nonlinear internal solitary waves: The effect of background current. *Phys. Fluids*, **14 (9)**, 2987–2999.

Stöber, U., and J. N. Moum, 2011: On the potential for automated realtime detection of nonlinear internal waves from seafloor pressure measurements. *Appl. Ocean Res.*, **33 (4)**, 275–285.

Winant, C. D., 2010: Two-Layer Tidal Circulation in a Frictional, Rotating Basin. *J. Phys. Oceanogr.*, **40 (6)**, 1390–1404.

APPENDICES

Appendix A: Volume conservation in the coupled barotropic-baroclinic resonant modes problem

In thesis Chapters 3 and 4, the grouping of the terms in the second partial differential equation (equation 3.11) results in a discretized form that does not conserve volume for even modes. That is, the sum of the discretized form over the entire basin is not zero. A restructuring of the terms in which the derivative of the bathymetry, $\frac{\partial h}{\partial x}$ and $\frac{\partial h}{\partial y}$, is grouped within the first derivative of N' and Z does lead to volume conservation. That is, if rather than the form of the second partial differential in equation 3.11, the equation is structured as

$$\frac{1}{\sigma^2(1-f^2)}\left\{i\frac{\partial}{\partial x}\left[(h(x,y)-h_1)\left(\frac{\partial N'}{\partial x}+\rho\frac{\partial Z}{\partial x}\right)\right]+i\frac{\partial}{\partial y}\left[(h(x,y)-h_1)\left(\frac{\partial N'}{\partial y}+\rho\frac{\partial Z}{\partial y}\right)\right]\right.$$
$$\left.+f\frac{\partial}{\partial x}\left[(h(x,y)-h_1)\left(\frac{\partial N'}{\partial y}+\rho\frac{\partial Z}{\partial y}\right)\right]-f\frac{\partial}{\partial y}\left[(h(x,y)-h_1)\left(\frac{\partial N'}{\partial x}+\rho\frac{\partial Z}{\partial x}\right)\right]\right\}$$
$$+iZ=0, \quad \text{(A.1)}$$

then volume is conserved.

Simplifying this to look at just the one-dimensional basin without rotation, the volume conserving discretized form of the second partial differential equation is

$$\frac{1}{\sigma^2}\frac{1}{\delta x}\left\{\left[\frac{1}{2}(h_{j+1}+h_j)-h_1\right]\frac{(N'+\rho Z)_{j+1}-(N'+\rho Z)_j}{\delta x}\right.$$
$$\left.-\left[\frac{1}{2}(h_j+h_{j-1})-h_1\right]\frac{(N'+\rho Z)_j-(N'+\rho Z)_{j-1}}{\delta x}\right\}+Z_j=0\,. \qquad \text{(A.2)}$$

When this structure is used, the results for the one-dimensional problem are identical to those presented in thesis Chapter 3, except that volume is conserved.

For example, the variance of the interface motions between the two methods line up nearly perfectly (Fig. A.1). Looking at an example even mode structure that obviously does not conserve volume, as demonstrated by the sea surface structure being less than zero across the entire basin, we see that the structure for the discretization that does conserve volume shows an identical mode, but with the mean offset from zero removed (Fig. A.2). As further demonstration that the two discretization methods give the same results (other than volume conservation) and thus that conclusions do not change, comparing the results for a barotropic basin mode with an odd number of zero crossings for a basin with wide shelves shows that the coupling of baroclinic scales in barotropic modes persists when volume is conserved (Fig. A.3). The volume conserving method has smaller amplitude baroclinic scales in the deep basin, but they still exist. This amplitude difference is likely due to one method being slightly less converged to the mode than the other. Subtle changes in relative amplitudes for coupled modes occur depending on how converged the frequency is to the mode.

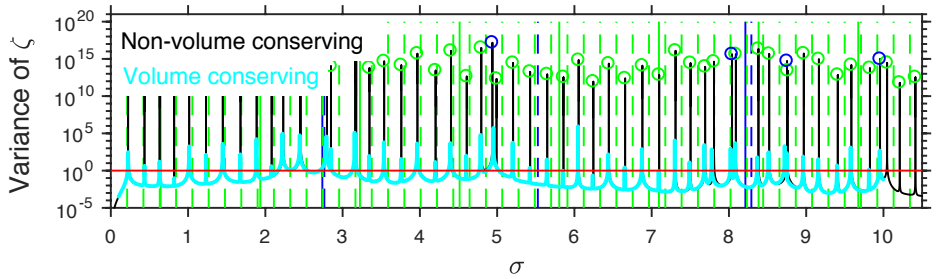

Figure A.1: Variance of interface motions (ζ) averaged over the basin and normalized by forcing variance from solutions to the forced one-dimensional problem versus σ, for the equation discretization used in thesis Chapters 3 and 4 that does not conserve volume (black line) versus the form that does conserve volume (cyan line), showing that the two methods result in the same variance distribution. The volume conserving results shown here have not been iterated through smaller $\Delta\sigma$ to converge on higher amplitude peaks. This is for the wide shelf basin with $h1 = 0.02625$, $\delta_{BC} = 0.70$, and $\rho = 0.25$. Blue circles denote peaks of barotropic modes; green circles denote peaks of baroclinic modes. The horizontal red line is the normalized forcing variance. Vertical dashed lines show predicted σ_n for barotropic (blue) and baroclinic (green) modes (equation 3.21). Vertical solid lines are values of σ_m (equation 3.22), which show when multiples of quarter barotropic (blue) and baroclinic (green) wavelengths fit across the shelf width.

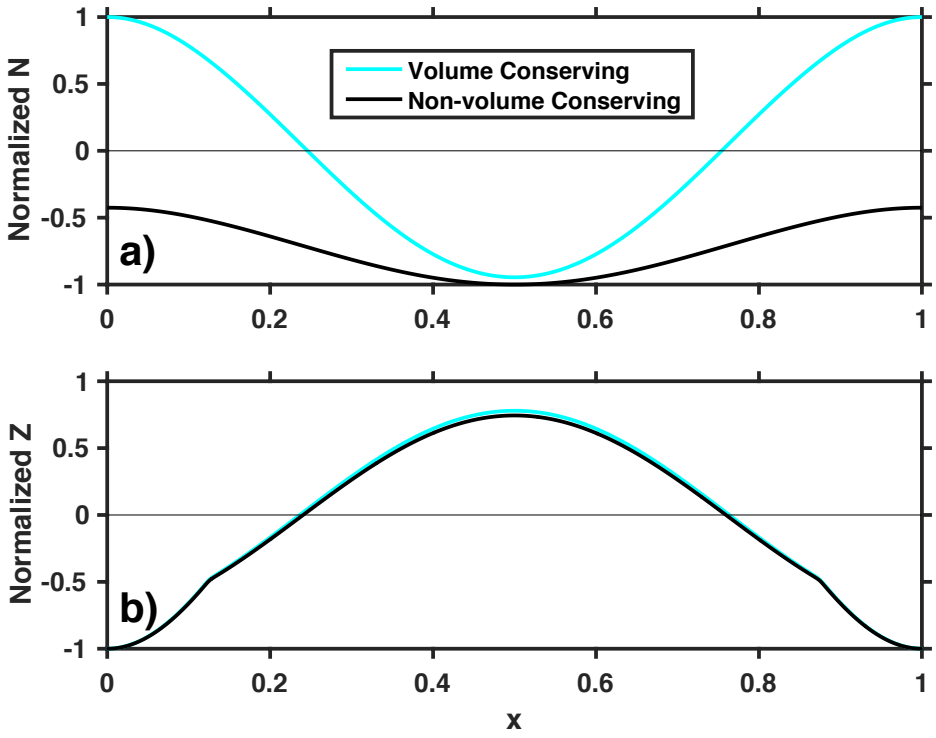

Figure A.2: Normalized baroclinic basin mode 2 structure of the sea surface, N, (a) and interface, Z, (b) for the basin with wide shelves, $h1 = 0.02625$, $\delta_{BC} = 0.70$, and $\rho = 0.01$, compared between the volume conserving (cyan) and non-volume conserving discretization (black). In panel (b), the cyan line is mostly covered by the black line.

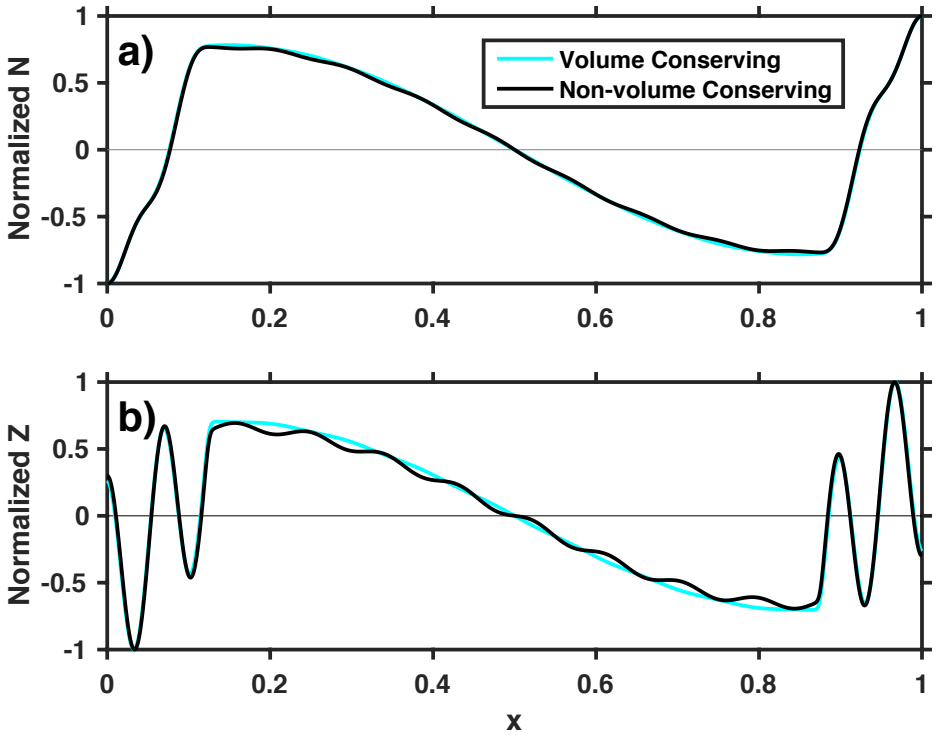

Figure A.3: Normalized barotropic basin mode 3 structure of the sea surface, N, (a) and interface, Z, (b) for the basin with wide shelves, $h1 = 0.02625$, $\delta_{BC} = 0.70$, and $\rho = 0.25$, compared between the volume conserving (cyan) and non-volume conserving discretization (black). In both panels, the cyan line is mostly covered by the black line.